Evaluating the CO distributions from current atmospheric chemistry models using satellite observations from MOPITT and SCIAMACHY

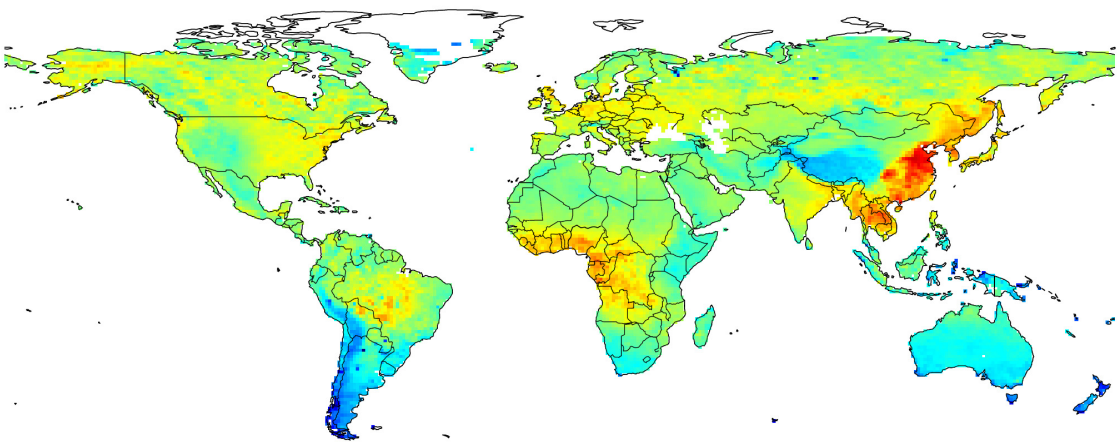

Cheng Liu

Dissertation

submitted to the

Combined Faculties for the Natural Sciences and for Mathematics

of the Ruperto-Carola University of Heidelberg, Germany

for the degree of

Doctor of Natural Sciences

Put forward by

Master-Physics: Cheng Liu

Born in: Bengbu, China

Date of the oral examination: 27. October 2010

Evaluating the CO distributions from current atmospheric chemistry models using satellite observations from MOPITT and SCIAMACHY

Referees: **Prof. Dr. Ulrich Platt**

Prof. Dr. Thomas Wagner

Zusammenfassung

Im Rahmen dieser Arbeit wurde ein neuer Algorithmus entwickelt, der vertikale Säulendichten von CO aus spektralen Messungen im nahen Infrarot des SCIAMACHY Satelliten-Instruments auf ENVISAT bestimmt. Effekte der Eis-Schicht auf den SCIAMACHY Detektoren wurden durch Vergleich mit MOPITT-Messungen über Ozean empirisch korrigiert. Obwohl in dieser Arbeit nur Beobachtungen mit effektiver Wolkenbedeckung unter 20% verwendet werden, können Wolkeneffekte aufgrund der hohen Wolkenalbedo immer noch groß sein. Daher wurde ein neu entwickeltes Korrekturschema angewendet, das explizit Wolkenbedeckung, Wolkenhöhe und Bodenalbedo für jede Einzelbeobachtung berücksichtigt. Die resultierenden SCIAMACHY CO Säulendichten erlauben die Untersuchung der CO-Verteilung über Kontinenten, also über den Quellregionen.
Der resultierende Datensatz wurde mit Messungen des MOPITT Instruments sowie Modellergebnissen von drei globalen Chemiemodellen (MATCH, EMAC und GEOS-CHEM) verglichen; der Fokus des Vergleichs liegt auf Regionen mit hohen CO Emissionen, also Gebiete mit Biomassenverbrennung oder anthropogenen Quellen. Der Vergleich ergab, dass über den meisten Regionen die modellierten CO Säulendichten systematisch niedriger als die Satellitenbeobachtungen sind, wobei die größten Differenzen im Vergleich mit SCIAMACHY auftreten. Da SCIAMACHY auch für die untere Troposphäre noch sensitiv ist, lässt dies darauf schließen, dass insbesondere nahe der Oberfläche die Modelle die wahre CO Konzentration unterschätzen, möglicherweise aufgrund zu niedriger CO Emissionen in heutigen Inventaren.

Summary

This thesis developed a new CO vertical column density product from near IR observations of the SCIAMACHY instrument aboard ENVISAT. To correct the effects of the ice layer on the SCIAMACHY near-IR detectors a normalization procedure based on collocated MOPITT observations over the oceans was developed. Although in this thesis only SCIAMACHY observations for effective cloud fractions below 20% are used, the remaining effects of clouds can still be large due to the higher cloud top albedo. Thus, a newly developed correction scheme is applied, which explicitly considers the cloud fraction, cloud top height and surface albedo of individual observations. The resulting SCIAMACHY CO data is well suited for the investigation of the CO distribution over the continents, where important emission sources are located.
This thesis compared the new SCIAMACHY CO data set, and also observations from the MOPITT instrument, to the results from three chemistry climate models (MATCH, EMAC, and GEOS-CHEM); the focus of this comparison is on regions with strong CO emissions (from biomass burning or anthropogenic sources). The comparison indicates that over most of these regions the simulated CO vertical column densities are systematically smaller than the satellite observations with the largest differences compared to the SCIAMACHY observations. Because of the high sensitivity of the SCIAMACHY observations for the lowest part of the atmosphere, this indicates that especially close to the surface the model simulations systematically underestimate the true atmospheric CO concentrations, probably caused by an underestimation of the true CO emissions by current emission inventories.

Contents

1 Introduction

1.1 Foreword and Thesis Outline

The ability to understand and predict future concentrations of global carbon monoxide (CO) and its effect on the earth system depends on the knowledge of the sources (emission estimates) and sinks. Therefore, the objective of this thesis is to acquire the global distribution of carbon monoxide with Scanning Imaging Absorption spectrometer for Atmospheric CHartographY (SCIAMACHY) satellite near-infrared measurements and to compare it with climate chemistry models. Due to its high sensitivity to all atmospheric layers, the SCIAMACHY CO data set could be used to improve the existing CO emission inventories of climate chemistry models on a global scale. For this purpose, a new data set of SCIAMACHY observations of the CO Vertical Column Density (VCD) is developed in this thesis. In contrast to other SCIAMACHY CO retrievals, a normalization procedure using coincident The Measurements of Pollution In The Troposphere (MOPITT) observations over the oceans is applied. This normalization procedure is applied on a daily basis for different latitude ranges; thus artificial offsets in the SCIAMACHY CO data are corrected depending on season and latitude. While the new SCIAMACHY CO data set can not be considered as fully independent from MOPITT observations, it can still be used for the investigation of the CO distribution over the continents, where all important CO emission sources are located. In this thesis only SCIAMACHY observations with effective cloud fraction below 20% are used. However, due to the much higher albedo of cloud compared to ground surface, the remaining effects of clouds can still be large (errors up to 100%), thus a correction of the remaining cloud effects depending on effective cloud fraction, cloud top height and surface albedo is applied. Here it is interesting to note that – to our knowledge – no explicit cloud correction has so far been applied to SCIAMACHY CO observations. Omission of a proper cloud correction can lead to systematic errors up to 100%, especially over polluted regions.

The thesis is divided into 7 chapters:

Chapter 1 introduces the role and the characteristics of carbon monoxide in atmospheric

chemistry and gives a brief overview of the state of the study of carbon monoxide retrieval from SCIAMACHY satellite instrument.

Chapter 2 introduces the satellite instrument SCIAMACHY (Scanning Imaging Absorption spectrometer for Atmospheric CHartographY), and also gives a brief introduction to another satellite instrument MOPITT (Measurements of Pollution in the Troposphere), which measures in the thermal-infrared.

Chapter 3 covers fundamental background knowledge for spectroscopic aspects.

Chapter 4 first introduces differential optical absorption spectroscopy (DOAS). Then it presents the used retrieval algorithm, a modified iterative maximum a posteriori-DOAS (IMAP-DOAS) and describes the improvements compared to the standard DOAS, which properly accounts for the temperature and pressure dependence of the high resolution absorption lines and the moderate spectral resolution of SCIAMACHY.

Chapter 5 first introduces the concept of air mass factor (AMF) which is used to convert the slant column density (SCD) to the vertical column density (VCD) and the concept of Box-AMF which describes the measurement sensitivity of altitude. Then a radiative transfer model (McArtim) to study the effect of clouds on the retrieved CO VCD is presented. It shows that errors due to even small cloud fractions (cloud fraction < 20%) can be large (errors up to 100%). For this reason, this chapter presents a correction scheme which explicitly considers the cloud fraction, cloud top height and surface albedo of individual observations.

Chapter 6 introduces the SCIAMACHY near-infrared instrument degradation and calibration problems, in particular an ice layer deposited on the detector, which strongly affects the instrument's response function. It then demonstrates several procedures which have been developed by other groups to correct the time dependent disturbances of the SCIAMACHY near IR channels. Nevertheless, from the comparison with collocated MOPITT data it turned out that not all artifacts caused by the instrumental problems could be sufficiently corrected by these procedures for the whole time series of SCIAMACHY CO observations.

Chapter 7 describes a completely different strategy to correct the the icing problem of SCIAMACHY CO observations: a normalization procedure of the SCIAMACHY observations using coincident observations of the MOPITT instrument over the oceans. This normalization

procedure is applied on a daily basis for different latitude ranges; thus artificial offsets in the SCIAMACHY CO data are corrected depending on season and latitude. While the new SCIAMACHY CO data set can not be considered as fully independent from MOPITT observations, it can still be used for the investigation of the CO distribution over the continents, where all important CO emission sources are located.

Chapter 8 presents the new data set of CO VCDs from the SCIAMACHY measurements, a validation with ground-based Fourier-Transform Infrared (FTIR) spectrometers observations, and a comparison with thermal IR satellite (MOPITT) observations.

Chapter 9 compares our SCIAMACHY CO data set, and also observations from the MOPITT instrument, to the results from three chemistry climate models (MATCH, EMAC, and GEOS-CHEM) in regions with strong CO emissions (from biomass burning or anthropogenic sources). For this comparison only coincident measurements/model results are selected and the height dependent sensitivity of both satellite instruments is considered explicitly.

1.2 Atmospheric Pollution

Atmospheric pollution is the introduction of chemicals, or particulate matter into the atmosphere that causes harm or discomfort to humans or other living organisms, or damages the natural environment.

Atmospheric pollution is a serious global problem, and is especially problematic in large urban areas such as Mexico City and East Asia. Many people suffer from serious illnesses caused by smog and air pollution in these areas. Plants, buildings, and animals are also victims of a particular type of air pollution called acid rain. Acid rain is caused by airborne sulfur from burning coal in power plants and can be transported in rain droplets for thousands of kilometers. Poisons are then deposited in streams, lakes, and soils, causing damage to wildlife. In addition, acid rain eats into concrete and other solid structures, causing buildings to slowly deteriorate.

Scientists study air pollution by distinguishing between two different categories of gasses: permanent and variable. The most common of the stable gasses are nitrogen at 78%, and

oxygen at 21% of the total atmosphere. Some highly variable gasses, often referred to as trace gases, are water vapor, carbon dioxide, methane, carbon monoxide, sulfur dioxide, nitrogen dioxide, ozone, ammonia, and hydrogen sulfide.

The output of many trace gasses increases with the growth of industrialization and population. The benefits of progress cost people billions of dollars each year in repairing and preventing air pollution damage. This includes health care and the increased maintenance of structures that are crumbling, in part due to air pollution.

The effects of air pollution have to be carefully measured because the build-up of pollutants depends on atmospheric conditions and a specific area's emission level. Once pollutants are released into the atmosphere, wind patterns make it impossible to contain them to any particular region. This is why e.g., the effects of pollution from major oil fires in the Middle East are measurable in Europe and elsewhere. On the other hand, terrestrial formations such as mountain ridges can act as natural barriers. The terrain and climate of a particular area (e.g., Bei Jing whose three sides are surrounded by mountains) can also help promote and accumulate air pollution. Specifically, weather conditions, called thermal inversions, can trap the impurities and cause them to build up until they have reached dangerous levels. A thermal inversion is created when a layer of warm air settles over a layer of cool air closer to the ground. It can stay until rain or wind dissipates the layer of stationary warm air.

Only satellite data, with high spatio-temporal resolution, can be used to acquire the global distribution of atmospheric pollutants to complement people’s knowledge of the sources and sinks and the corresponding seasonal variation.

1.3 Atmospheric Carbon Monoxide

Carbon monoxide (CO) is an important trace gas constituent of the Earth's atmosphere. Despite its relatively small concentration, CO plays an important role in atmospheric chemistry via its effect on the hydroxyl radical (OH) concentration. In case of high NO_x, the reaction of CO with OH leads to the formation of carbon dioxide and ozone, as shown schematically in Eq.1.3.1.-1.3.6. Locally, CO is an important component in urban and indoor air pollution and is considered as a critical air pollutant because of its short-term harmful health effects. Furthermore, it has been proposed that CO emissions have a GWP (Global Warming Potential), although it does not absorb terrestrial infrared radiation strongly enough to be counted as a direct greenhouse gas (Shine *et al.*, 1990; Fuglestvedt *et al.*, 1996; Prather, 1996). Because CO affects the lifetimes of other greenhouse gases by influencing the atmospheric burden of OH (Isaksen and Hov, 1987) and thus can be considered to be an indirect greenhouse gas on the basis of its effect on the lifetime of other greenhouse gases. For example, it is estimated that emitting 100 Tg of CO is equivalent to emitting 5 Tg of CH_4 for its global warming potential (Wild and Prather, 2000). Therefore, our ability to understand and predict future concentrations of important gases and their effects on the earth system depends in part on understanding the sources and global distribution of atmospheric carbon monoxide.

$$CO + OH \rightarrow H + CO_2 \qquad 1.3.1$$
$$H + O_2 + M \rightarrow HO_2 + M \qquad 1.3.2$$
$$HO_2 + NO \rightarrow NO_2 + OH \qquad 1.3.3$$
$$NO_2 \xrightarrow{h\nu(\lambda<420nm)} NO + O \qquad 1.3.4$$
$$O + O_2 + M \rightarrow O_3 + M \qquad 1.3.5$$

$$CO + 2O_2 \rightarrow O_3 + CO_2 \qquad 1.3.6$$

In clean air (low NO_x abundance), however, ozone and OH are destroyed:

$$2CO + 2OH \rightarrow 2H + 2CO_2 \qquad 1.3.7$$
$$2H + 2O_2 + 2M \rightarrow 2HO_2 + 2M \qquad 1.3.8$$
$$HO_2 + O_3 \rightarrow 2O_2 + OH \qquad 1.3.9$$

$$2CO + O_3 + OH \rightarrow HO_2 + 2CO_2 \qquad 1.3.10$$

The well-known sources of atmospheric CO consist of four types. The first type is the combustion of carbonaceous fossil and biofuels such as coal, oil, gasoline and wood, and constitutes a significant portion of direct emissions of CO on a global scale. The second type is boilers, ovens, industrial engines, residential heating in industry-related processes (e.g., production of steel and cracking of crude oil) due to energy use, which shows less seasonal variation. The third type is the incomplete combustion of living and dead plant organic matter (loosely termed as biomass) in large-scale forest fires, in burning of agricultural wastes, and in clearing of forest, savanna and brush lands by fire for agricultural purposes (Crutzen and Andreae, 1990; Levine, 1991; Levine *et al.*, 1995). Biomass burning, which generally shows a strong seasonal variation, can be both natural and anthropogenic. In particular, lightning can trigger mid- and high latitude fires and ignites the dry vegetation in tropical region. Unlike other sources, which are emitted within the surface layer, CO can also be produced indirectly through chemical oxidation of carbon-containing compounds in the atmosphere. Non-methane hydrocarbons (NMHC) from biogenic sources such as isoprenes and monoterpenes emitted by vegetation (Zimmerman *et al.*, 1978) or from anthropogenic sources in the form of volatile organic compounds (VOC) emitted from automobiles and the use of organic solvents, react with OH radicals or O_3 and are converted to oxygenated compounds and then partly to CO (Logan *et al.*, 1981). The yields of CO vary depending on the parent NMHC and environmental conditions such as temperature, light availability, and other trace gas concentrations (e.g., Miyoshi *et al.*, 1994; Hatakeyama *et al.*, 1991) The initial reaction of CH_4 with OH also leads to the production of CO (e.g., Wofsy *et al.*, 1972; Weinstoc and Niki, 1972). The emission estimates of global CO are given in Table 1.1 (IPCC, 2001). For a more detailed overview of the global CO budget and its implication see (IPCC, 2001) (Holloway *et al.*, 2000; Houghton, 2000; Bergamaschi *et al.*, 2000a; Bergamaschi *et al.*, 2000b) and references therein.

Table 1.1: IPCC (2001) carbon monoxide emission estimates

Category	Carbon monoxide source strength (Tg/year)
Sources	
Oxidation of CH_4	800
Oxidation of Isoprene	270
Oxidation of industrial NMHC	110
Oxidation of biomass NMHC	30
Oxidation of Acetone	20
Sub-total in situ oxidation	1230
Vegetation	150
Oceans	50
Biomass burning	700
Fossil & domestic fuel	650
Sub-total direct emissions	1550
Total sources	2780
Sinks	
Surface deposition	200-640
OH reaction	1500-2700

Carbon monoxide has a chemical lifetime of 30-90 days in the troposphere. Measurements indicate that there is more CO in the Northern Hemisphere than in the Southern Hemisphere; the maximum values are found near the surface at northern midlatitudes. In general, the CO mixing ratios decrease with altitude in the Northern Hemisphere to a free tropospheric average value of about 120ppb near 45N. In the Southern Hemisphere CO tends to be more uniformly mixed vertically with a mixing ratio of about 60ppb near 45S. Seasonal variations have been established to be about $\pm 49\%$ of the mean in the Northern Hemisphere and $\pm 20\%$ of the mean in the Southern Hemisphere. The maximum concentration is observed to occur during local spring and the minimum is found during late summer or early fall.

Since the start of the Industrial Revolution human activities affect increasingly the world we live in by changing atmospheric conditions in a significant way. Carbon monoxide, which is an indirect greenhouse gas and major pollutant harmful to human health and plants, not only changes global climate, but also destructs the stratospheric ozone. The quantification of its effects requires an accurate understanding of the distribution of the sources and sinks which is unfortunately limited by the sparse ground-based measurements. However, satellite data, with high spatio-temporal resolution, can be used to acquire the global distribution of sources and sinks and the corresponding seasonal variations which is not only the compensation of fewer ground-based measurements but also could help to improve climate chemistry model's precision. The detailed description of the satellite instruments used for the retrieval (SCIAMACHY) and for the comparison (MOPITT) will be given in chapter 2.

1.4 New Algorithm for the Retrieval of CO from the SCIAMACHY Near-infrared Channel

The well known differential optical absorption spectroscopy (DOAS) (Platt and Wiley, 1994) is a widely used method to determine the concentration of atmospheric trace gases. In general, the DOAS technique is about analyzing spectra in the UV and visible region that has been transmitted through long atmospheric paths. Different atmospheric species will leave their absorption fingerprints in the spectra from which concentrations could be retrieved. However, in the near-infrared region, because the cross sections of trace gases like CO, CH_4 and H_2O depend strongly on temperature and pressure, and because the absorption lines are narrower than the spectral resolution of SCIAMACHY, the classical DOAS is not appropriated any more.

Some authors have already noticed the drawbacks of the classical DOAS algorithm under certain conditions. Maurellis *et al.* (2000) parameterized the DOAS algorithm for highly structured spectra, while Solomon *et al.* (1989) and Volkamer *et al.* (1998) analyzed the interference between different absorbers. For the analysis of absorption spectra in the near-IR, three independent scientific algorithms IMLM, WFM-DOAS and IMAP were developed in

three institutes, and will be described shortly below.

The IMLM (de Laat *et al.*, 2006) retrieval method is based on an Iterative Maximum Likelihood Method and was developed at SRON (Netherlands institute for space research). The retrieval uses a fixed set of climatologically atmospheric profiles based on the US standard atmosphere (1976) to compute a model spectrum in terms of optical depths. For each SCIAMACHY ground pixel these profiles are corrected for the mean surface elevation of the pixel, by cutting off the part of the profile below the surface.

The Weighting Function Modified Differential Optical Absorption Spectroscopy (WFM-DOAS) (Buchwitz and Burrows, 2004) method is based on fitting the logarithm of a linearized radiative transfer model plus a low-order polynomial to the logarithm of the ratio of a measured nadir radiance and solar irradiance spectrum (observed sun normalized radiance). The fit parameters are the trace gas vertical columns plus other parameters such as a temperature profile shift. In order to avoid time consuming on-line radiative transfer calculations WFM-DOAS has been implemented as a look-up table scheme.

In this thesis, the iterative maximum a posteriori DOAS (IMAP-DOAS) (Frankenberg *et al.*, 2005a, 2005b) method which was developed at the University of Heidelberg by C. Frankenberg is adopted. The algorithm is based on the optimal estimation theory introduced to the remote sensing community by (Rodgers, 1976). This method iterates the vertical column densities of the absorbers of interest until the expected spectral signature of the total optical density fits the measurement. It accounts for nonlinearities due to spectrally non-resolved strong absorptions and considers the sensitivity to pressure and temperature changes in the atmospheric profile. A detailed description of the algorithm can be found in chapter 4. In addition, two important improvements are developed and applied, which are described in detail in chapter 5 and chapter 7.

1.5 The Study of SCIAMACHY CO Retrievals: State of the Art

Many comparisons of CO VCDs from SCIAMACHY with other satellite observations (mainly MOPITT) and model results have been performed in recent years (e.g., Buchwitz *et al.*, 2004; Gloudemans *et al.*, 2005; Straume *et al.*, 2005; Buchwitz *et al.*, 2006a; Buchwitz *et al.*, 2007; Turquety *et al.*, 2008; de Laat *et al.*, 2010; Kopacz *et al.*, 2010). Besides for validation purposes, the aim of these comparisons was also the improvement of current emission estimates.

In the comparison studies between different satellite instruments it was mostly found that the CO VCDs derived from SCIAMACHY satellite instrument are larger than those derived from MOPITT satellite instrument (e.g., Buchwitz *et al.*, 2004; Buchwitz *et al.*, 2006a; Buchwitz *et al.*, 2007; Turquety *et al.*, 2008), in agreement with the assumption that the CO concentrations close to the surface are higher than those assumed for the MOPITT a-priori profiles (which represent current knowledge about the CO profiles, especially in the surface-near layers).

In the comparison studies with model simulations in most cases the CO VCDs from SCIAMACHY are found to be higher than the corresponding model data, especially over polluted regions, indicating that current emission inventories underestimate the true emissions (e.g., Gloudemans *et al.*, 2006; de Laat *et al.*, 2006; de Laat *et al.*, 2007; Gloudemans *et al.*, 2009; de Laat *et al.*, 2010; Kopacz *et al.*, 2010)

Sometimes models were also used as 'transfer tools' for the comparison of CO VCDs from SCIAMACHY with those from other satellite sensors (e.g., Turquety *et al.*, 2008; de Laat *et al.*, 2010; Kopacz *et al.*, 2010).

However, it was found that the comparisons between SCIAMACHY observations and those from other satellite instruments suffer from two general problems:

a) Many of these comparison were rather qualitative (e.g., Buchwitz *et al.*, 2004; Straume *et al.*, 2005; Buchwitz *et al.*, 2006a; Buchwitz *et al.*, 2007). While in general good agreement of the observed patterns was found, the quantitative comparison was complicated by the different spatio-temporal sampling of SCIAMACHY and the other satellite observations: besides the

different height-dependencies of near-IR and thermal IR sensors, also often not collocated observations were compared. Sometimes even night-time observations of the thermal IR sensors were included in the comparison. Also, the effect of clouds on the SCIAMACHY observations was not adequately corrected.

b) Some comparison studies were performed in a more quantitative way (e.g., Turquety *et al.*, 2008; de Laat *et al.*, 2010; Kopacz *et al.*, 2010). Only collocated observations were used for the comparisons and the different height-dependencies of near IR and thermal IR sensors were adequately considered (e.g., using model simulations). In particular Turquety *et al.* (2008) retrieved a boundary layer partial CO VCD from the comparison of SCIAMACHY and MOPITT observations, and related these partial CO VCDs to the respective quantity from model simulations. However, in these comparisons always inconsistencies were found which limited the quantitative interpretation of the retrieved results. Besides possible errors of the MOPITT observations and/or the model simulations, these biases are mainly related to still existing biases in the SCIAMACHY CO retrievals (and missing cloud correction, see chapter 5).

In fact, in many studies, biases of the SCIAMACHY CO VCDs were reported or were obvious in the presented data sets. Typically, they do not only depend on location (e.g., latitudinal gradient) but also vary with time, (Buchwitz *et al.*, 2005; Buchwitz *et al.*, 2007; Turquety *et al.*, 2008; Gloudemans *et al.*, 2009; de Laat *et al.*, 2010; Kopacz *et al.*, 2010). The reasons for these biases are not completely understood, but are probably related to several problems of the SCIAMACHY detectors or retrieval algorithms. For example a changing ice-layer on the SCIAMACHY near-IR detectors influences the measurements in several ways (e.g., Gloudemans *et al.*, 2005). Most importantly, it causes a loss of signal strength and systematically changes the instrument slit function. In addition, the dark current of the detectors is influenced. Variations of the dark current occur also within individual orbits. The SCIAMACHY near-IR detectors also suffer from variable but generally increasing numbers of so called bad and dead pixels, which can not be used for the analysis. For all of these problems sophisticated solutions have been developed and applied in recent years (e.g., Gloudemans *et al.*, 2005; Frankenberg *et al.*, 2005b; Buchwitz *et al.*, 2006a; Buchwitz *et al.*, 2007; Gloudemans *et al.*, 2009). Nevertheless, these corrections are not perfect, and the retrieved CO

VCDs are still subject to remaining errors. Especially it was shown that the application of different dead/bad pixel masks leads to systematic changes of the retrieved CO VCDs (Buchwitz *et al.*, 2007). In addition to the systematic errors caused by these effects, the random errors for the CO retrieval are generally large (up to >100%), mainly depending on the brightness of the observed scene (Gloudemans *et al.*, 2005; Frankenberg *et al.*, 2005a; Buchwitz *et al.*, 2006a; de Laat *et al.*, 2007; Gloudemans *et al.*, 2008). Thus many individual observations are usually averaged (for example monthly means) to achieve smaller measurement uncertainties.

Besides these instrumental problems, also some ambiguity with respect to the analysis parameters remains. For example, the specific choice of the spectral window (Gloudemans *et al.*, 2005; Buchwitz *et al.*, 2006a) and the spectral data used for the analysis has an influence on the retrieved CO VCDs (Gloudemans *et al.*, 2005; Gloudemans *et al.*, 2009). These effects are mainly related to the fact that the strength of the overlapping absorptions of CH_4 and H_2O is much weaker than that of CO. Another problem is that usually a height-independent sensitivity for the SCIAMACHY CO observations was assumed. While this is mostly true for completely cloud-free conditions and small solar zenith angles (Buchwitz *et al.*, 2004; Gloudemans *et al.*, 2008; de Laat *et al.*, 2010), the sensitivity of SCIAMACHY for the lowest atmospheric layers can be systematically reduced for large solar zenith angles and/or in the presence of clouds (see chapter 5). Again, while most of these problems have been investigated in detail in recent years and optimized retrieval settings have been found, systematic biases still remain which are difficult to quantify. Like the other groups working on the SCIAMACHY CO retrieval, this thesis also investigates several ways to correct and minimize the effects of the instrumental problems and limitations of the spectral analysis. For example the instrumental slit functions from the widths of the strong absorption lines of CH_4 and H_2O within the CO fitting range on a daily basis are determined and then these time dependent slit functions are applied to the CO retrieval. In a similar way a possible time-dependent spectral offset is determined and corrected (e.g., Gloudemans *et al.*, 2005). Furthermore the normalization procedure using the simultaneously retrieved CH_4 VCD, as suggested by Buchwitz *et al.* (2007), is applied. The results of these studies are described in detail in chapter 6. However, it turned out that (similar to the results of several other studies),

part of the problems of the SCIAMACHY CO data could be improved, at least for limited periods of time, but always systematic biases remained.

From the temporal variation and latitudinal dependence of the biases of the SCIAMACHY CO VCDs (mainly related to instrumental problems and limitations of the spectral analyses) it can be concluded that they are complex functions of several parameters (e.g., solar zenith angle, cloud properties, number and location of bad and dead detector pixels, instrument throughput, and strength of H_2O and CH_4 absorptions). Besides the comparison between SCIAMACHY with other satellite sensors, also any comparison of SCIAMACHY data with model results will be systematically influenced by these biases in the SCIAMACHY CO VCDs.

For these reasons, this thesis developed a normalization procedure of the SCIAMACHY CO VCDs using simultaneous observations of the MOPITT instrument (see e.g., Drummond and Mand, 1996; Deeter *et al.*, 2003) over the ocean. This normalization is performed on a daily basis and depending on latitude (the details are presented in chapter 7). Thus especially the spatio-temporal variation of the bias between SCIAMACHY and MOPITT is corrected for. Of course, due to this normalization procedure the SCIAMACHY CO data can not be regarded as a completely independent data set anymore. In particular, all potential problems of the MOPITT observations will be directly transferred to the retrieved SCIAMACHY CO VCDs. Nevertheless, any systematic (and varying) biases between both instruments are largely reduced. This is an important achievement, because now the potential of the different height sensitivities of both instruments can be fully explored. Also, it is worth noting that MOPITT observations have been validated in many studies and generally very good agreement was found.

In addition to the normalization procedure, this thesis also applies a sophisticated cloud correction. So far, the cloud effect was discussed in many studies, but it was not explicitly corrected for. Instead, usually only measurements for small cloud fractions (typically <20%) are considered (e.g., de Laat *et al.*, 2010; Kopacz *et al.*, 2010) and references therein. Here it might be worth mentioning that using such a rather strict selection criterion leads to a strong decrease of the number of useful SCIAMACHY observations. According to a study of Krijger *et al.* (2007) only about 25% of all SCIAMACHY CO observations have a cloud fraction

<20%. Thus e.g., during one month on average only 1.5 CO observations at a given location could be used if this selection criterion is applied.

As already stated in several studies (e.g., Buchwitz *et al.*, 2004; Buchwitz *et al.*, 2005; Frankenberg *et al.*, 2005a; Gloudemans *et al.*, 2006; de Laat *et al.*, 2007), clouds can lead to systematic underestimation of the true CO VCDs, because the part of the CO profile below the cloud is shielded. This underestimation becomes especially large for observations over polluted regions (where enhanced CO concentrations exist close to the surface) and/or for high clouds. Even for small cloud fractions the cloud effect can be substantial, because usually (exceptions are e.g. deserts) clouds are much brighter than the surface, and the signal from the clouded part usually dominates the measured spectra. As will be shown later, even for small cloud fractions the related systematic errors can be large (e.g., up to 100% for observations with cloud fraction <20% over polluted regions).

Here it should be noted that in many cases the systematic cloud effect is further enhanced if the SCIAMACHY observations are averaged weighted by the inverse of the retrieval error (e.g., de Laat *et al.*, 2006). Since the retrieval error increases with decreasing brightness of the observed scene, measurements with higher cloud fraction will be systematically stronger weighted and any systematic cloud effect will thus be further increased.

Buchwitz *et al.* have introduced an implicit cloud correction: using a normalization based on the simultaneous retrieved CH_4 absorptions (Buchwitz *et al.*, 2007). However, because of the different height profiles of CO and CH_4 (and probably also because of other differences like the absorption strength), this method can not completely correct for the influence of clouds. Especially in regions with strong CO emissions, the height profiles of CO and CH_4 are particularly different, leading to a systematic underestimation of the true CO VCD. Buchwitz *et al.* (2007) also state that while many retrieval problems are largely improved by the CH_4 normalization procedure, still some systematic effects of the retrieved CO VCD remain.

In this thesis, for the first time an explicit cloud correction for the retrieval of CO VCDs from SCIAMACHY is applied. It is based on results of the FRESCO algorithm and takes into account the (effective) cloud fraction and cloud top height. Besides the correction of the cloud effect, the algorithm also provides height dependent averaging kernels for the individual SCIAMCHY CO measurements. The details of the cloud correction procedure are given in

chapter 5.

After the normalization of the SCIAMACHY CO VCDs and the explicit cloud correction, our CO data set is well suited to be compared in a quantitative way with the results of model simulations.

In this thesis, the SCIAMACHY CO data set for the years 2004 and 2005 are compared to the results from three chemistry climate models: MATCH (Model of Atmospheric Transport and Chemistry, Max-Planck-Institute for Chemistry, (von Kuhlmann *et al.*, 2003)), EMAC (ECHAM5/MESSy Atmospheric Chemistry modeling system, Max-Planck-Institute for Chemistry, (Jockel *et al.*, 2006)) and GEOS-CHEM (Goddard Earth Observing System, (Bey *et al.*, 2001)). In addition MOPITT observations are also used for this comparison. For the observations of both satellite instruments, the respective height-dependent sensitivities were explicitly considered in this comparison by using the corresponding averaging kernels. Besides several regions with intense biomass burning, the comparison is also performed for eastern China, where high CO concentrations from anthropogenic emissions occur. Besides the comparison with the simulated CO distributions from the models, also the temporal variations of the CO emission inventories and fire counts observed from satellite are included in the comparison.

2 Satellite Instruments

2.1 The SCIAMACHY Instrument

Currently, The Scanning Imaging Absorption spectrometer for Atmospheric CHartographY (SCIAMACHY), (Burrows *et al.*, 1995; Bovensmann *et al.*, 1999) which was launched on board the European environmental research satellite ENVISAT (Figure 2.1) is sensitive to all altitude levels of the atmosphere (it should be noted that originally also the MOPITT instrument was designed to measure the CO absorptions in the near IR spectral range. But due to problems with these spectral channels, the MOPITT standard product includes only the results from the thermal channels, see section 2.3). Being sensitive to the boundary layer is a prerequisite to obtain information about regional sources and sinks because they are located near the Earth's surface. This is the reason for the choice of the near-infrared CO absorption band for the DOAS analysis. This is demonstrated by SCIAMACHY's CO column averaging kernel (Buchwitz *et al.*, 2004), which are close to unity throughout the troposphere when there is no cloud. The physical reason why SCIAMACHY has nearly equal sensitivity at all altitudes is that the reflected solar radiation measured by its near infrared channel has passed the entire atmosphere down to the Earth' surface and is then reflected back, since the spectral region used for CO column retrieval is relatively transparent in the atmosphere. However, even a small cloud contamination (cloud fraction smaller than 20%) can significantly reduce SCIAMACHY's sensitivity for trace gases below cloud. The detailed description of the method for handling the cloud effect can be found in chapter 5. Most other existing satellite instruments measure in the thermal infrared and are primarily sensitive to middle and upper tropospheric trace gas concentrations. Thus, SCIAMACHY plays a pioneering role in obtaining a better understanding of the distribution and variation of carbon monoxide by global near-infrared satellite measurements for other missions planned in the near future.

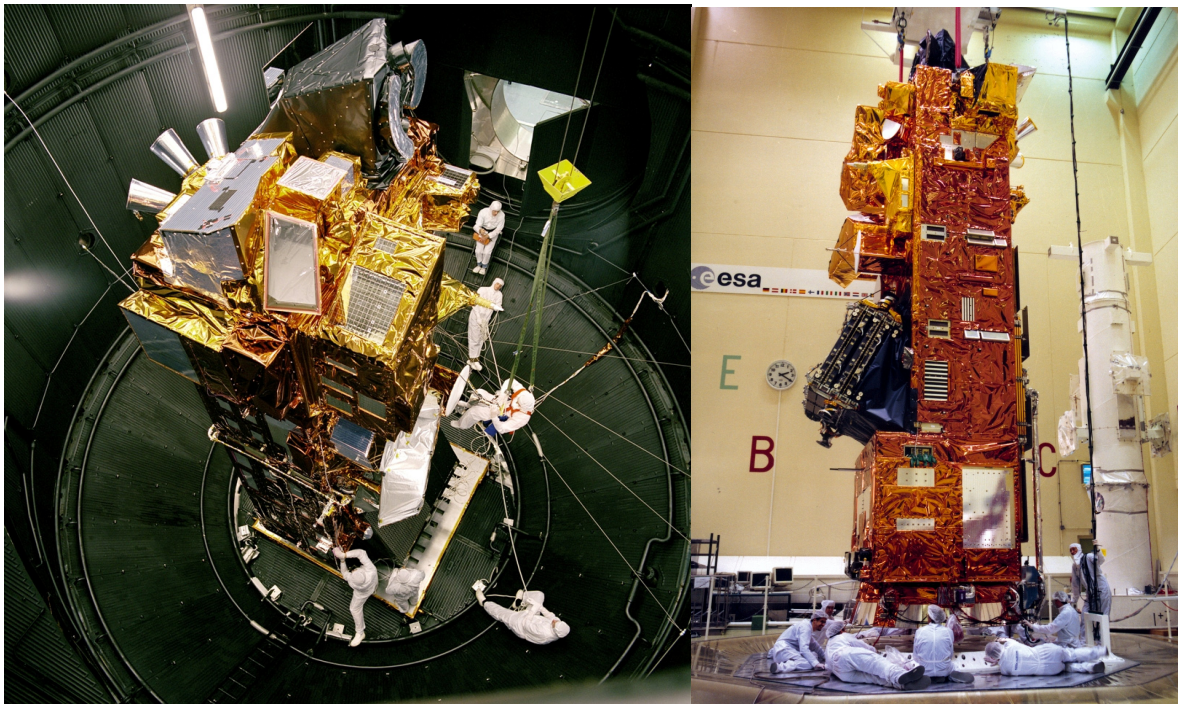

Figure 2.1: ENVISAT in the European Space Research and Technology Centre, ESTEC (photos by ESA).

Table 2.1: Characteristics of SCIAMACHY's spectral channels (Gottwald *et al.*, 2006).

Channel	Spectral Range [nm]	Resolution [nm]	Detector material	Temperature Range [k]
1	214-334	0.24	Si	204.5-210.5
2	300-412	0.26	Si	204.0-210.0
3	383-628	0.44	Si	221.8-227.8
4	595-812	0.48	Si	222.9-224.3
5	773-1063	0.54	Si	221.4-222.4
6	971-1773	1.48	InGaAs	197.0-203.8
7	1934-2044	0.22	InGaAs	145.9-155.9
8	2259-2386	0.26	InGaAs	143.5-150.0

SCIAMACHY is a UV/visible/near-infrared spectrometer with 3 near infrared channels covering wavelengths from 1–1.75µm, 1.94–2.04µm and 2.26– 2.38µm with moderate spectral resolution (0.22–1.5 nm). The details are given in Table 2.1. Due to its relatively high spectral resolution and the wide wavelength range, SCIAMACHY detects many different trace gases in the atmosphere, such as O_3, SO_2, and NO_2 (Figure 2.2).

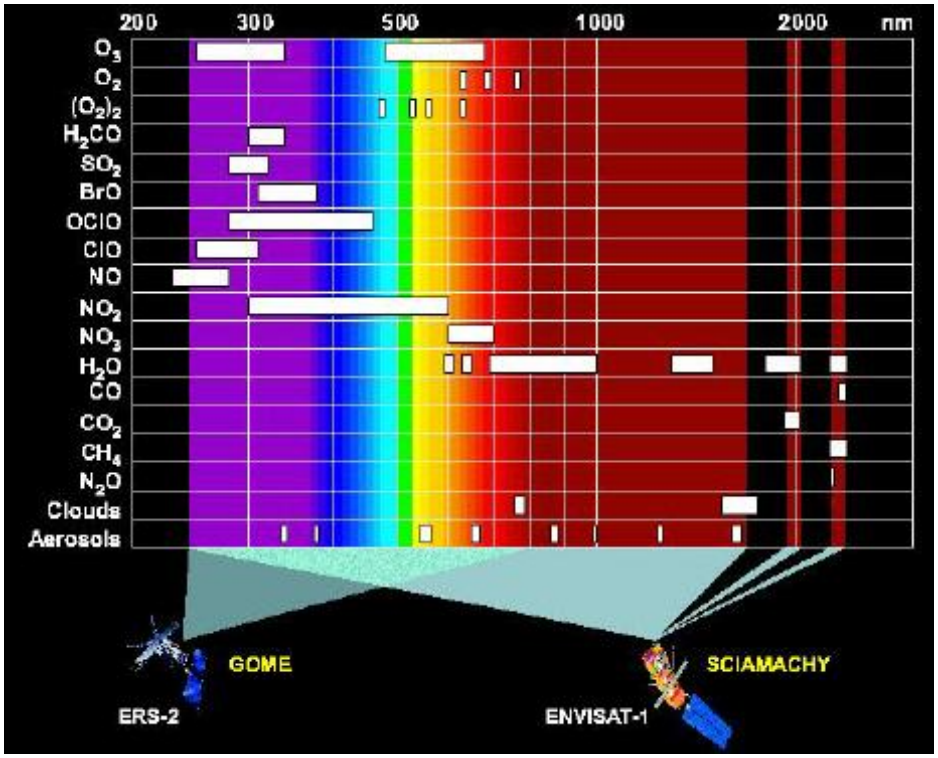

Figure 2.2: The spectral range of SCIAMACHY and GOME and corresponding trace gas absorption bands (Gottwald *et al.*, 2006).

SCIAMACHY measurements alternate between limb and nadir mode. In the nadir mode the field of view faces downward to the Earth's surface scanning across the sub-satellite track. The swath of 960 km gives full global coverage every six days (14 orbits per day; see Figure 2.3 for an example of an orbit and the swath). The typical ground pixel size of SCIAMACHY is 30km (along track, i.e. approx. north-south) times 60 to 120km (across track, i.e. approx. east-west). For the CO retrieval, the typical ground pixel size is 30 km (along track) times 120 km (across track). In limb mode scattered light above the horizon is measured as function of tangent height allowing the determination of trace gas profiles. The limb/nadir matching performed by SCIAMACHY provides the possibility to measure the same atmospheric volume

both in nadir and limb geometry within one orbit, yielding three-dimensional information about the atmosphere, as shown in Figure 2.3.

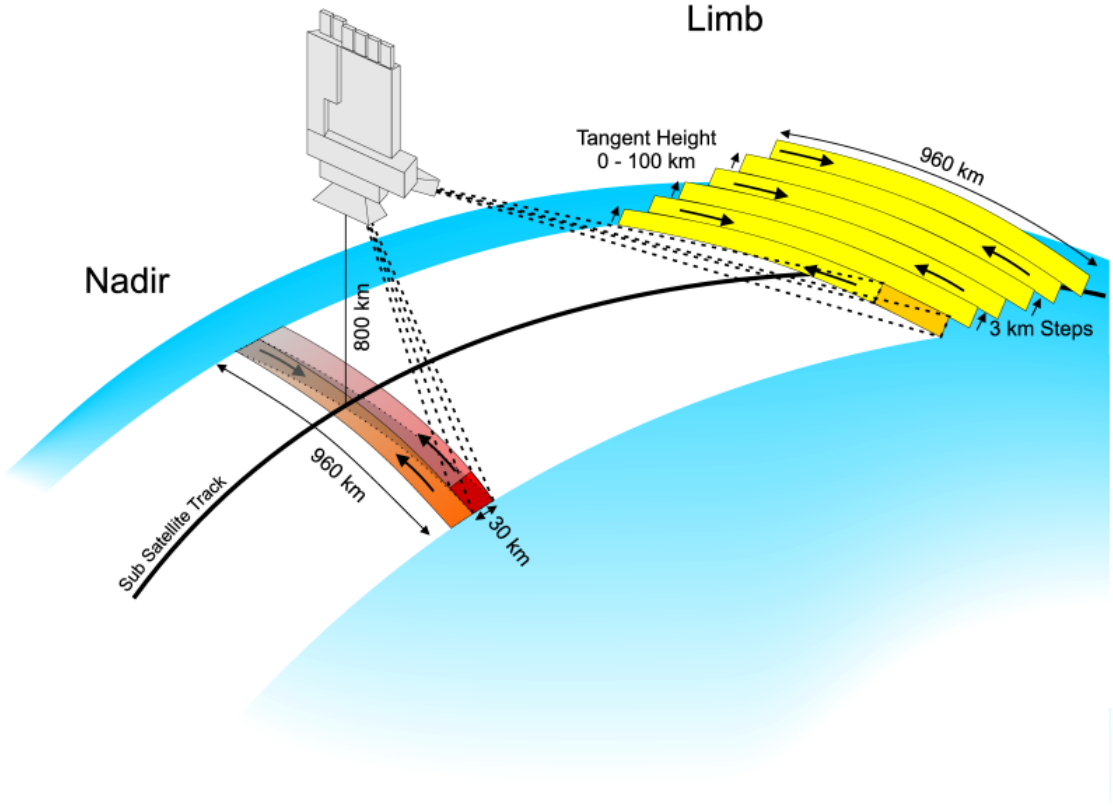

Figure 2.3: Nadir and limb scanning strategy of SCIAMACHY (Gottwald *et al.*, 2006).

The optical configuration of SCIAMACHY is shown in Figure 2.4. The incoming light enters the instrument alternatively via the nadir, limb or sub solar port depending on scan mode, and is focused on the entrance slit of the spectrometer. After leaving a predisperser prism a geometrical channel separator splits the resulting weakly dispersed intermediate spectrum and directs the light to the 8 spectral channels depending on the spectral range using reflective optics and a dichroic mirror. Overall, the in-flight optical performance of SCIAMACHY is very similar to that predicted from the pre-flight on the ground characterization and calibration activities (Gottwald *et al.*, 2006). One exception is a time dependent optical throughput variation in the SCIAMACHY NIR/SWIR channel 7, which has many resolved CO_2 absorption features, and channel 8, which has many CO and CH_4 features. This results from the in-flight deposition of ice on the cooled detectors. As ice absorbs and scatters radiation at these wavelengths, this adversely affects the trace gas retrieval: not only by reducing the signal-to-noise ration, but also by changing the slit function (Gloudemans *et*

al., 2005; Buchwitz *et al.*, 2005). Therefore, it was evaporated by heating the detector every 3~6 months to alleviate the loss of signal, as shown in Figure 2.5. However, the slit function (width and shape) behaves differently during each of these decontamination procedures, which significantly affects the retrieval of trace gases from the near-infrared channels. Several methods have been developed to deal with this problem. They will be introduced and compared in chapter 6 and chapter 7.

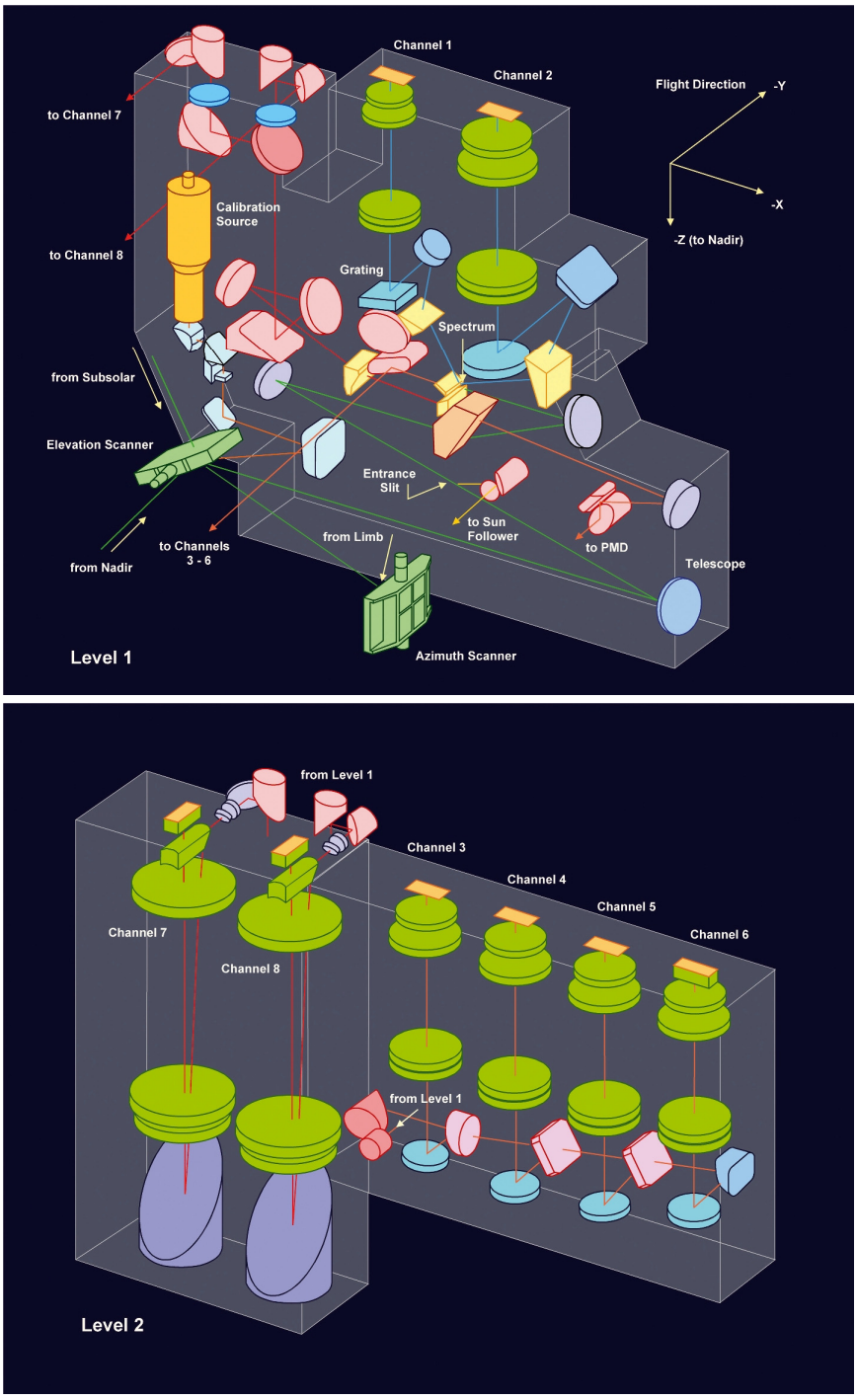

Figure 2.4: Optical configuration of SCIAMACHY (graphics: DLR-IMF, modified after SJT 1996).

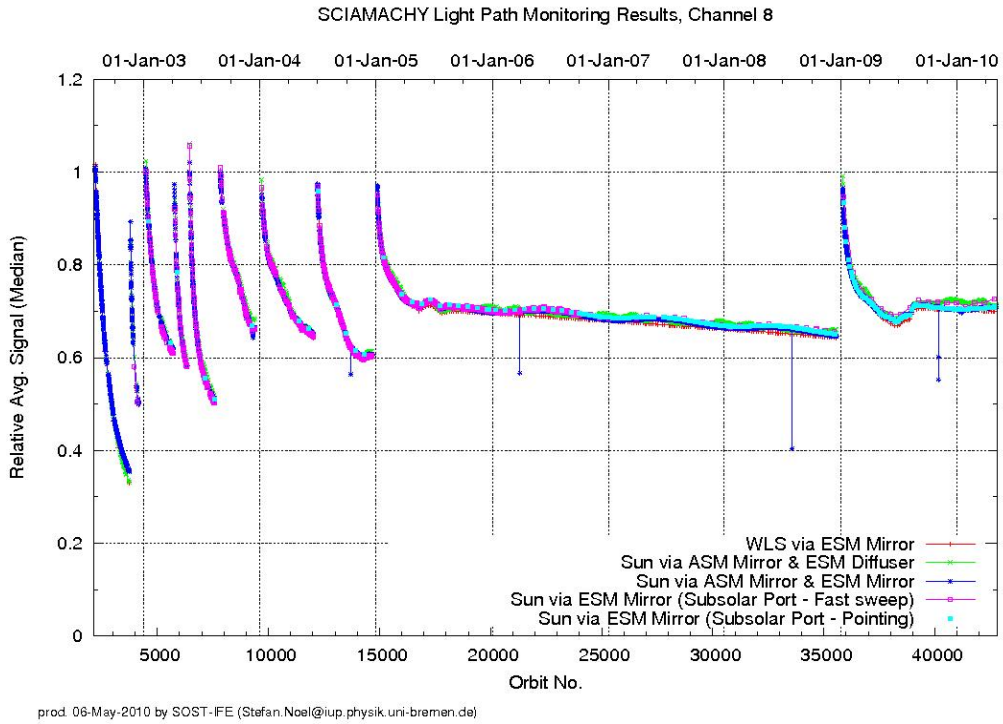

Figure 2.5: SCIAMACHY Light Path Monitoring Results, Channel 8 (prod. 16-Jun-2010 by SOST-IFE (Stefan.Noel@iup.physik.uni-bremen.de)).

2.2 The SCIAMACHY Near-infrared Detectors

From a technological viewpoint, spectrometry (using image arrays) in the near infrared is a challenging task. At the time SCIAMACHY was planned, the now common detector material Indium Gallium Arsenide (InGaAs) was still very experimental and especially the extension of the wavelength range to nearly 2.4 µm was very difficult. Compared to classical silicon detectors used in the UV and visible, the major drawbacks of the SCIAMACHY InGaAs detector pixels are a substantially higher pixel-to-pixel variability in quantum efficiency and a more predominant dark (leakage) current. Hence, the correction for dark current as well as the identification of dead or bad pixels had to be implemented in the retrieval scheme of this work.

In channel 8 where the CO fitting window lies, an additional problem occurs. It has been found that water vapor has somehow infiltrated the satellite. Since the detectors of channel 8 are the coolest elements (150K) of the SCIAMACHY instrument, the water vapor

resublimation occurs on the surfaces of these detectors. This ice layer has two impacts, first it reduces the transmission and second, it alters the instrumental line-shape and the dark current as photons are scattered within the ice layer (see Gloudemans *et al.*, 2005 and references therein). From time to time, SCIAMACHY is heated in order to get rid of the ice layer. However, after these decontamination periods, the ice layer starts to rebuild once the detectors are at nominal temperature. Thus, the problem of transmission and line-shape distortion depends strongly on time. For the retrieval of carbon monoxide, there is no way to circumvent this problem since strong absorption lines are only present in channel 8. There are several correction methods developed by different groups, but no consistent time series could be retrieved so far. Thus, a completely different strategy was chosen which will be described in chapter 7.

Furthermore, as Figure 2.6 shows, due to moderate spectral resolution of SCIAMACHY, the absorption of retrieved species can not be fully resolved and compared with CH_4 and H_2O, the absorption of CO are much weaker, which make the retrieval of CO from SCIAMACHY challenging.

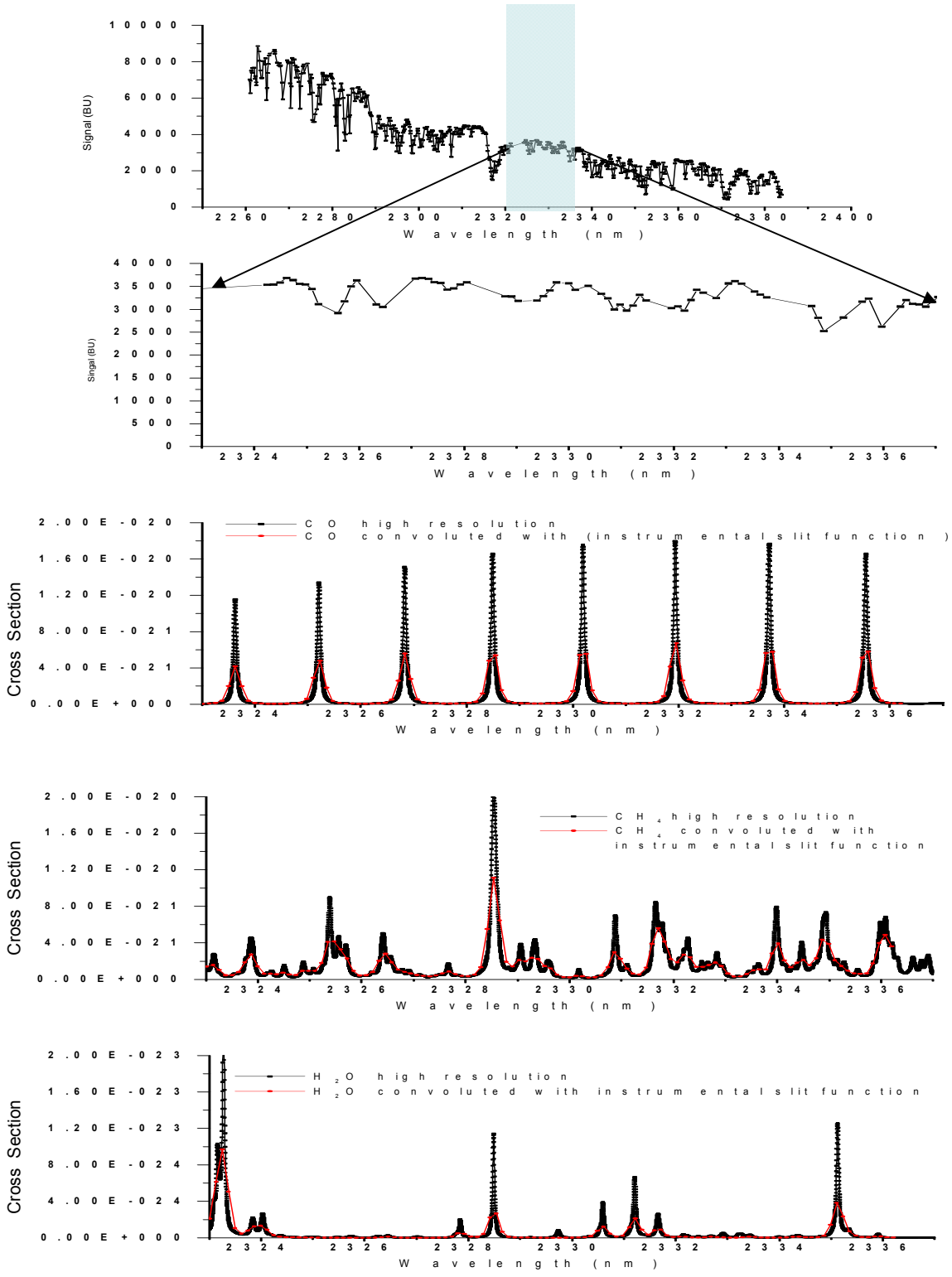

Figure 2.6: Exemplary averaged SCIAMACHY measurements over the Sahara on the 3rd of February 2004 (20°N ~ 28°N; 8°W ~ 28°E). The upper two rows show SCIMACHY signal (with dark current corrected and dead/bad pixels masked). The third row shows the cross section of CO with and without convolution with the instrumental slit function; the forth and the fifth rows show the respective cross sections for CH_4 and for H_2O.

2.3 The MOPITT Instrument

The Measurements of Pollution In The Troposphere (MOPITT) experiment was launched on December 18th 1999, onboard the NASA EOS-Terra satellite. It is a downward looking (nadir view) infrared radiometer which targets measurements of carbon monoxide (CO) and methane, providing a horizontal resolution of 22 km by 22 km. Terra is in a 705 km, sun-synchronous orbit with a 10:30am equator crossing time, which together with the MOPITT swath width, of about 600km, means that total global coverage can be achieved in approximately 3 days. The primary objective of MOPITT is to enhance knowledge of the lower atmosphere system and particularly interactions with the surface/ocean/biomass systems. The particular focus is on the distribution, transport, sources and sinks of CO and CH_4 in the troposphere. In this thesis, CO measurements are only used for comparison with SCIAMACHY. A more complete description of the MOPITT instrument can be found in the MOPITT mission description document (Drummond and Mand, 1996).

The MOPITT instrument makes CO measurements in two spectral regions, thermal infrared emission at 4.7 μm and reflected solar radiation at 2.3 μm. This thesis will concentrate on the thermal infrared channels only, since the CO retrieved from solar channels are not currently delivered for public downloading. The 4.7 μm region covers the R branch of the CO (0-1) fundamental band in the spectral region 2110-2230 cm^{-1}. In this region, the solar spectrum is relatively weak and the ground reflectivity is low, ~2% over the ocean (Edwards *et al.*, 1999). The top of the atmosphere radiance in this region is therefore dominated by thermal emission from the surface and the atmosphere. Table 2.2 shows how the MOPITT instrument makes use of two PMCs (Pressure Modulation Cells) and four LMCs (Length Modulation Cells) to form eight spectral channels; six are designed to be used for the CO retrievals and two for CH_4. By using a series of PMRs and LMRs at different cell pressures the MOPITT instrument is able to obtain information on the vertical distribution of CO by sampling different parts of the line wings.

Table 2.2: The MOPITT instrument channel characteristics, numbers in parentheses denote standard deviation, adapted from the NCAR MOPITT web site. (http://www.eos.ucar.edu/mopitt).

Channel Number	Primary Purpose	Modulator Type and Number	Cell Pressure (mb)	Cell Temperature (K)	Cell Length (mm)	Centre Wavenumber (cm^{-1})
1	CO	LMC1	200	300	2-10	2166 (52)
2	CO	LMC1	200	300	2-10	4285 (40)
3	CO	PMC1	50-100	300	10	2166 (52)
4	CH_4	LMC2	800	300	2-10	4430 (140)
5	CO	LMC3	800	300	2-10	2166 (52)
6	CO	LMC3	800	300	2-10	4285 (40)
7	CO	PMC2	25-50	300	10	2166 (52)
8	CH_4	LMC4	800	300	2-10	4430 (140)

2.4 MOPITT CO Measurements

Daytime MOPITT Version 4 data (http://eosweb.larc.nasa.gov/PRODOCS/mopitt) are used in this thesis for comparison with SCIAMACHY CO columns and model CO columns. The MOPITT retrieval algorithm is based on the Maximum a Posteriori solution (Deeter *et al.*, 2003), which depends explicitly on both the *a priori* state vector, which represents the statistically most probable state, and the *a priori* covariance matrix, which describes the statistical variability relative to that state. Compared to the previous version, an important improvement of MOPITT version 4 data is that, instead of fixed *a priori* profiles, *a priori* profiles, which vary geographically and temporally, are used for each retrieval.

MOPITT derives CO profiles from longwave thermal radiation emitted by the Earth's surface and atmosphere and its sensitivity to the lower troposphere directly depends on the temperature differences between the ground and the troposphere. MOPITT observations are predominantly sensitive to the middle troposphere (Deeter *et al.*, 2003). The sensitivity to the lower troposphere below 700hpa is strongly reduced, especially in the cases of could surface temperatures.

MOPITT CO total columns and corresponding total column averaging kernels are calculated from CO profiles using the procedure as described by (Emmons *et al.*, 2004). Only cloud free MOPITT measurements are available. The clear/cloudy determination is based on both the MOPITT radiances themselves and a 'cloud mask' produced from near-simultaneous observations by the Terra/MODIS ("MODerate resolution Imaging Spectroradiometer") instrument. The error of the MOPITT total column measurements is generally less than 20% and consists of a smoothing error, model parameter error, forward model error and an error due to instrument noise. The MOPITT instrument noise error itself is only a few percent (Pan *et al.*, 1998).

3 Infrared Spectroscopy

The content of this chapter is largely adopted from standard textbooks (Herzberg, 1989; Haken and Wolf, 2006) and the thesis of Schneising (2008)

3.1 Basics of Spectroscopy

Spectroscopy deals with the interaction between matter and electromagnetic radiation through absorption, emission, and scattering of the latter. Radiation can be characterized by its energy which is linked to frequency by Planck's relation.

$$E = h\upsilon \qquad 3.1$$

The electromagnetic spectrum (Figure 3.1) classifies electromagnetic radiation according to specific wavelength or rather frequency ranges. These quantities can be converted by the simple formula.

$$\nu = c / \lambda \qquad 3.2$$

Commonly used in spectroscopy is also the wavenumber defined as

$$\tilde{\nu} = 1 / \lambda \qquad 3.3$$

The part of the electromagnetic spectrum between the visible and microwave regions is referred to as the infrared spectrum commonly being subdivided in spectroscopy as follows: The region from 0.7µm to 1.4µm is denoted near-infrared (NIR), the short-wave infrared (SWIR) ranges from 1.4µm to 3µm, and the interval from 3µm to 15µm is called thermal infrared (TIR), while the spectral interval from 15µm m to 1mm is referred to as far-infrared (FIR). The differentiation between NIR and SWIR is somewhat arbitrary and in this study near-infrared therefore refers to the entire spectral range from 0.7µm to 3µm to simplify matters covering all considered absorption bands of carbon monoxide relevant for the retrieval presented here.

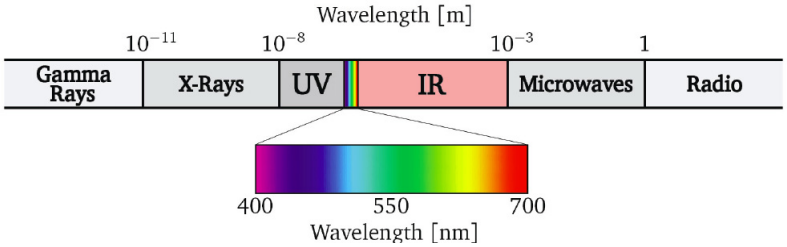

Figure 3.1: The electromagnetic spectrum (Schneising, 2008).

Molecular absorption spectra result from conversion of radiative energy to excitation of the molecule by rotational, vibrational or electronic transitions. The spacings of available energy levels of the molecule have to match the energy of the incident radiation; otherwise the species will be transparent to that radiation. While rotational energies of the molecule correspond to the far-infrared or microwave region, vibrational energies are located in the NIR/SWIR or TIR region. Electronic transitions correspond to energies in the visible, ultraviolet or X-ray wavelength range.

In contrast to thermal infrared spectroscopy which uses thermal emission from the earth's surface and the atmosphere, near-infrared spectroscopy benefits from the absorption of reflected, backscattered or transmitted solar radiation in the atmosphere and is normally based on corresponding coupled rotational and vibrational excitation of the molecules with the vibrational spectra containing fine structure according to the rotational sublevels. Due to the coupling the spectra exhibit high complexity. Rarely, also electronic transitions such as in oxygen are involved.

3.2 Molecular Rotations and Vibrations

A molecule which consists of n atoms has 3n degrees of freedom, whereof three are translational and three are rotational in a nonlinear molecule. A linear molecule only has two rotational degrees of freedom because the degree of freedom associated with spinning along the line of centres of the atoms is frozen out which is due to the very small moment of inertia I along this axis and the inverse dependence of energy on it according to (with J being the total angular momentum quantum number)

$$E_{rot} = \frac{\hbar^2}{2I} J(J+1) \qquad 3.4$$

resulting in very widely spaced rotational energy levels greater than the binding energy. The remaining degrees of freedom then correspond to fundamental vibrations amounting to 3n−5 in the linear and 3n−6 in the nonlinear case. The actual amount of spectral bands due to fundamental vibrational modes can be smaller because of degeneration caused by symmetry.

Commonly observed near-infrared transitions are of rotational-vibrational nature. The corresponding spectra are a result of transitions from rotational levels of a specific vibrational state (described by the vibrational quantum number v) to rotational levels of another vibrational state without changing the electronic state. $((\nu', J') \rightarrow ((\nu'', J''))$ For the absorption to take place there has to be a periodic change in the electric dipole moment of the molecule during the vibration, otherwise the corresponding band is not observed in the infrared absorption spectrum (infrared-inactivity).

Assuming that the interaction between rotation and vibration is negligible, the rotational and vibrational contributions to the energy of the molecule can be considered independently. Using the approximations of harmonic oscillator and rigid rotor, one gets therewith for a symmetric top molecule, which is a molecule in which two moments of inertia are the same ($I_A \neq I_B \neq I_C$) having two equal principal moments of inertia.

$$E_{vib,rot} = E_{vib} + E_{rot} = (v + \frac{1}{2}) h\nu_0 + hcBJ(J+1) + hc(A-B)K^2 \qquad 3.5$$

Where A and B are the rotational constants with respect to the moments of inertia about the axis of symmetry and about an axis perpendicular to the axis of symmetry. v is the vibrational quantum number, ν_0 is the vibration frequency, J the quantum number of the total angular momentum, and K=− J, . . . , J the quantum number of the component of angular momentum about the axis of symmetry (i.e., projection of J on the symmetry axis).

Vibrational modes in a symmetric top differ according to the orientation of the oscillating dipole moment relative to the top axis and the corresponding bands are referred to as parallel and perpendicular. The selection rules are Δv =±1 and

Parallel bands: $\Delta J = \pm 1; \quad \Delta K = 0 \quad$ for $K = 0$ 3.6

$\Delta J = 0, \pm 1; \quad \Delta K = 0 \quad$ for $K \neq 0$ 3.7

Perpendicular bands: $\Delta J = 0, \pm 1; \quad \Delta K = \pm 1$ 3.8

Pure rotational transitions ($\Delta v = 0$) are also possible if the molecule has a permanent electric dipole moment.

Special cases of the symmetric top are linear (I_B=I_C; I_A=0) and spherical top (I_A=I_B=I_C) molecules. For linear molecules holds K=0 (no rotation about the molecular axis accordant to the frozen out rotational degree of freedom mentioned above) and for spherical tops A=B so that (3.5) reduces to

$$E_{vib,rot} = (v + \frac{1}{2}) h \nu_0 + hcBJ(J+1) \quad 3.9$$

respectively. The degeneracy of each energy level is 2J+1 in the linear case and $(2J+1)^2$ for spherical tops. According to the selection rules given above, $\Delta J = \pm 1$ for parallel bands of linear molecules (i.e., stretching vibrations) whereas for perpendicular bands which are associated to a change of dipole moment perpendicular to the molecular axis (i.e., bending vibrations) also $\Delta J = 0$ is possible. Transitions with $\Delta J = -1$ and $\Delta J = +1$ are referred to as P-branch and R-branch, respectively; transitions with $\Delta J = 0$ are denoted as the Q-branch, which is - if present – rather strong because of many overlapping lines due to $\Delta B / B'' \leq 1$ concentrated near the band center between the P- and R-branches. The involved transitions are illustrated in Figure 3.2.

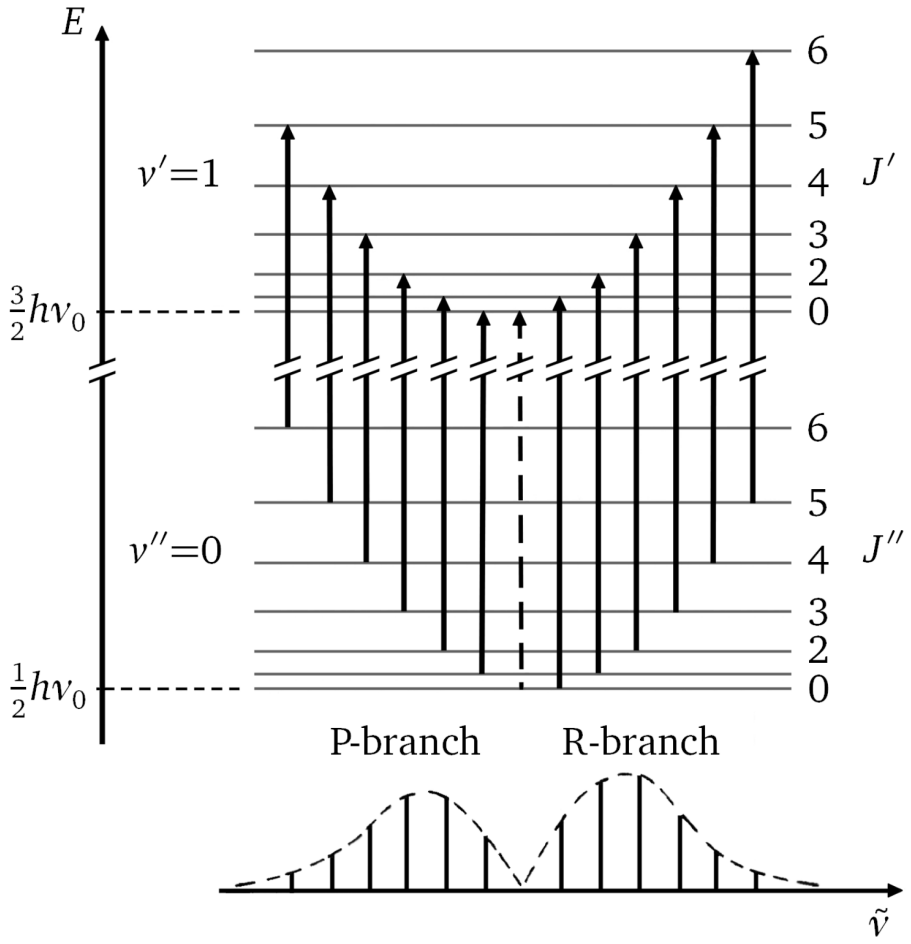

Figure 3.2: Schematic rotational-vibrational molecular spectral band and corresponding transitions. The P- and R-branches are consequences of transitions with $\Delta J = -1$ and $\Delta J = +1$, respectively. In local thermodynamic equilibrium there is typically only thermal population in the lowest vibrational state with $\nu'' = 0$. The relative amplitudes of the spectral lines scale as the population of the rotational sublevels J''. (This plot has been obtained from Haken and Wolf, 2006).

Unlike linear molecules where a Q-branch is only allowed for bending vibrations or when the molecule has a triplet ground state, i.e., unpaired electron spins contributing to angular momentum about the molecular axis, for a spherical top there is a Q-branch for both parallel and perpendicular bands. The Q-branches of different K-values all lie on top of each other (only very slightly displaced due to centrifugal distortion) with P- and R-branches to either side as in the linear case. For a general symmetric top with $I_A \neq I_B$ the PQR-branches of a perpendicular band would be spread out according to K due to $\Delta K = \pm 1$ and (3.5) leading to a very complex

spectrum with spacing 2(A−B) of the Q-branches but since A=B for a spherical top they overlap near the band center because the energy levels do not depend on K.

The rigid rotor approximation predicts lines with a constant distance of 2B in the observed spectrum, whereas realistic measurements reveal slightly decreasing spacing in the R-branch as the wavenumber increases and increasing spacing in the P-branch as the wavenumber decreases due to the fact that bonds in molecules are not entirely rigid because of the vibrational coupling. Anharmonicity additionally causes overtone bands resulting from $\Delta v = \pm 2, \pm 3, \pm 4, \ldots$ with decreasing intensity.

Besides the selection rules, the relative amplitude of the spectral lines in a given band depends on the degree of degeneracy and the population of the rotational level of the lower state (v'', J''). In local thermodynamic equilibrium the thermal population is given by the Boltzmann distribution, hence

$$\frac{N_J}{N_0} = \frac{g_J}{g_0} \exp\left(-\frac{E_J - E_0}{k_B T}\right) = g_J \exp\left(-\frac{hcBJ(J+1)}{k_B T}\right) \qquad 3.10$$

with degeneracy g_J, i.e., number of states having energy E_J. For small J the degeneration term ((2J+1) for linear and $(2J+1)^2$ for spherical top molecules) dominates and the population NJ increases with J, whereas for greater J the population decays exponentially with increasing J. Thus, a population maximum is obtained for a specific J depending on temperature and rotational constant. Since there is typically no thermal population in the upper state (v', J') the spectral line intensities scale as the population of the rotational sublevels of the lower vibrational state according to (3.10) with $J = J''$. The intensities of transitions can also be affected by nuclear spin in molecules with inversion symmetry. Given for example the linear molecule $^{12}C^{16}O_2$, the exchange of the identical ^{16}O nuclei corresponds to a symmetric total wave function if J is even and to an antisymmetric wave function if J is odd. Since the nuclei have zero spin, the Bose-Einstein statistics requires symmetric behavior under nuclear exchange explaining why only spectral lines originating from energy levels with even J are observed.

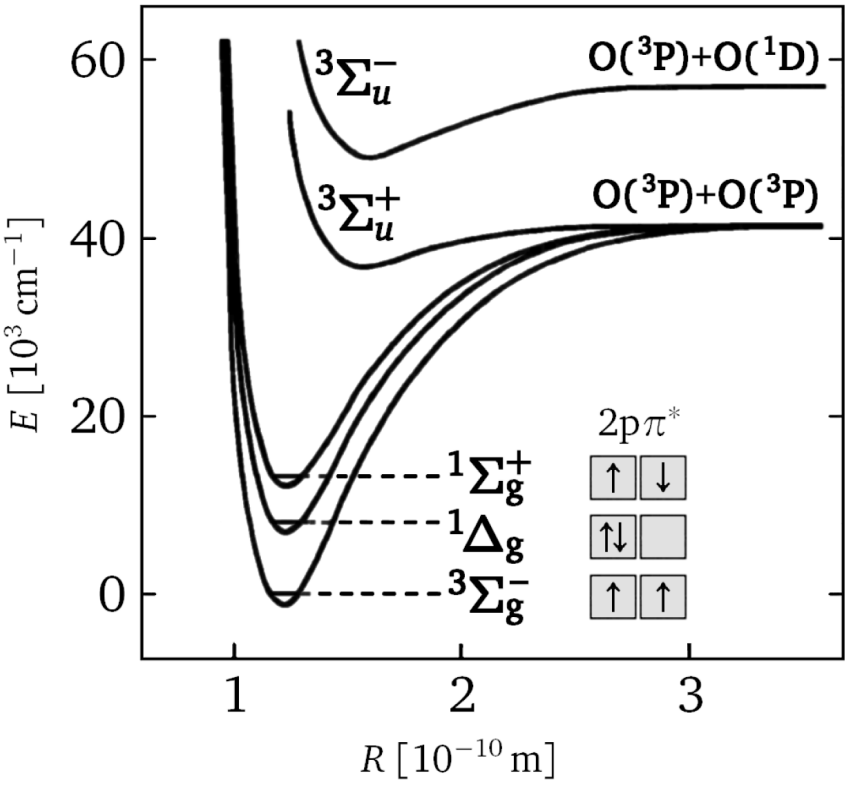

Figure 3.3: Potential curves for the lowest electronic states of molecular oxygen. (This plot has been obtained from Herzberg , 1989).

3.3 Carbon Monoxide Properties

The bond length between the carbon atom and the oxygen atom is 112.8 pm (Gilliam *et al.*, 1950). Atomic formal charge and electronegativity result in a small bond dipole moment with the negative end of the molecule on the carbon atom (Kutzelnigg, 2002). This is due to the highest occupied molecular orbital having an energy much closer than that of the carbon's p orbitals, despite the oxygen's greater electronegativity. This means that the greater electron density is found near the carbon atom. In addition, carbon's lower electronegativity creates a much more diffuse electron cloud, enhancing the polarizability. This is also the reason why almost all chemistry involving carbon monoxide occurs through the carbon atom, and not the oxygen.

The bond length of CO is consistent with a partial triple bond, and the molecule can be represented by three resonance structures:

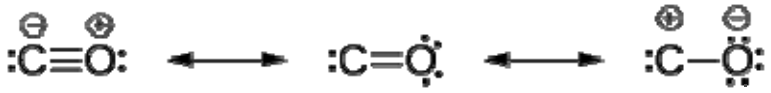

Figure 3.4: Structures of carbon monoxide (Kutzelnigg, 2002).

In this study, the leftmost structure contributes the most. Carbon monoxide resembles molecular nitrogen (N_2), and it has nearly the same molecular mass. The boiling point (82 K) and melting point (68 K) are very similar to those of N_2 (77 K and 63 K respectively). The bond dissociation energy of 1072 kJ/mol is stronger than that of N_2 (942 kJ/mol) and represents the strongest chemical bond known "National Standard Reference Data Series", National Bureau of Standards (Darwent, 1970).

The oxidation state of carbon in carbon monoxide is +2 in each of these structures. It is calculated by counting all the bonding electrons as belonging to oxygen, which is more electronegative than carbon. Only the two non-bonding electrons on carbon are assigned to carbon. In this count carbon then has only two valence electrons in the molecule compared to four in the free atom, so that its oxidation state is +2, and the molecule may be called carbon (II) oxide.

3.4 IR Spectrum of Carbon Monoxide

The infrared (IR) spectrum of a simple heteronuclear diatomic molecule reveals a series of regularly spaced peaks. A typical spectrum is illustrated in Figure 3.5 (the IR spectrum of carbon monoxide looks much like this spectrum).

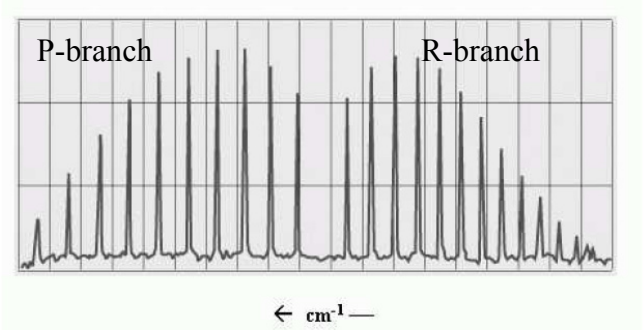

Figure 3.5: A typical simple heteronuclear diatomic spectrum in the infrared (IR) (Grubbs, 2010).

To understand the information contained in the CO spectrum, the vibrational and rotational energy levels of the molecule must be taken into account.

To a first approximation, the vibration of the carbon-oxygen bond is well described by the harmonic oscillator model. The energy levels of a harmonic oscillator are given by

$$E_\nu = \omega(\nu + \frac{1}{2}) \tag{3.11}$$

Where υ is the vibrational quantum number (0, 1, 2 ….) and ω is the harmonic frequency of oscillator. This frequency can in turn be calculated from

$$\omega = \sqrt{\frac{k}{\mu}} \tag{3.12}$$

Where k is the spring constant of the bond and μ is the reduced mass of the diatomic,

$$\mu = \frac{m_C m_0}{m_{C+} m_0} \tag{3.13}$$

The rotational energy levels of CO can be described using the rigid rotor model, which has energies

$$E_J = BJ(J+1) \tag{3.14}$$

Where J is the rotational quantum number (0, 1, 2, 3 …) and B is the rotational constant,

$$B = \frac{\hbar^2}{2I} = \frac{\hbar^2}{2\mu R^2} \tag{3.15}$$

In equation 2.4.5, I represent the moment of inertia and R the equilibrium bond distance.

The combined rotational-vibrational energy (ro-vibrational energy) can be obtained by adding equations (1) and (4) which yields

$$E_{\nu,J} = \omega(\nu + \frac{1}{2}) + BJ(J+1) \tag{3.16}$$

When a diatomic molecule absorbs a photon of IR light, there can be a simultaneous change in vibrational and rotational quantum number. However, not all transitions are permitted. The selection rules that apply to this system tell us that only transitions whereby $\Delta\upsilon = \pm 1$ and $\Delta J = \pm 1$ are allowed. At room temperature, nearly all of the CO molecules reside in their ground vibrational state ($\upsilon = 0$), so the vibrational transition that predominates is the $\upsilon = 0$ to 1 transition. But a wide range of rotational states are thermally occupied within the ground vibrational state, so several $\Delta J = \pm 1$ rotational transitions can coincide with the $\upsilon = 0$ to 1 jump. Using equation

3.16, a theoretical expression for this energy difference is derived as follows:

$$\Delta E_{J''} = [\omega(\frac{1}{2}) + B(J''+1)(J''+2)] - [\omega(\frac{1}{2})B(J''-1)(J'')] \quad 3.17$$

Figure 3.6 shows a number of ro-vibrational energy levels for CO. By convention, ground state parameters are identified with double prime and excited state parameters with a single prime. Of the transitions that can occur between the v'' and v' level, some will involve a decrease in rotational quantum number (ΔJ= -1) and the others will involve an increase (ΔJ = +1). The peaks in the IR spectrum that arise from ΔJ = -1 transitions are called P-branch transitions and the ΔJ = +1 transitions are called R-branch transitions (three possible P-branch and three possible R-branch transitions are shown in Figure 3.6).

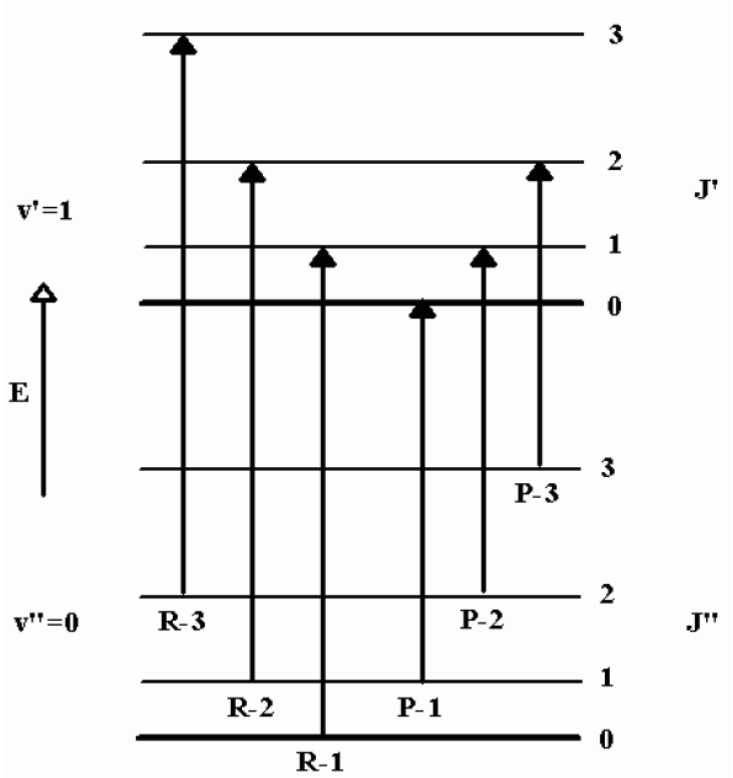

Figure 3.6: Three possible P-branch and three possible R-branch transitions of CO (Grubbs, 2010).

Referring back to Figure 3.5, the P-branch transitions give rise to a series of peaks that appear at lower wave numbers. The R-branch series appears at higher wave numbers. There appears to be a peak missing between these two series; no peak appears here because ΔJ = 0 transitions are not allowed. Investigation of more possible transitions of CO is beyond this thesis, which is left to the specialized literature.

4 Retrieval Algorithm

4.1 DOAS

Carbon Monoxide (CO) exhibits spectral lines due to vibrational-rotational transitions in the wavelength range of 2323nm ~ 2338nm. Thermal emission from the Earth can be neglected compared to reflected solar radiation in the near infrared. Therefore, in general trace gas concentrations can be retrieved by means of differential optical absorption spectroscopy (DOAS) (Platt and Wiley, 1994), which is based on the well known Beer-Lambert law:

$$dI(\lambda) = -I(\lambda)c(s)\sigma(\lambda, p, T)ds \qquad 4.1$$

Here $\sigma(\lambda, p, T)$ is the absorption cross section of the absorbing species which depends on wavelength λ, pressure p and temperature T. c (s) is its concentration along the light path s.

Integration of equation (4.1) for a finite light path through the absorbing species yields the relationship between the incident light intensity $I_0(\lambda)$ and the transmitted light intensity $I(\lambda)$:

$$I(\lambda) = I_0(\lambda)\exp(-\tau) \qquad 4.2$$

The logarithm of the ratio of the measured I and I_0 is called optical density $\tau(\lambda)$

$$\tau(\lambda) = -\ln\left(I(\lambda)/I_0(\lambda)\right) = \int \sigma(\lambda, p, T)c(s)ds. \qquad 4.3$$

In case of multiple absorbers, equation 4.2 has to take into account optical densities of several absorbing species:

$$I(\lambda) = I_0(\lambda)\exp(-\sum_i \tau_i), \qquad 4.4$$

Where τ_i denotes the optical density of the absorber i.

If σ does not strongly depend on temperature and pressure (or if temperature and pressure along the path ds are constant):

$$\tau_i(\lambda) = \int \sigma_i(\lambda, p, T)c_i(s)ds \approx \sigma_i(\lambda)\int c_i(s)ds \qquad 4.5$$

$$W_i = \int c_i(s)ds \qquad 4.6$$

W is the concentration of the absorbing gas i integrated along the light path and usually called the "Slant Column Density" (SCD).

To solve equation 4.4, the contributions of all trace gases with significant absorption in the selected wavelength range need to be taken into account (including the so-called Ring spectrum accounting for inelastic scattering that leads to a filling-in of strong Fraunhofer lines). In addition, the Rayleigh scattering, Mie scattering and surface absorption should be included, for they also contribute to the total extinction within the atmosphere. The key principle of DOAS is to discriminate between high-frequency absorptions of atmospheric molecules and low-frequency absorptions due to, e.g., scattering processes, since the absorptions due to transitions (electronic, vibrational or rotational) of atmospheric molecules strongly varies with wavelength. In the spectral fitting process, the low-frequency extinction is simply modeled by a low order polynomial. Therefore, the total optical density $\tau_{tot}(\lambda)$ can be written as:

$$\tau_{tot}(\lambda) = -\ln\left(I(\lambda)/I_0(\lambda)\right) = \sum_i W_i \cdot \sigma_i(\lambda) + \sum_{x=0}^{n} a_x \lambda^x \qquad 4.7$$

Where $a_x\lambda^x$ represents the xth terms of a polynomial of nth degree.

The parameter vectors $\vec{W}$ and $\vec{a}$ could be retrieved by minimizing χ^2 (the squared Euclidian norm $\|\cdot\|_2$ of the residual vector):

$$\chi^2(\vec{W},\vec{a}) = \left\| \ln\left(\frac{I(\lambda)}{I_0(\lambda)}\right) + \sum_i W_i \cdot \sigma_i(\lambda) + \sum_{x=0}^{n} a_x \lambda^x \right\|_2^2 \rightarrow \min \qquad 4.8$$

Since the system of equations is strongly over determined, the linear least squares approach is suitable in this case. A detailed description of the DOAS fitting routine is given by Platt and Wiley (1994), Leue *et al.* (2001) and Wenig (2001).

4.2 The Characteristic of the Trace Gas Cross Sections in Near Infrared.

Spectral absorption of molecules in the near infrared region is mainly due to vibrational and rotational transitions (see chapter 3) whose ground state population distribution strongly depends on temperature and pressure. Thus, in contrast to the UV/Vis spectral region, it becomes indispensable to consider the temperature and pressure dependence of the cross sections in near

infrared.

In the case of local thermodynamic equilibrium, the absorption cross section of a single transition line $\sigma_i(\nu)$ can be written as the product of the line intensity S_i and a frequency dependent part determining the line shape $\phi_i(\nu)$ (Thomas and Stamnes, 1999).

$$\sigma_i(\nu) = S_i \phi_i(\nu) \tag{4.9}$$

In the near-infrared range, the line shape is not only determined by Doppler broadening (Gaussian shape) but also determined by pressure broadening (Lorentzian shape).

Doppler broadening is caused by the relative speed of the absorbing molecules with respect to the incident light source which leads to a small Doppler shift of the absorbed frequency. The line shape of a purely Doppler broadened line can be described by a Gaussian function (Thomas and Stamnes, 1999; Goody and Yung, 1989):

$$\phi_D(\nu) = \frac{1}{\sqrt{\pi}\gamma_D} e^{-(\nu-\nu_0)^2/\gamma_D^2} \tag{4.10}$$

Where

$$\gamma_D = \frac{\nu_0}{c}\overline{|\nu|} = \frac{\nu_0}{c}\sqrt{2k_B T/m} \tag{4.11}$$

with

m = molecular weight,

k_B = Boltzmann constant

c = the speed of light

υ = the observed frequency

υ_0 = the rest frequency

Pressure broadening is caused by optical collisions between molecules which effectively reduce the life time of the upper state (Thomas and Stamnes, 1999) and could be described by a Lorentz line shape.

$$\phi_L(\nu) = \frac{\gamma_L}{\pi[(\nu-\nu_0)^2 + \gamma_L^2]} \tag{4.12}$$

Where γ_L is the Lorentzian half-width of the broadened line. The width linearly depends on the collision frequency with other molecules; hence it is proportional to the mean velocity of the molecules and inverse proportional to the mean free path. Theoretically, pressure broadening is thus proportional to pressure and inversely proportional to the square root of the temperature.

Assuming that both broadening processes are independent of each other, the resulting combined line shape is a convolution of a Gaussian and a Lorentzian line shape, called a Voigt profile (Goody and Yung, 1989; Thomas and Stamnes, 1999):

$$\phi(a,b) = \frac{b}{\pi^{3/2}\gamma D}\int_{-\infty}^{\infty}\frac{\exp(-t^2)}{(a-t)^2+b^2}dt \qquad 4.13$$

With b denoting the ratio of the Lorentzian and the Gaussian half width γ_L/γ_D and a distance from the line center in units of the Gaussian half width ($a=(\nu-\nu_0)/\gamma_D$). The Lorentzian half width γ_L is directly proportional to the pressure p while γ_D is independent of p.

Due to the temperature and pressure dependence caused by the broadening pressure mentioned above, a single cross section can not be used as reference for the entire atmosphere. Besides, the absorption lines of simultaneously retrieved species such as CO, CH_4, and H_2O in the near-infrared range are strong and narrow so that they can not be fully resolved by SCIAMACHY which has only moderate spectral resolution. This leads to a nonlinear relationship between the absorption cross sections and the total optical depth. To account for these circumstances, where classical DOAS is no longer appropriate any more, in this thesis the so called iterative maximum a posteriori-DOAS (IMAP-DOAS) (Frankenberg *et al.*, 2005a) is applied which will be introduced in the next section.

4.3 Iterative Maximum a Posteriori-DOAS (IMAP-DOAS)

The classical DOAS (Platt and Wiley, 1994) uses the Lambert-Bee law to obtain a linear system of equations where the column density to be retrieved is directly proportional to the measured differential optical density:

$$I(\nu) = I_0(\nu)\exp(-\int\sigma(\nu,p,T)c(s)ds) \approx I_0(\nu)\exp(-\sigma(\nu,p,T)\int c(s)ds) \qquad 4.14$$

In the near infrared, considering the temperature and pressure dependence of absorption lines, the integral in equation 4.14 can not be simplified since $\sigma(\nu, p, T)$ is not constant along the light path ds. To solve this problem, the basic idea of IMAP-DOAS is to fit optical depths instead of cross sections. The total vertical optical depths of the respective absorbers are calculated as the sum of the vertical optical densities of sub layers, each having nearly constant pressure and temperature (4.15).

$$OD = \ln\left(\frac{I_0(\nu)}{I(\nu)}\right) = A \cdot \sum_i \sigma_i(\nu, p, T) c_i(s) \qquad 4.15$$

Where A is the airmass factor, which is the ratio of the slant column density and the vertical column density and depends on many factors such as measurement geometry, albedo, wavelength and concentration profile. Neglecting scattering, the airmass factor can be approximated by simple geometric considerations of the slant light path. If clouds are absent, this is a reasonable approximation in the near infrared and assumed in this study. The detailed description of the air mass factor and the correction for the cloud effect is presented in chapter 5.

Strictly speaking, the Lambert-Beer law is only valid for monochromatic light, when spectrometers can fully resolve individual absorption lines. However, in our case, the spectrometer detects light convolved with an instrumental function that is broader than the individual absorption lines. Thus, the spectrometer always records a blend of different wavelengths with very different transmissions. For so-called weak absorbers, the Lambert-Beer law is still valid, but for strong absorbers the problem becomes nonlinear (Frankenberg *et al.*, 2005a), if the width of the high-frequency absorption lines is not fully resolved by the spectrometer. It means, the interchanging of convolution and exponentiation which is often used as a reasonable approximation for weak absorbers in the standard DOAS approach, is inappropriate for strong absorbers:

$$\left\langle I_0 \exp(-\tau_{tot}) \right\rangle \neq I_0 \exp(\left\langle -\tau_{tot} \right\rangle) \qquad 4.16$$

Where I_0 is the Fraunhofer spectrum and< > denotes the convolution with the normalized instrument function

CO is a relatively weak absorber in the near infrared spectral region, but its absorption lines overlap with strong absorption features of CH_4 and H_2O. In order to detect CO, it is

indispensable to account for the absorption of CH_4 and H_2O properly. The idealized radiation seen by the detector is

$$\left\langle I_0 \exp((-\tau_{CH_4} - \tau_{H_2O} - \tau_{CO} - \sum_j b_j)) \right\rangle \quad 4.17$$

b_j is the low frequency polynomial associated with Raleigh, Mie and other broadband extinction processes. The convolution does not strongly affect the low frequency structures, thus

$$\left\langle I_0 \exp((-\tau_{CH_4} - \tau_{H_2O} - \tau_{CO} - \sum_j b_j)) \right\rangle \approx I_0 \exp(-\sum_j b_j) \left\langle \exp(-\tau_{CH_4} - \tau_{H_2O} - \tau_{CO}) \right\rangle \quad 4.18$$

In this case of two strong overlapping absorbers, the absorptions of methane and water can not be considered individually since they affect each other.

$$\left\langle \exp(-\tau_{CH_4} - \tau_{H_2O}) \right\rangle \neq -\left\langle \exp(\tau_{CH_4}) \right\rangle - \left\langle \exp(\tau_{H_2O}) \right\rangle \quad 4.19$$

(Frankenberg *et al.*, 2005a) demonstrate that the error resulting from assuming that equation 4.3.5 holds is far larger than the CO absorptions and can not be neglected.

$$\Delta\tau = -\ln(\left\langle \exp(-\tau_{CH_4} - \tau_{H_2O}) \right\rangle) - (-\ln(\left\langle \exp(-\tau_{CH_4}) \right\rangle) - \ln(\left\langle \exp(-\tau_{H_2O}) \right\rangle)) \quad 4.20$$

$$\Delta\tau >> -\ln(\left\langle \exp(-\tau_{CO}) \right\rangle) \quad 4.21$$

This problem is solved by taking $-\ln(\left\langle \exp(-\tau_{CH_4} - \tau_{H_2O} - \tau_{CO}) \right\rangle)$ as a linearization point in IMAP-DOAS.

Based on optimal estimation theory introduced to the remote sensing community by (Rodgers, 1976), IMAP-DOAS iterates the vertical column densities (slant column densities divided by the air mass factor) of the absorbers of interest (in this case, CH_4, H_2O and CO), until the modeled total optical density fits the measurement.

The general concept is a linearization of the forward model F(x) at x_0 (nomenclature according to (Rodgers, 2000)):

$$y = F(x_0) + \left.\frac{\partial F(x)}{\partial x}\right|_{X_0} \cdot (x - x_0) + \varepsilon \quad 4.22$$

Where y denotes the measurement $\ln(I/I_0)$ and $F(x_0)$ the theoretical value of $\ln(I/I_0)$ evaluated at a state vector x_0 by means of a radiative transfer model (in the non-scattering case simply the Beer-Lambert law). The state vector is comprised of the scaling factors for the vertical columns

of the respective trace gases in different height layers, a climatological index for temperature change in the atmosphere, and polynomial coefficients accounting for low frequency absorptions and scattering. The derivatives $K_0 = \left.\frac{\partial F(x)}{\partial x}\right|_{x_0}$ can be represented as a Jacobian Matrix where each column is the derivative vector of the measurement with respect to an element of the state vector.

Assuming the elements of the state vector to have Gaussian distributions, the state vector maximizing the a posteriori probability density function of a nonlinear problem can then be written by means of Newtonian iteration (Rodgers, 2000). Each iteration of the Gauss-Newton method requires the following operations:

$$x_{i+1} = x_a + (K_i^T S_\varepsilon^{-1} K_i + S_a^{-1})^{-1} K_i^T S_\varepsilon^{-1} [y - F(x_i) + K_i(x_i - x_a)] \quad 4.23$$

where

x_a = *a priori* state vector,

x_i = state vector at the i-th iteration,

S_ε = (pixel) error covariance matrix,

S_a = *a priori* covariance matrix,

$F(x_i)$ = forward model evaluated at x_i,

K_i = Jacobian of the forward model at x_i.

To solve equation 4.23 by the least squares method, it is written in the form:

$$(K_i^T S_\varepsilon^{-1} K_i + S_a^{-1})^{-1} (x_{i+1} - x_a) = K_i^T S_\varepsilon^{-1} \delta y_i \quad 4.24$$

or

$$\begin{pmatrix} S_\varepsilon^{-1/2} K_i \\ S_a^{-1/2} \end{pmatrix} (x_{i+1} - x_a) = \begin{pmatrix} S_\varepsilon^{-1/2} \delta y_i \\ 0 \end{pmatrix} \quad 4.25$$

where $\delta y_i = y - F(x_i) + K_i(x_i - x_a)$

At last the slant column density is calculated by scaling the first assumed total column density with the retrieved x_i. Thus, given a linearization point, the derivatives of the measured optical density and other affecting factors can be calculated. A detailed description of IMAP-DOAS fitting routine is given by Frankenberg *et al.* (2005a). One example of the fitting results is shown

in Figure 4.1. Due to the decline of instrument sensitivity towards larger wavelengths, for the retrieval of CO, a fit window between 2324nm and 2335nm was chosen which is an optimal fitting window with respect to signal to noise ratio.

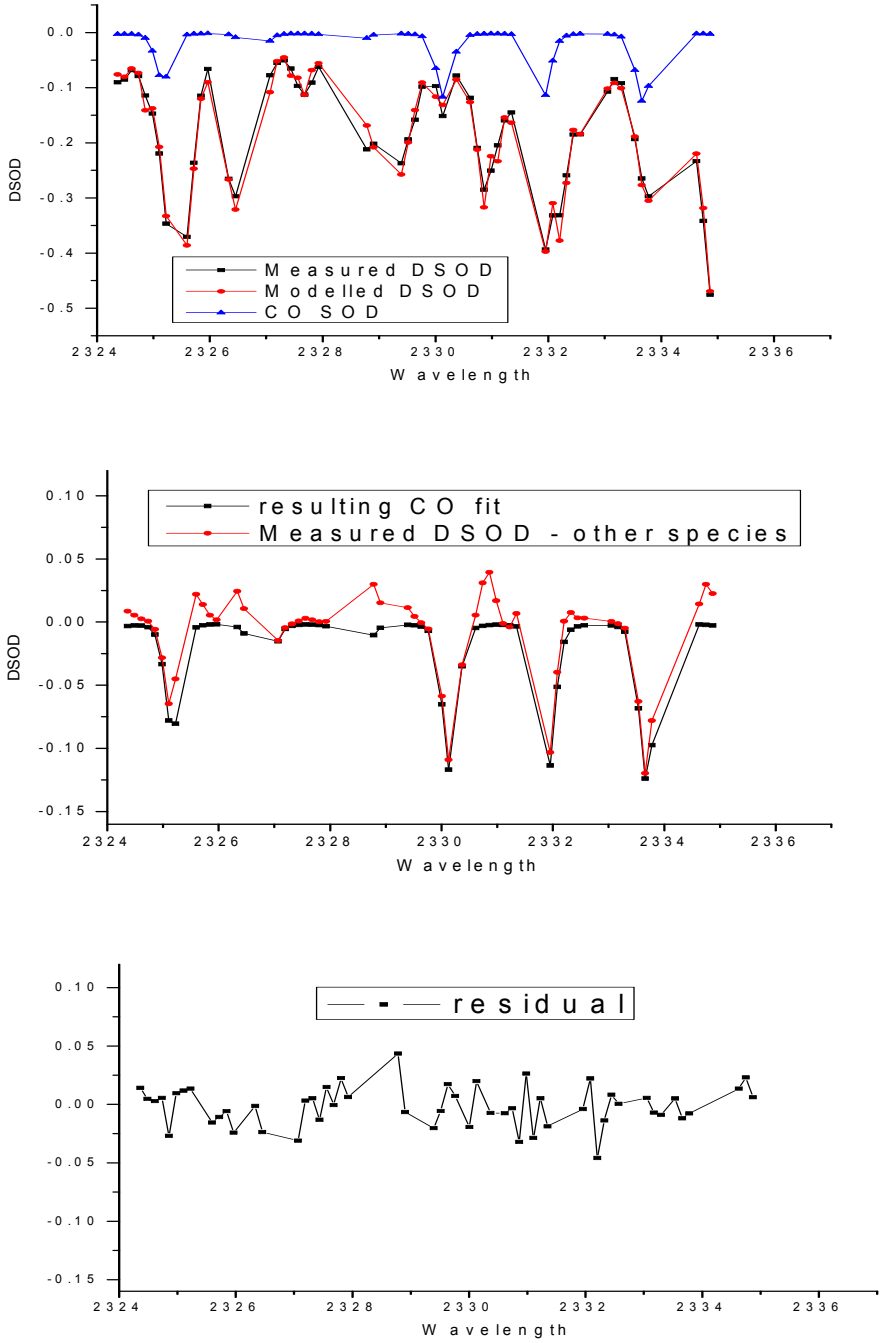

Figure 4.1: Example of a CO fit with relatively strong CO absorptions (V CD $\approx 8.5 \cdot 10^{18}$ molec/cm^2). The upper panel shows the differential slant optical density (DSOD) of all absorbers (CH_4, H_2O and CO) as well as that of CO separated (blue line). The centre panel shows the measured slant optical density with the slant optical density of CH_4 and H_2O subtracted in order to depict only the absorption structures of CO. The lower panel shows the residual of the fit.

4.4 Sensitivity Study of the Shielding Effect of Clouds

As mentioned above, due to the strong temperature and pressure dependence of the cross sections of the trace gases under study in the near infrared, the basic idea of IMAP-DOAS is to fit optical depths instead of cross sections. Also, to account for the strong absorption and the varying vertical profile of the absorber amount, the atmosphere is sub-divided into three layers in IMAP-DOAS. The optical depth of each layer is obtained by integrating the altitude-dependent cross sections (each having nearly constant pressure and temperature), multiplied by an *a priori* absorber profile (US standard profile) throughout the corresponding layer. This is schematically shown in Figure 4.2.

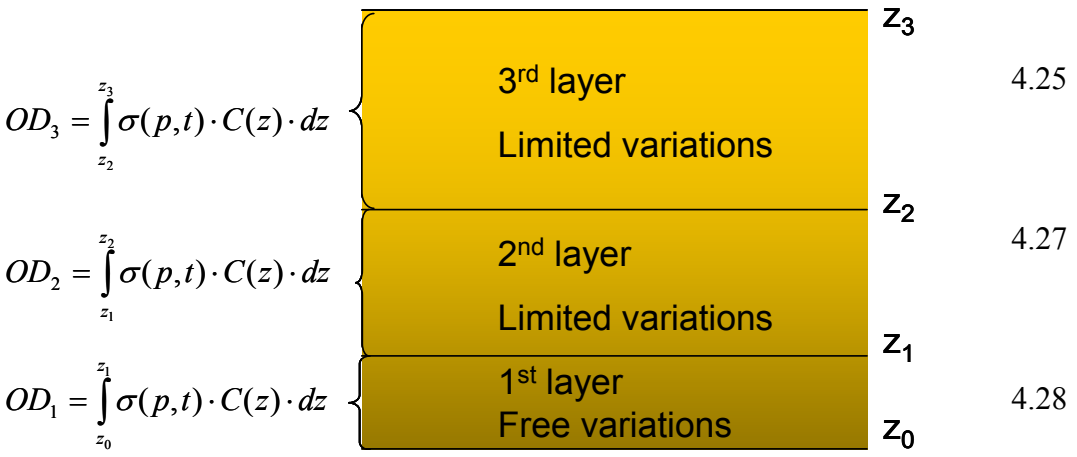

Figure 4.2: The first assumption of trace gases optical depth in the atmosphere in IMAP-DOAS simulations.

In the first (lowest) layer, usually up to 3 km altitude, the CO number density and vertical profile are highly variable. The steepest gradients are found here because nearly all emissions originate from (near) the surface. The second layer lies between 3 and 12 km, and is much less variable. This is where most large-scale transport of trace gases occurs. The third (upper) layer, from 12 km to top of atmosphere, is the least variable in trace gas concentration.

Since our instrument has only moderate spectral resolution, the retrieved optical depths at different height layers for the same species are nearly linearly dependent. However, the information content of the measurement is not high enough to discriminate between different height layers. In order to be more sensitive to changes in the lower atmosphere where the

variance of CO concentration is expected to be high, only small variances for the OD of higher atmosphere layers are allowed.

One fundamental problem appears if clouds shield a major fraction of the lower atmosphere. Especially if clouds are higher than the height of the 1st layer (3km), the retrieval of trace gas amounts becomes problematic. This can be easily seen in Figure 4.2: if a satellite pixel is completely covered by a cloud, which is located at or below z_1 (the top of layer 1), the OD_1 is adjusted by the algorithm to fit the observation; OD_2 and OD_3 are unaffected. If the cloud is located between z_1 and z_2, the retrieved OD_1 should be zero and the OD_2 should be smaller than *a priori* OD of the 2nd layer. But because only small variances of OD_2 are allowed in the retrieval algorithm, OD_1 is set to a negative value to compensate when the shielding effect of the cloud is larger than the allowed variance of OD_2.

The potential errors caused by this effect are investigated in two ways. The first is to allow more variability in the optical depth in the second layer (i.e., OD_2).

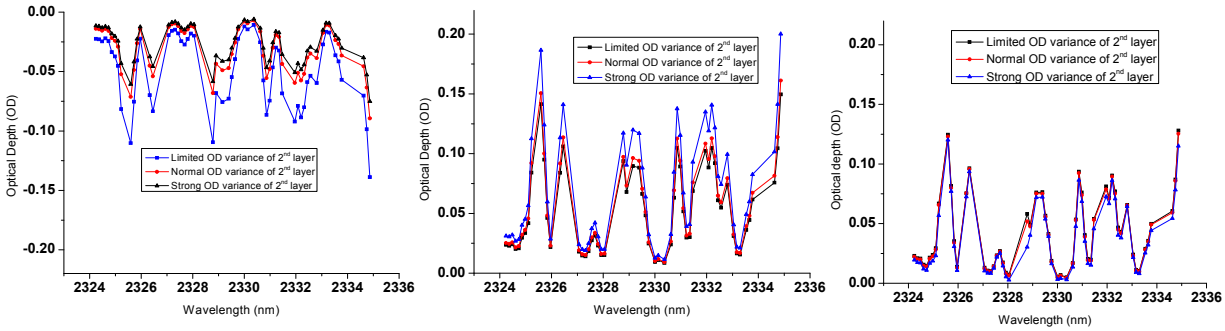

(a) CH_4 optical depth of 1st layer (b) CH_4 optical depth of 2nd layer (c) CH_4 total optical depth

Figure 4.3: Comparison of the CH_4 fit with different limits for the variance for the 2nd layer, which is synchronously retrieved with CO for a measurement with completely cloud-covered ground pixel. (a) The optical depth of the 1st layer. (b) The optical depth of the 2nd layer. (c) The total optical depth.

Considering that CH_4 is a strong absorber in the fitting range of CO, the optical depth (OD) from the CH_4 fit with different variance settings for the 2nd layer are compared, leaving the variability in the first layer unchanged. In Figure 4.3 the results are shown for three cases: 1) variance of CH_4 OD in the 1st layer, limited OD variance in the 2nd layer (default case; black lines); 2) same variability of CH_4 OD for 1st and 2nd layer (red line); 3) no limitation of CH_4 OD for 2nd layer (blue line).

The left panel (a) shows the retrieved CH_4 optical depths in the first layer (OD_1); the middle panel (b) shows OD_2, the optical depth in the second layer, and the right panel (c) contains the total column CH_4 OD (sum of OD_1, OD_2, and OD_3).

In Figure 4.3 it can be seen that allowing more freedom in the second layer improves the OD in the first layer slightly (the red and blue lines in panel are closer to zero). However, the total OD (panel c) does not change significantly. Apparently, this method is not very sensitive to the effect of clouds.

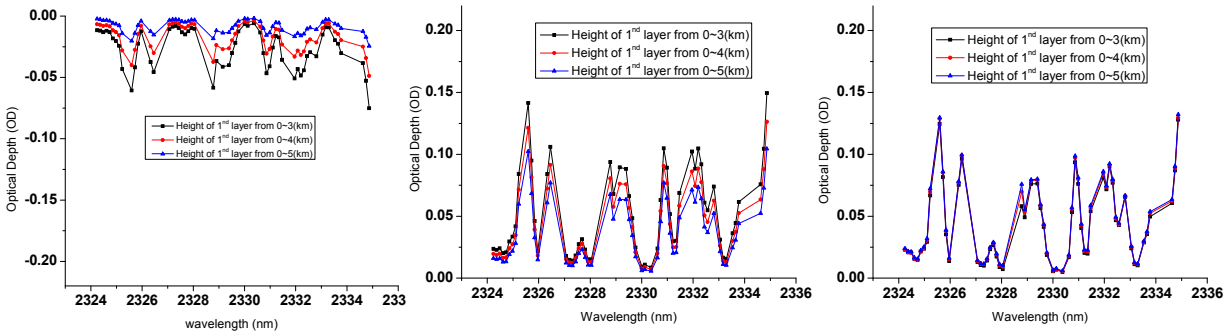

(a) CH_4 optical depth of 1st layer (b) CH_4 optical depth of 2nd layer (c) CH_4 total optical depth

Figure 4.4: Comparison of the CH_4 fit with different height settings of the 1st layer for a completely cloud-covered ground pixel. (a) The optical depth of the 1st layer. (a) The optical depth of the 2nd layer. (c) The total optical depth.

The other method is to divide the atmosphere according to the cloud top height information from the individual satellite observations (FRESCO+, Wang *et al.*, 2008). Figure 4.4 shows the comparison of the CH_4 fit with different settings for the altitude of the 1st layer height: 0~3km (default setting; black line), 0~4km (red line) and 0~5km (blue line). The variability of the second layer was set to the default value. Since the cloud top height of this pixel is 5km, it is reasonable that when the height of the 1st layer increases, the retrieved optical depth of the 1st layer becomes less negative, and the optical depth of the 2nd layer decreases. However, even when the height of the 1st layer is the same as the actual cloud top height (here 5 km), the retrieved optical depth in the 1st layer is still less than 0. One possible reason could be that the cloud top height used for atmospheric separation is underestimated by FRESCO+ or even the cloud still can not completely shield the CO below the cloud, e.g., due to the effect of convective uplifting.

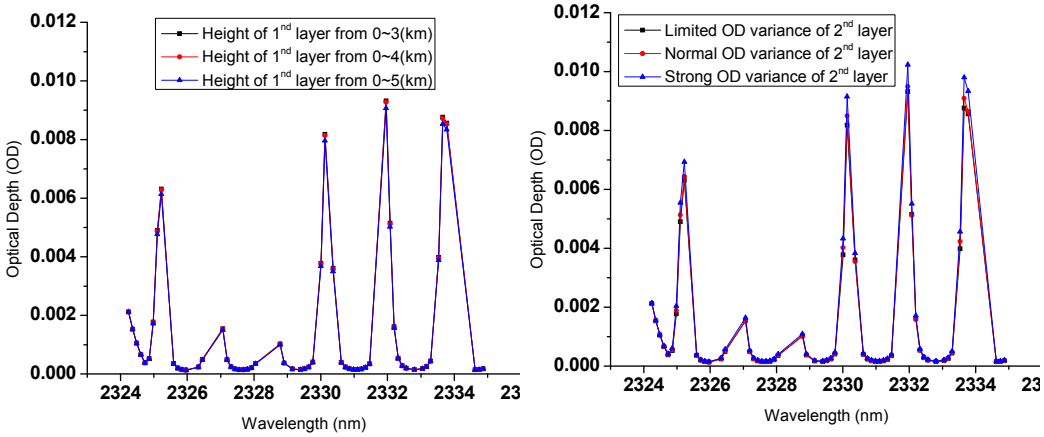

(a) CO optical depth with different limitation of the variance for 2nd layer

(b) CO optical depth with different height setting of 1st layer

Figure 4.5: Comparison of the CO fit with different limits for the variance of the 2nd layer and different height setting of the 1st layer. (a) The CO optical depth with different limits for the variance for the 2nd layer. (b) The CO optical depth with different height setting of the 1st layer.

In summary, it is found that both methods are rather insensitive to the influence of cloud shielding. This is a very important finding, because otherwise the uncertainties of the CO retrieval in the presence of clouds would have been largely increased. Because the difference in the retrieved CO (Figure 4.5) total optical depth between different tested parameter settings is very small, in this thesis the original atmospheric separation (with z_1 = 3 km) keep using, and only small variances for the scaling factors of the higher layers are allowed.

5 Radiation Transfer Model

5.1 Definition of Air Mass Factor and Box Air Mass Factor

The direct result of the spectral analysis is typically the so called Slant Column Density (SCD). This quantity represents the concentration of the specified trace gas integrated over all possible photon paths. Therefore, the SCD is a function of the solar zenith angle (SZA) and other parameters like cloud fraction and ground albedo. In order to become independent of viewing geometry the slant column density is usually transformed into the so called Vertical Column Density (VCD), which represents the concentration integrated along a vertical column through the atmosphere. For this transformation the concept of Air Mass Factors AMF (see e.g., Perliski and Solomon, 1993), has proved to be very useful. The AMF is defined as the ratio of the SCD and the VCD:

$$\text{AMF= SCD/AMF} \qquad 5.1$$

thus

$$\text{VCD=SCD/AMF} \qquad 5.2$$

Since Rayleigh scattering in the near IR spectral range can be neglected, in the absence of clouds, the observed light is simply reflected at the ground, and the AMF cam be well described by simple geometry. The so called “geometric AMF” (for nadir geometry) is:

$$AMF_{geom} = \frac{1}{\cos(LOS)} + \frac{1}{\cos(SZA)} \qquad 5.3$$

with LOS the viewing angle with respect to the nadir and SZA the solar zenith angle.

Here it should be noted that in the original IMAP-algorithm (Frankenberg *et al.*, 2005a) a geometric AMF is included in the spectral retrieval. Thus IMAP retrieval directly yields the CO VCD. The CO SCD can be simply calculated by multiplying the retrieved CO VCD by the geometric AMF (equation 5.3).

To describe the sensitivity of the measurements on the vertical distribution, the Box Air Mass Factor was introduced (equation 5.4). The Box-AMF represents the contribution of a trace gas located at a certain altitude interval, or vertical ‘box’, to the overall AMF under the given

atmospheric conditions. It is thus a measure of the sensitivity of a particular viewing direction towards an absorber being present in a specific altitude. In addition, the Box-AMF characterizes the ratio of the partial SCD to the partial VCD of an atmospheric layer with an assumed constant trace gas concentration. The relationship between total AMF and Box-AMF is shown in equation 5.5.

$$\text{Box-AMF}(z_i) = \text{SCD}(z_i) / \text{VCD}(z_i) \qquad 5.4$$

with $\text{SCD}(z_i)$ and $\text{VCD}(z_i)$ the partial slant and vertical column densities of layer i.

$$AMF = \frac{\sum_{0}^{TOA} AMF_i \cdot VCD_i}{\sum_{0}^{TOA} VCD_i} \qquad 5.5$$

AMF_i and VCD_i refer to the Box-AMF and the partial VCD for layer i; within the layer the trace gas concentration is assumed to be constant.

Both AMF and Box-AMF can be calculated with radiative transfer models (RTMs). In this thesis the full spherical Monte-Carlo atmospheric radiative transfer model McArtim (Monte Carlo Atmospheric Radiative Transfer and Inversion Model) (Deutschmann *et al.*, 2010; Deutschmann, 2008) is used; it was compared to various other radiative transfer models (Wagner *et al.*, 2007) and excellent agreement was found. McArtim allows the simulation of ensembles of individual photon trajectories for a given atmospheric situation. From these trajectories the average frequency of the modeled photons for certain interactions with atmospheric constituents or with the Earth's surface are determined. The scattering events are modeled individually, according to their respective scattering cross sections and phase functions. Interaction with the Earth's surface is treated as a Lambertian reflection.

5.2 Sensitivity Study of Cloud Effect

In the near-infrared fitting range of CO (2324nm to 2335nm), due to the longer wavelength, Rayleigh scattering can be neglected. Thus, the geometric air mass factor (AMF) could be a good approximation in the absence of clouds, which is demonstrated in Figure 5.1. Figure 5.1 shows the Box-AMF factor simulated by the radiative transfer model McArtim for different solar zenith

angles and ground albedo scenarios in the absence of clouds. It is found that the geometric AMF matches quite well the simulated Box-AMF. Although, the simulated Box-AMF deviates from the geometric AMF at higher altitudes for larger solar zenith angles, many measurements with large SZA are discarded due to very low SNR in the fitting procedure. Besides this, it could be found that the sensitivity of the measurements on altitude does not depend on the ground albedo for clear sky. This demonstrates that in the near-infrared, the geometric AMF is a very suitable global approximation for the conversion of SCDs to VCDs for cloud free cases.

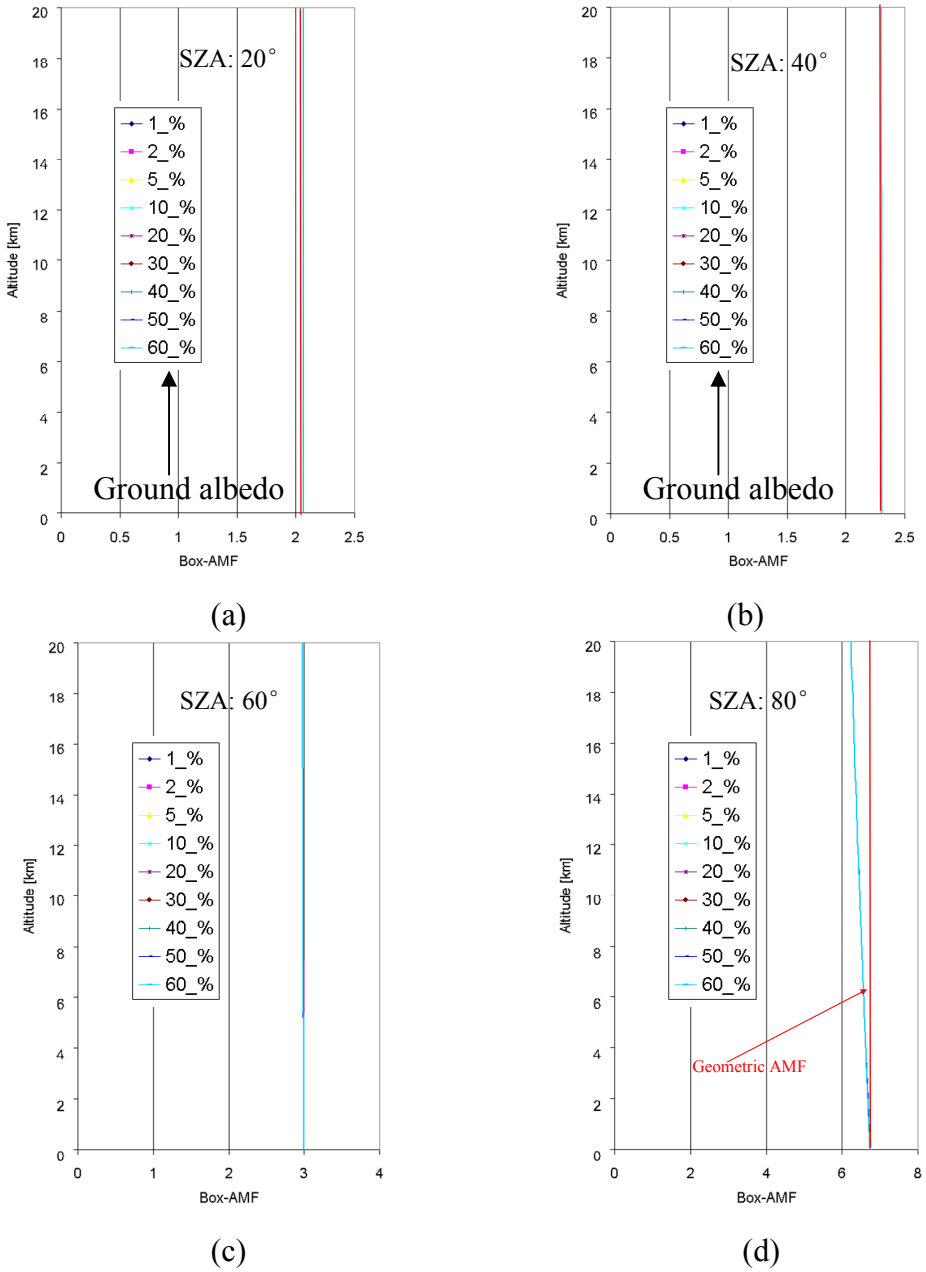

Figure 5.1: Box-AMF factor simulated by the radiative transfer model McArtim for different solar zenith angle and ground albedo scenarios in the absence of clouds. The red line in each figure denotes the geometric AMF.

When clouds are present, as in the left side of Figure 5.2, the measurement sensitivity is enhanced at the cloud top due to multiple scattering, and this enhancement increases with decreasing SZA. Besides this, it is found that the measurement sensitivity is strongly reduced below the clouds which are the well known cloud shielding effect. Because of the high cloud top albedo even for small cloud fractions most of the photons that the satellite receives are reflected from the cloud top. For example, in the case of a cloud fraction of 20% (the general threshold of cloud free cases), cloud albedo of 80% and ground albedo of 5%, the majority (80%) of all measured photons are reflected at the cloud top. This example indicates that without a proper cloud correction procedure, the CO columns are strongly and systematically underestimated, especially over biomass burning and industrial regions. Therefore a cloud correction procedure is developed (and applied) which is described in the next section.

There is one important aspect which needs to be mentioned here: in this thesis, a rather simple cloud model is used. In contrast to the Radiative transfer results shown above, a so called Lambertian cloud model is used in this study, which assumes that clouds are simple reflecting surfaces (with a specified albedo), which completely shield the atmosphere below. The reason for this is that the cloud information used for our cloud correction scheme is from the FRESCO+ algorithm (Wang *et al.*, 2008), which calculates cloud information (effective cloud top height, effective cloud fraction etc.) also based on the assumption of a Lambertian cloud.

The measurement sensitivity as a function of the cloud altitude for the assumption of a Lambertian cloud is shown in the right side of Figure 5.2: The difference of the measurement sensitivity between these two types of cloud models becomes smaller when the solar zenith angle is high.

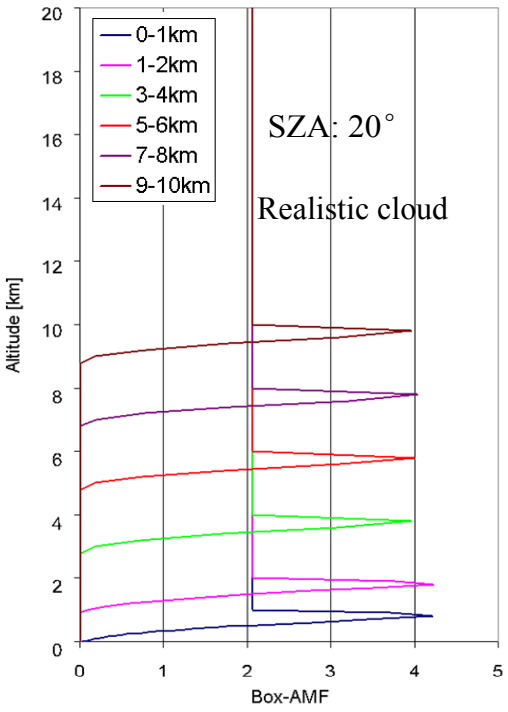
0-1km
1-2km
3-4km
5-6km
7-8km
9-10km
SZA: 20°
Realistic cloud
Altitude [km]
Box-AMF

(a)

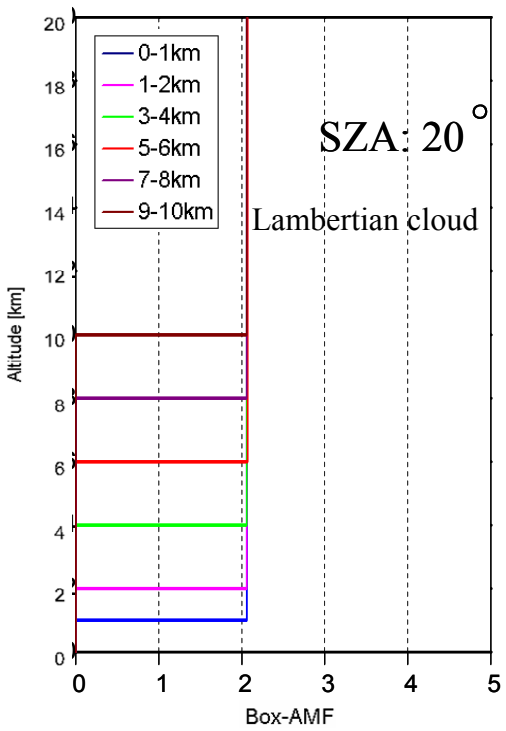
0-1km
1-2km
3-4km
5-6km
7-8km
9-10km
SZA: 20°
Lambertian cloud
Altitude [km]
Box-AMF

(b)

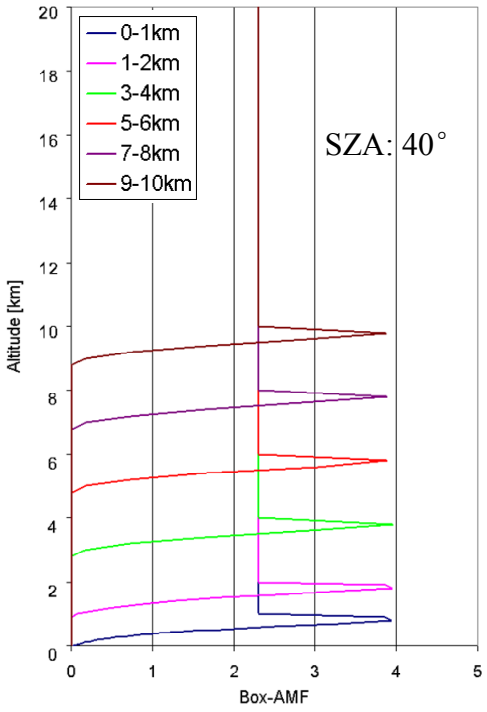
0-1km
1-2km
3-4km
5-6km
7-8km
9-10km
SZA: 40°
Altitude [km]
Box-AMF

(c)

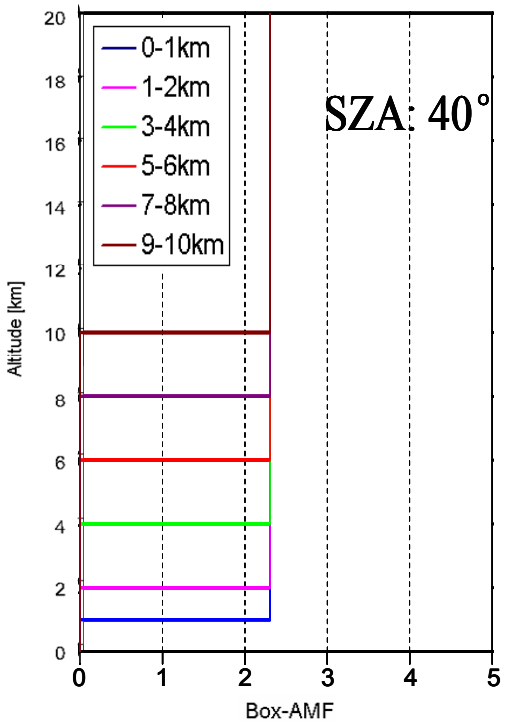
0-1km
1-2km
3-4km
5-6km
7-8km
9-10km
SZA: 40°
Altitude [km]
Box-AMF

(d)

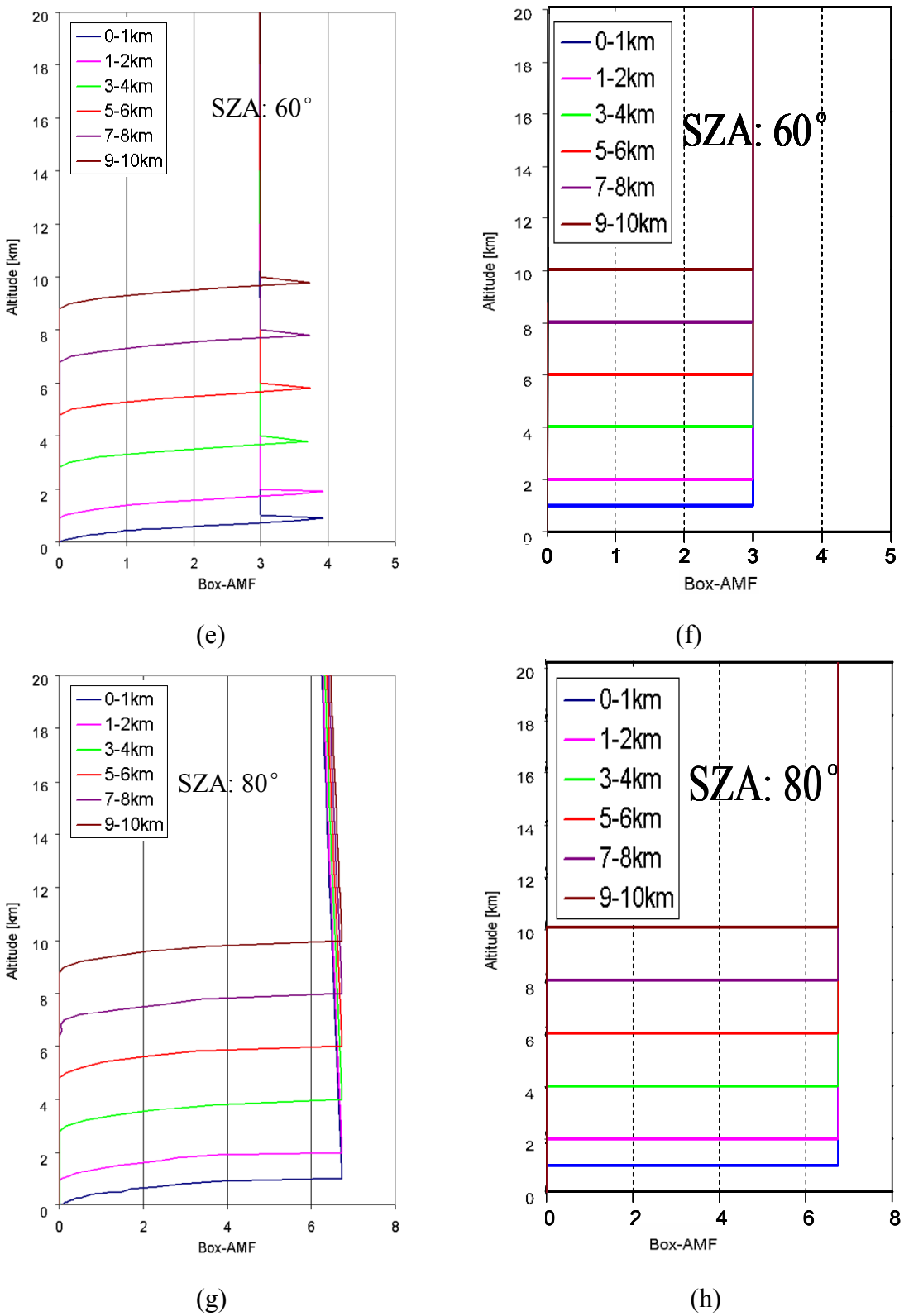

Figure 5.2: Box-AMF simulated by the radiative transfer model McArtim for different solar zenith angles and different heights of the clouds (ground albedo is 5%). The left side is for a 'realistic cloud'; The right side is for a Lambertian cloud, which is also the assumption of FRESCO+.

5.3 Correction for the Cloud Shielding Effect

From the sensitivity study of the cloud effect above, it follows that even for small cloud fractions, the clouds can still strongly affect the retrieved CO VCD, especially if the cloud altitude is high, the surface albedo is low, and the surface-near CO concentration is high.

Thus an appropriate cloud correction is particularly important for measurements close to strong emission sources. In this thesis, before the normalized SCIAMACHY data set can be used for comparison with other data sets like e.g., ground based observations or model results, the effect of clouds on the measurement sensitivity has to be corrected. Here it should be noted that – to our knowledge – such a cloud correction was not applied to any SCIAMACHY CO data before. Cloud effects can be minimized by excluding measurements with large effective cloud fractions; for satellite observations of tropospheric trace gases often a threshold of 20% to 30% effective cloud fraction is used. In this study only measurements with effective cloud fractions <20% are considered. But even for such small cloud fractions the errors can be up to 100%.

In this cloud correction, the effective cloud fraction and effective cloud top height are used; these cloud properties are simultaneously retrieved by the FRESCO+ algorithm (Wang *et al.*, 2008); the influence of the surface albedo is taken into account using MODIS albedo maps for the wavelength range of our CO retrieval (Justice *et al.*, 1998). The independent pixel approximation is used: the CO absorptions of the clear and cloudy parts of a satellite pixel are weighted, according to the effective cloud fraction and the respective radiances of the cloudy and clear fractions. For the cloudy part of the pixel it is assumed that the sensitivity to CO above the cloud is high, but is zero below the cloud top (see Figure 5.2). This assumption is justified by the high effective albedo of clouds. For the clear part of the pixel it is assumed that a constant sensitivity throughout the atmosphere, which is justified by the low probability of Rayleigh-scattering in the near IR spectral range. As already mention in the above section, in this thesis, the description of clouds by a so called Lambertian reflector is chosen, because such a cloud model is also used in the FRESCO algorithm.

First, box-AMFs (equation 5.4) for different layer heights are calculated:

$$Box_{AMF}(z_i) = \frac{(1-CF)\cdot SA\cdot AMF_{Clear} + CF\cdot CA\cdot AMF_{Cloud}}{(1-CF)\cdot SA + CF\cdot CA} \quad 5.5$$

Here z_i indicates the height of the atmospheric layer CF, indicates the (effective) cloud fraction, SA indicates the surface albedo, and CA indicates the cloud top albedo. AMF_{clear} is approximated by the geometrical AMF assumption (equation 5.3). AMF_{cloud} is zero for $z_i <$ the cloud top height and set to the geometric AMF for $z_i \geq$ the cloud top height.

These box-AMFs describe the height resolved sensitivity of the SCIAMACHY observation the depending on the actual effective cloud fraction, cloud top height, and ground albedo. If the (relative) CO profile for the observed atmospheric scene is known (or assumed), the total cloud-corrected CO VCD can then be calculated from the SCIAMACHY observation based on the height dependent sensitivity.

$$VCD_{SCIA,corrected} = \frac{VCD_{SCIA}\cdot AMF_{geo}}{AMF_{total,profile}} \quad 5.6$$

with

$$AMF_{total,profile} = \frac{\sum_z BOX_{AMF}(z_i)\cdot c_{CO,profile}(z_i)}{\sum_z c_{CO,profile}(z_i)} \quad 5.7$$

VCD_{SCIA} indicates the IMAP CO VCD after the normalization procedure, see section chapter 7; $c_{CO,\,profile}(z_i)$ indicates the CO concentration at layer i.

Using the formalism of (Eskes and Boersma, 2003), besides the cloud-corrected CO VCDs, also averaging kernels can be calculated for individual SCIAMACHY CO observations.

$$AK(z_i) = \frac{BOX_{AMF}(z_i)}{AMF_{total,profile}} \quad 5.8$$

If no independent information on the CO profile (e.g., from model simulations) is available, a

'standard CO profile' for the retrieval of CO VCDs from SCIAMACHY observations is used. This 'standard profile' is constructed as a compromise between CO profiles from chemical models for polluted and remote areas; it is shown in Figure 5.3. Using this profile as input in equation 5.7, the new standard SCIAMACHY CO VCD is determined:

$$VCD_{SCIA,standard} = \frac{VCD_{SCIA} \cdot AMF_{geo}}{AMF_{total,standard}} \qquad 5.9$$

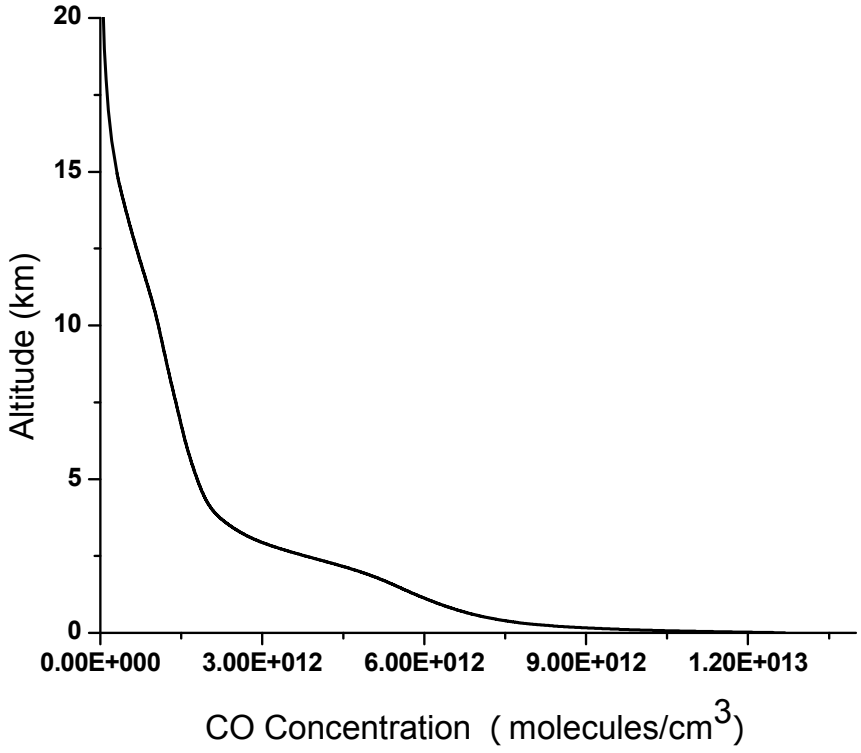

Figure 5.3: Standard CO profile used for the calculation of the SCIAMACHY vertical CO column density.

Of course, this choice of a CO profile is somewhat arbitrary and can lead to large deviations of the retrieved CO VCDs from the true atmospheric CO VCDs, depending on the true atmospheric CO profile. Close to emission sources, where the CO concentration in the surface-near layers might be higher than in the standard profile, the retrieved SCIAMACHY CO VCD tends to underestimate the true CO VCD. In contrast, for remote unpolluted regions, the actual surface-near CO concentration might be lower than assumed by the standard profile, and thus the

retrieved SCIAMACHY CO VCD tends to overestimate the true CO VCD. These dependencies should be kept in mind when the values of our SCIAMACHY standard CO VCD are compared to other data sets of CO VCDs. However, if the SCIAMACHY CO VCD is compared to a data set which provides explicit profile information (e.g., from climate chemistry models), the application of the averaging kernels properly takes into account the height-dependent sensitivity of the SCIAMACHY observation; or in other words: if both measurements and model simulations are correct, exact agreement between both data sets must be expected by considering the averaging kernels of the measurements. A detailed comparison between satellite measurements and climate chemistry models is shown in chapter 9.

In Figure 5.4, examples for the averaging kernels of SCIAMACHY CO observations (for effective cloud fractions <20%) are shown. The graphs present the monthly mean averaging kernels for SCIAMACHY and MOPITT observations over selected regions (central Africa, January 2004, and east of China, May 2004). It is obvious that – as expected – SCIAMACHY is much more sensitive to surface near CO concentrations than MOPITT. Nevertheless, due to the cloud shielding effect, also the sensitivity of SCIAMACHY CO observations systematically decreases towards the ground (by about 20% for observations with cloud fractions <20%), but this decrease of sensitivity is considered for the quantitative comparisons with model data in this study (see chapter 9).

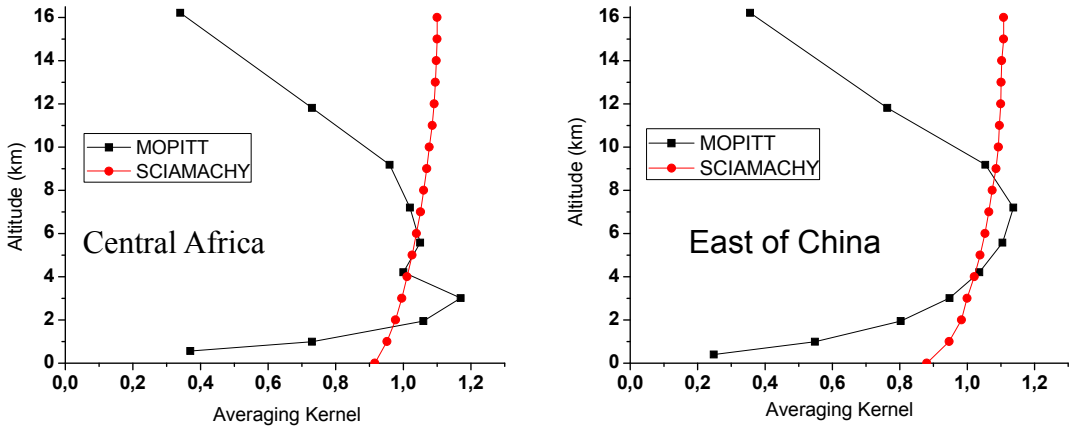

Figure 5.4: Examples of MOPITT's and SCIAMACHY's monthly mean averaging kernels over central Africa (5°N to 12°N; 15°W to 32°E, January 2004) and East of China. (20°N to 40°N; 107°E to 123°E, May 2004). Only observations with effective cloud fractions <20% are selected.

The importance of a proper cloud correction is illustrated in Figure 5.5, where the relative difference of SCIAMACHY CO VCDs with and without cloud correction is shown. The relative difference is below 20% over desert areas where the surface albedo is high and cloud fraction is low. In general, over areas with small cloud fraction and low cloud top height, relatively small differences are found. However, over areas with high cloud top height the relative difference can reach up to 100%. Here it should be noted that most of these areas (such as industrial regions and biomass burning regions) are of great interest for the verification of current emission estimates.

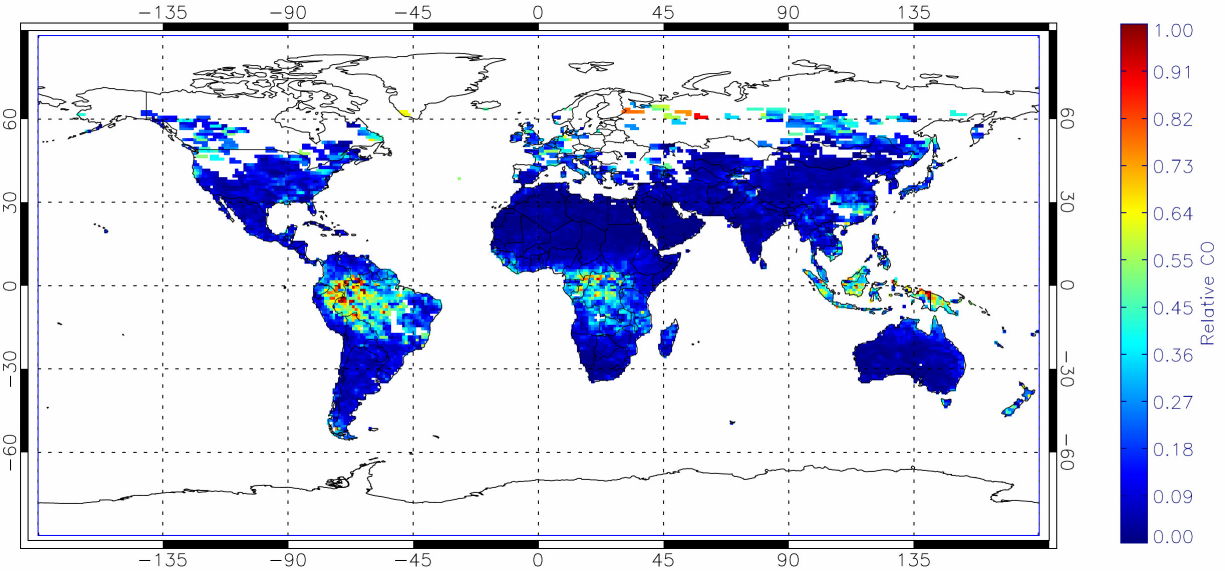

Figure 5.5: Relative difference of SCIAMACHY CO columns with and without cloud correction (January 2004). Only observations with effective cloud fractions <20% are considered.

6 Attempts to Correct the Effects of the Ice Layer on the SCIAMACHY near-IR Detectors and of the Increasing Number of Bad and Dead Detector Pixels

In many studies in recent years, biases of the SCIAMACHY CO VCDs were reported or were obvious in the presented data sets. Typically, they do not only depend on location (e.g., showing a latitudinal gradient) but also vary with time (e.g., Buchwitz *et al.*, 2005; Buchwitz *et al.*, 2007; Turquety *et al.*, 2008; Gloudemans *et al.*, 2009; Kopacz *et al.*, 2010; de Laat *et al.*, 2010). The reasons for these biases are not completely understood, but are probably related to several problems of the SCIAMACHY detectors. For example a changing ice-layer on the SCIAMACHY near-IR detectors influences the measurements in several ways (e.g., Gloudemans *et al.*, 2005) Most importantly, they cause a loss of signal and systematically change the instrument slit function. In addition, the dark current of the detectors is influenced. Variations of the dark current occur also within individual orbits. The SCIAMACHY near-IR detectors also suffer from variable but generally increasing numbers of so called bad and dead pixels, which can not be used for the analysis. For all of these problems possible solutions have been developed and applied in recent years (e.g., Gloudemans *et al.*, 2005; Frankenberg *et al.*, 2005b; Buchwitz *et al.*, 2006a; Buchwitz *et al.*, 2007; Gloudemans *et al.*, 2009). Nevertheless, these corrections are not perfect, and the retrieved CO VCDs are still subject to remaining errors.

In this thesis similar correction procedures are developed and tested as described below. In addition to existing correction methods (like adding a variable bias to the spectral retrieval or normalizing the CO data by simultaneous retrieved CH_4 data), a new correction method using variable slit functions is developed. All three correction methods are described in detail below.

6.1 Application of a Variable Offset in the Spectral Retrieval

One problem caused by the variable ice layer on the SCIAMACHY near-IR detectors is that they cause a change in the instrument slit function (Gloudemans *et al.*, 2005). Especially the wings of the slit function are largely broadened. Effectively, this modification of the instrument function leads to an additional broad band intensity offset in the measured spectra. As suggested by Gloudemans *et al.* (2005), this effect can be corrected for by adding a variable offset in the spectral retrieval. The offset is determined in such a way that the retrieved CH_4 VCD above the Sahara equals the expected value. The relative value of the retrieved offset to the average intensity of the SCIAMACHY spectrum is then used to calculate the respective offsets for all SCIAMACHY observations of that day.

In this thesis a similar correction procedure for our SCIAMACHY CO retrieval is developed. The results are shown in Figure 6.1. The black symbols indicate the VCDs of CH_4 (left) and CO (right) for the original IMAP analysis over the Sahara. The red symbols indicate the respective results after applying the correction using a variable offset. In Blue the corresponding MOPITT results are shown. It is found that for the CH_4 VCD the effect of the changing ice layer can be almost corrected by the method of variable offsets. Also for part of the CO VCDs (in 2003) some improvement can be seen. However, it also turned out that especially after 2005 the increasing difference between the SCIAMACHY results and the MOPITT results are only slightly improved by this correction method. Thus it is conclude that for the IMAP retrieval of CO, this correction method does not lead to a sufficient quality of the retrieved CO VCDs. Here it is interesting to note that the improvement reported by other studies (e.g., Gloudemans *et al.*, 2005) is better than found in our study. The reason for these differences are not clear, but might be caused by the use of different retrieval settings. Nevertheless, also the CO VCDs retrieved by Gloudemans *et al.* (2005; 2009) show still significant systematic biases, which also depend on latitude and time.

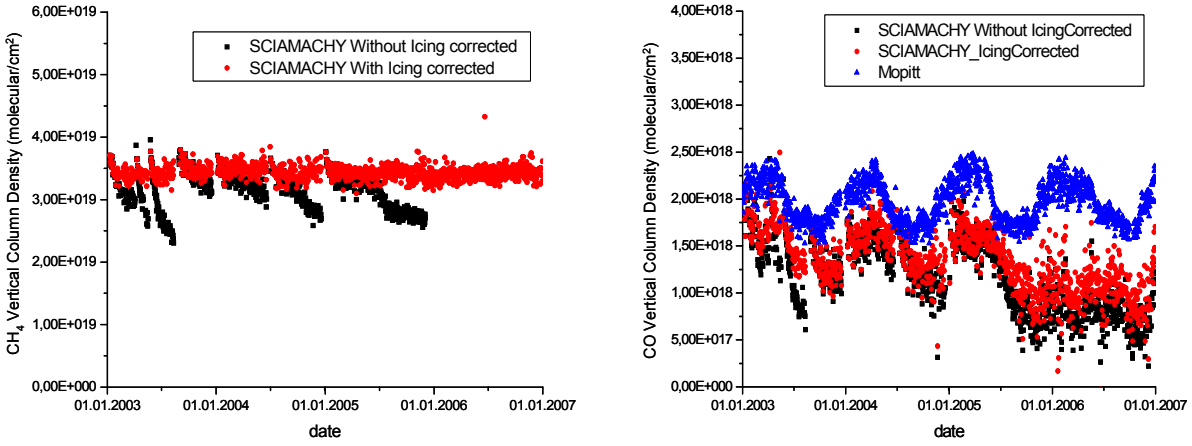

Figure 6.1: Time series of VCDs of CH4 (left) and CO (right) over the Sahara. The black symbols indicate the results of the original IMAP retrieval. The red symbols indicate the respective results after applying the correction using a variable offset. In blue the corresponding MOPITT results are shown.

6.2 Normalization of the CO VCDs Using Simultaneously Retrieved CH_4 VCDs

Buchwitz *et al.* (2006a; 2007) suggested applying a normalization procedure of the analyzed CO VCDs using simultaneously retrieved CH_4 VCDs. The idea behind this approach is that the atmospheric CH_4 VCDs are rather constant. Assuming that the effect of the instrumental problems is similar to the retrieval of the absorptions of CO and CH_4, one can determine the deviation of the retrieved CH_4 VCD from the expected value and then apply the determined correction factor to the retrieved CO VCD. An interesting side effect of this method is that also the effect of clouds is corrected for (at least to some degree). Buchwitz *et al.* (2007) showed that using this method, the effect of the ice layer on the CO VCD can indeed largely be corrected.

In this thesis a similar normalization method is developed and applied to our CO analysis; the results are shown in Figure 6.2. Like for the method of variable offset, some improvement of the CO VCDs can be seen (in 2003), but again, the improvement in general does not lead to a sufficient quality of the retrieved CO VCDs. Here it is interesting to note that also Buchwitz *et al.* (2007) state that the normalization procedure does not correct for all biases.

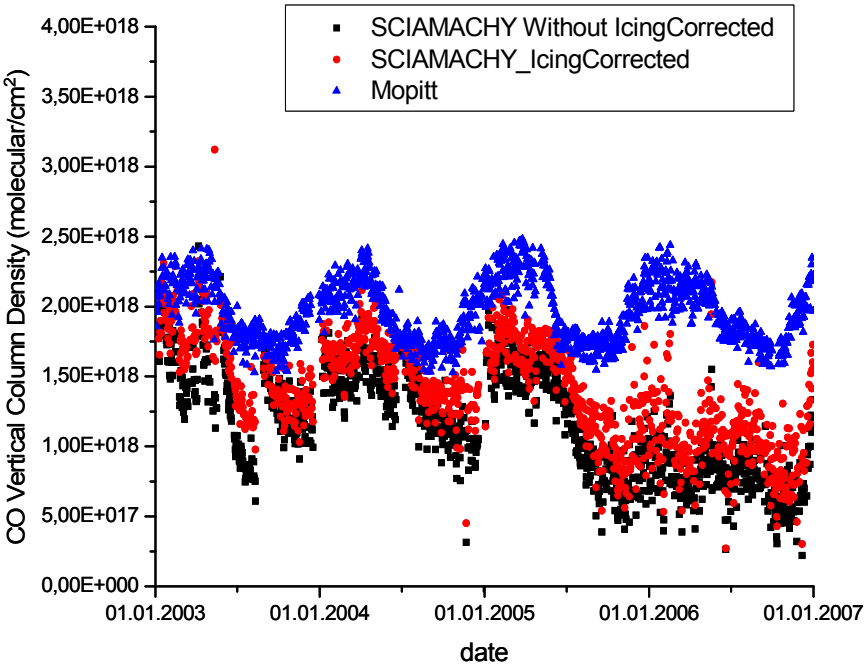

Figure 6.2: Time series of CO VCDs over the Sahara. The black symbols indicate the results of the original IMAP retrieval. The red symbols indicate the respective results after applying the CH_4 normalization procedure. In blue the corresponding MOPITT results are shown.

6.3 Correction Using Variable Slit Functions

It was shown by Gloudemans *et al.* (2005) that the ice layer on the SCIAMACHY near IR detectors significantly affects the instrument slit function. The reason for this effect is probably multiple scattering between the ice layer and the surface of the detectors.

In this thesis the effect of the variable slit function is investigated in detail, and a correction procedure for the CO analysis is developed. The method consists of two steps.

a) First the best slit function for a given day is determined by performing a series of IMAP fits for different slit functions. From the respective fit residual, the best slit function for this day is determined. Besides Lorentian and Gaussian slit functions, also the results for Voigt line shapes are investigated in this thesis. It turned out that the Gaussian part of the slit function is negligible compared to the Lorentian part. From the dependence of the fit residual on the line width (FWMH) of the used slit function, the respective slit function for the minimum of the residual is determined. Since the H_2O and CH_4 absorptions in the CO fitting range are relatively weak, the determination of the best FWHM is performed in two neighboring spectral

intervals (2302.44 nm to 2324.49 nm and 2334.75 nm to 2355.12 nm). Results for Lorentian and Gaussian slit functions are shown in Figure 6.3 for SCIAMACHY measurements with thin and thick ice layer. The line width is found to be larger in the presence of a thick ice layer on the detector.

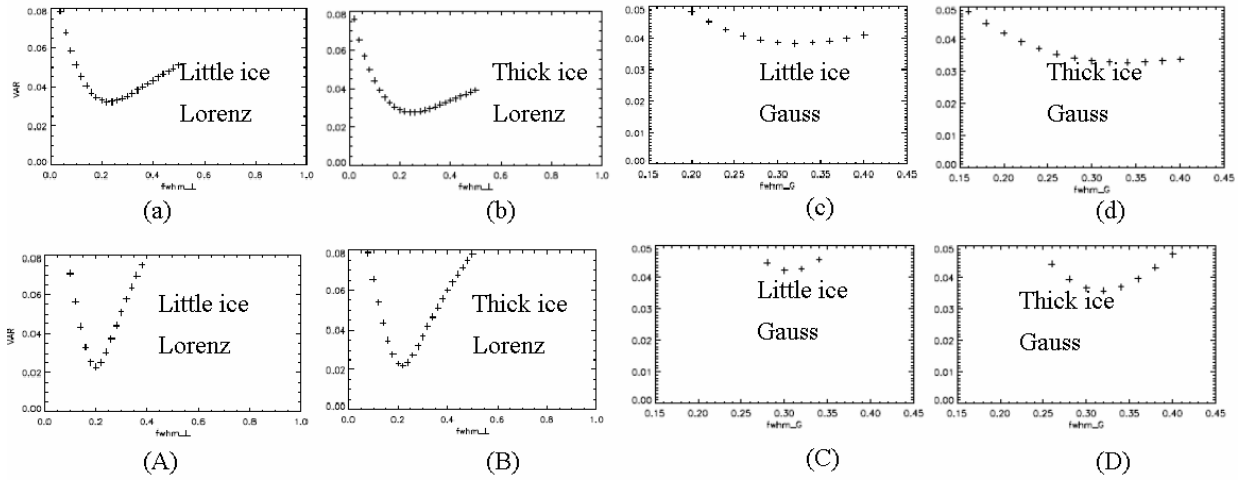

Figure 6.3: Variance of the fit residual depending on the width (FWHM) of the slit function used in the IMAP retrieval for Gaussian and Lorentian line shapes. Results are shown for thin and thick ice layers on the detector and for two different spectral ranges (capital letters: 580nm to 751nm, small letters: 320nm to 496nm).

For each day the optimum slit function is determined in this way. The respective results for the two wavelength intervals are shown in Figure 6.4. It can be clearly seen that the thickness of the ice layer has indeed a systematic effect on the derived line width. According to the assumption of multiple scattering, the line increases with increasing thickness of the ice layer. It can also be seen that the results in both selected wavelength ranges show a consistent temporal variation. However, it is also found that after 2005, still large variations of the line width are found, although the ice layer did not change significantly during that period. The reason for this behavior is not clear, but indicates that the throughput through the ice layer and the shape of the slit function are not related by a simple functionality.

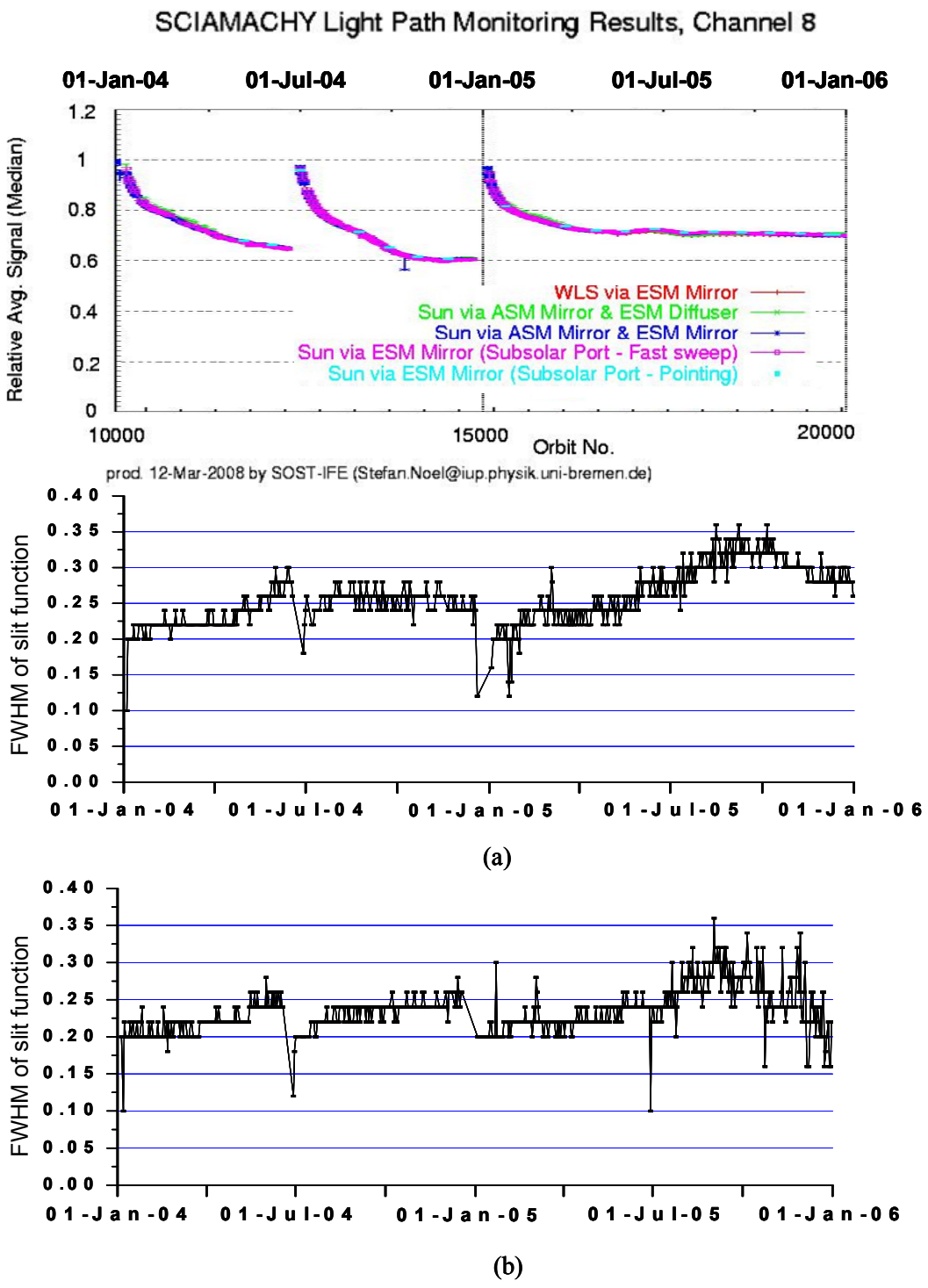

Figure 6.4: Time series of the retrieved slit function's FWHM which correspond to minimum fitting residuals in both wavelength ranges (a: 2302.44 nm to 2324.49 nm, b: 2334.75 nm to 2355.12 nm). The relative signal strength (top) is a measure of the thickness of the ice layer on top of the near-IR detectors (with low throughput for thick ice layer).

b) In a second step, the slit functions retrieved in both spectral ranges are averaged on a daily basis. Then a low order polynomial as function of time is fitted to the retrieved time series of daily values. Note that this fit is done separately between the different decontamination phases of the detectors. For a given day, the fitted value of the FWHM is then used for the IMAP CO retrieval. The results of the CO VCDs retrieved with this correction method are shown in Figure 6.5. Like for the other correction methods, improved results can be seen for part of the time series (e.g., during 2005). However, this correction method can not lead to sufficiently unbiased and consistent time series of CO VCDs.

From the results of all three correction methods it is conclude that although they are able to improve the quality of the CO VCDs at least for specific periods, these methods can not sufficiently correct all problems of the SCIAMACHY CO retrieval. One reason for these finding might be the effect of bad and dead pixels. As was shown by Buchwitz *et al.* (2007), the number and location of these pixels have a strong and systematic influence on the retrieved SCIAMACHY CO VCD. Since the number of bad and dead pixels increases with time, also time dependent biases of the SCIAMACHY CO VCDs should be expected.

Because of the remaining problems of the SCIAMACHY CO retrieval, it is decided to follow a completely new strategy in this thesis: a normalization procedure is developed and applied using MOPITT observations over oceans. This normalization method is described in detail in next chapter.

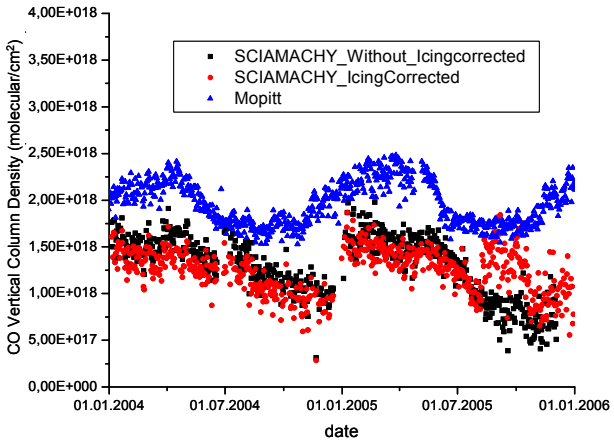

Figure 6.5: Time series of CO VCDs over the Sahara. The black symbols indicate the results of the original IMAP retrieval. The red symbols indicate the respective results after applying the method of variable slit functions. In blue the corresponding MOPITT results are shown.

7 Normalization Using MOPITT Data over the Oceans

The initial comparison between MOPITT and SCIA indicated that the difference between the CO VCDs measured by both instruments depends on latitude and time (probably related to changes in SZA and relative azimuth angle). Thus, no simple correction of the SCIAMACHY CO column densities (e.g., by adding a constant or time-dependent offset) is possible, and it is decided to apply a latitudinal and seasonal dependent correction of the offset in the SCIAMACHY CO VCDs using MOPITT observations over the oceans. The main justification of such a normalization procedure is that all important CO emissions sources are located over land and thus the CO distribution over the ocean can be expected to be relatively well mixed. In particular, in the lowest atmospheric layers no strong spatial gradients of the CO concentration should in general be expected. Thus, in spite of the low sensitivity of the MOPITT instruments for surface-near layers, CO VCDs retrieved from both sensors should show good agreement, if the a-priori assumptions in the MOPITT retrieval for the CO concentration in the lowest atmospheric layers are reasonable. Over oceans, far away from strong CO sources, this prerequisite should in general be well fulfilled. For the comparison with the MOPITT observations SCIAMACHY observations above low-lying clouds (cloud top heights between 0 and 2 km and effective cloud fractions > 20%) are selected, which have a rather similar height-dependent sensitivity compared to the MOPITT observations (the cloud properties are derived from the FRESCO algorithm (Wang *et al.*, 2008)). The height averaging kernels of the individual SCIAMACHY observations are applied to the coincident MOPITT measurements over the oceans before both data sets are compared. Thus, even if the true CO concentration in the low atmosphere differs from the MOPITT a-priori values, this should only have a small effect on the comparison. The remaining errors affecting the comparison of the CO VCD are estimated to be <5% for unperturbed profiles. In the case of effective transport of polluted air masses over the ocean the corresponding error might be larger.

For the normalization procedure, the remote ocean area is divided into 15 latitude bins from north to south (see Figure 7.1). Offsets ΔCOlat between SCIAMACHY and MOPITT VCDs for these regions are calculated on a daily basis according to the following equation:

$$\Delta CO(lat_i) = \overline{CO}_{MOPPIT,above\ cloud\ height}(lat_i) - \overline{CO}_{SCIA}(lat_i) \quad 7.1$$

Here $\overline{CO}_{SCIA}(lat_i)$ indicates the mean value of all SCIAMACHY CO VCDs within the selected latitude bin which fulfill the cloud selection criteria (CF>20%, cloud top height <2km). $\overline{CO}_{MOPPIT,above\ cloud\ height}(lat_i)$ indicates the mean value of all MOPITT partial CO VCDs above the average cloud top height of the SCIA observations within the selected latitude bin. The offset $\Delta CO(lat_i)$ is determined on a daily basis and interpolated (using splines) to a latitudinal grid of 1°.

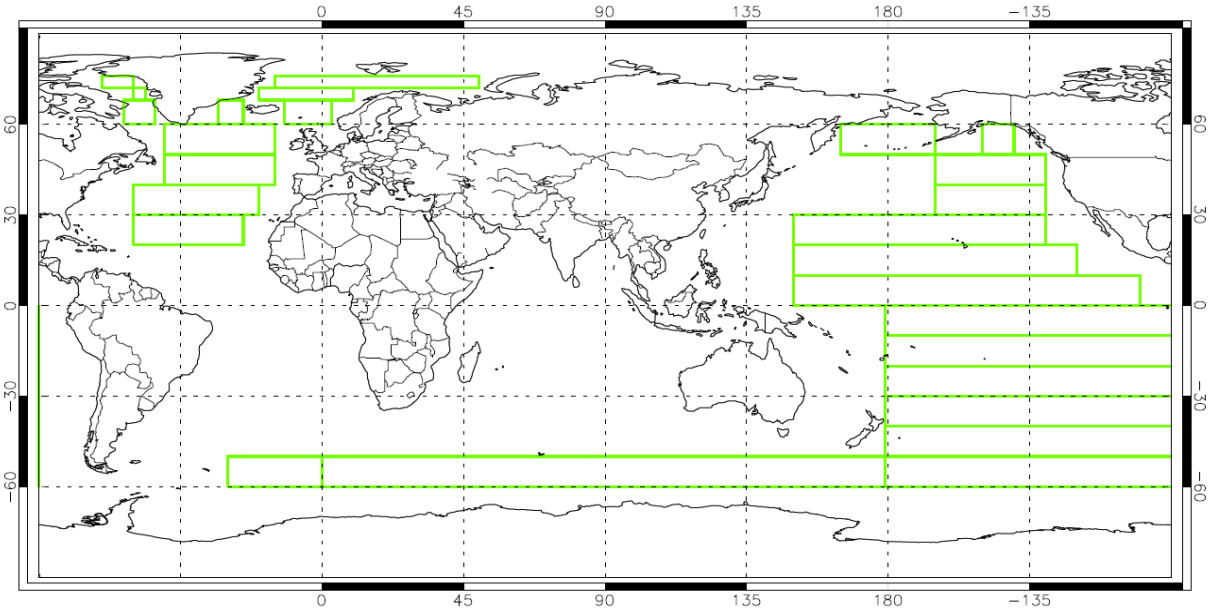

Figure 7.1: Latitude bins selected over the remote ocean for the normalization procedure using MOPITT data.

Assuming that the CO VCDs measured by MOPPIT over remote ocean areas are correct and that the bias of the SCIAMACHY CO VCD does not depend on longitude, the determined offset between MOPPIT and SCIAMACHY $\Delta CO(lat_i)$ can be used for the correction of the SCIAMACHY CO observations on a global scale.

In order to verify our normalization process MOPPIT CO VCDs and SCIAMACHY CO VCDs are compared over the continents; in Figure 7.2 the results over the Sahara are shown (additional comparisons are shown in chapter 9).

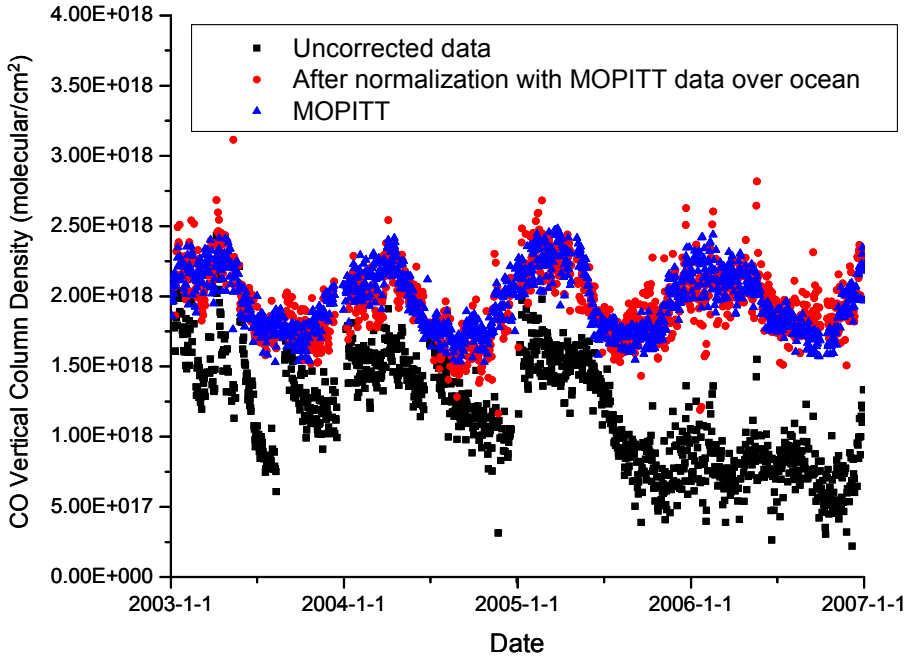

Figure 7.2: Comparison between MOPITT CO VCDs and SCIAMACHY CO VCDs averaged over Sahara (20°N to 28°N; 8°W to 28°E) for each day in the period 2003 to 2006 with and without applying MOPITT normalization.

As expected, after the normalization procedure, the agreement between the MOPITT and SCIAMACHY data is largely improved.

It should be noted that the SCIAMACHY CO VCDs normalized in this way can not be considered as an independent data set anymore. In particular, its accuracy depends critically on the accuracy of the MOPITT data: systematic errors of the MOPITT data will almost directly result in similar errors of the normalized SCIAMACHY data set. Nevertheless, the normalized SCIAMACHY CO data are useful, since observations in the near IR are sensitive to the total atmospheric CO VCD (see e.g., Figure 5.4), SCIAMACHY data can yield important information on the location and strength of local emission sources. Here in particular the comparison of CO VCDs from SCIAMACHY (and also MOPITT) over continental sources with model data is of great interest (see chapter 9).

8 Retrieval Results

8.1 New Data Set of SCIAMACHY CO VCDs

In this thesis a new CO VCD product from near IR observations of the SCIAMACHY instrument is developed. It is based on the original IMAP CO algorithm (Frankenberg *et al.*, 2005a), but includes also corrections for the well-know icing problem (see chapter 7) and the effects of clouds (our data set includes observations with cloud fraction <20%; see chapter 5). Figure 8.1 shows the global mean average CO VCD (2003 to 2005) from this new dataset. It is obtained after applying the normalization procedure using MOPITT observations over ocean, skipping all observations with effective cloud fractions >20%, and applying the cloud correction. Large-scale CO enhancements over biomass burning and industrial regions can be clearly identified. In addition to these large-scale features the map also shows considerable fine structure.

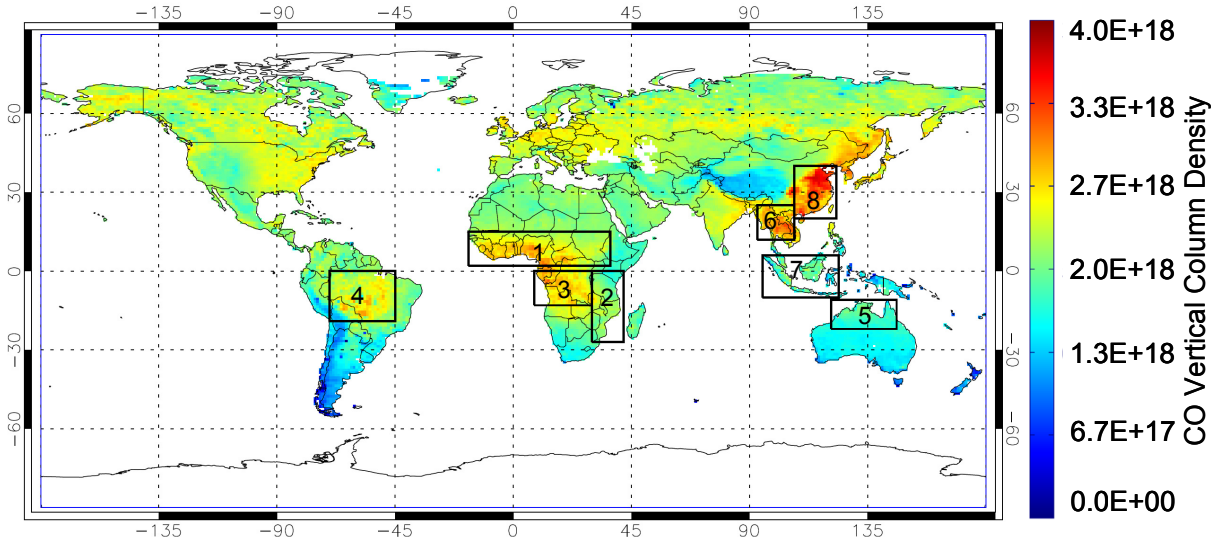

Figure 8.1: Mean CO VCD retrieved from SCIAMACHY 2003 to 2005 (units: molec/cm^2). The boxes indicate regions of strong biomass burning or industrial activity that are selected for the comparison between satellite observations and model simulations (see chapter 9). All observations with effective cloud fractions >20% are discarded, and the cloud correction, as described in the text, is applied.

Figure 8.2, Figure 8.3 show yearly and seasonal averages of three years of SCIAMACHY global measurements (2003, 2004, and 2005). Well-known major source regions of CO located in South America, Africa, and China are clearly visible for all three years, and considerable source strength variations from year to year are apparent. Also visible is the inter-hemispheric gradient with much higher CO columns over the northern hemisphere. In South America and Africa, biomass burning is presumed to contribute most to the seasonal patterns. The seasonal variations of the global distribution of biomass burning events can be well observed by the ATSR sensor on board the ERS-2 satellite. Figure 8.4 shows seasonal fire counts of the three years (2003, 2004, and 2005) measured by ATSR. The areas with high fire frequencies correlate well with high abundances of CO, substantiating the assumption that the CO enhancements stem from biomass burning. The detailed comparison is shown in chapter 9.

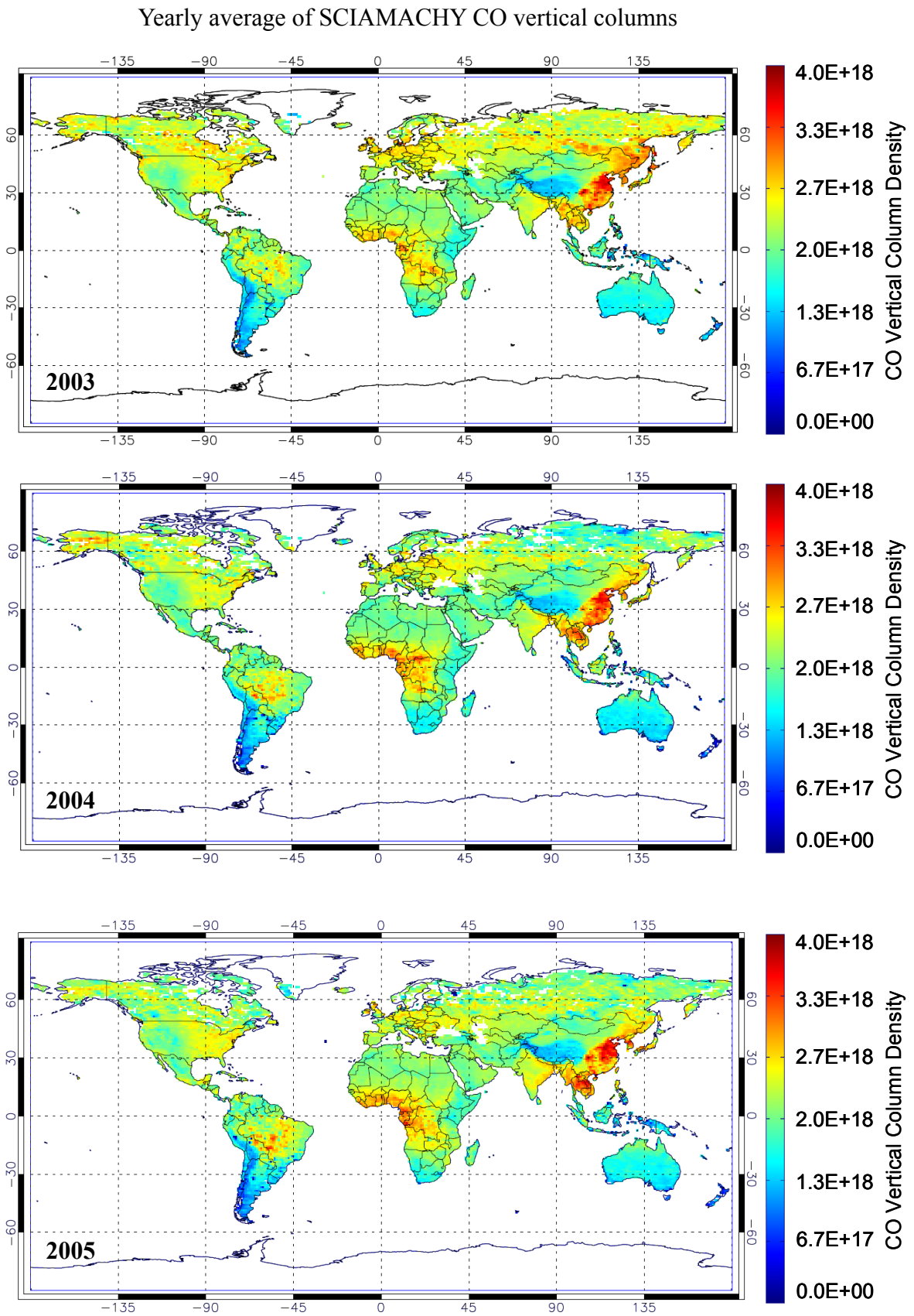

Figure 8.2: yearly averages of SCIAMACHY CO vertical columns from 2003 - 2005. The normalization procedure using MOPITT observations over ocean (see chapter 7) has been applied to all data, all observations with effective cloud fractions >20% are discarded, and the cloud correction, as described in the text, is applied.

Seasonally average of SCIAMCHY CO vertical columns

Jan. to Mar. of 2003~ 2005

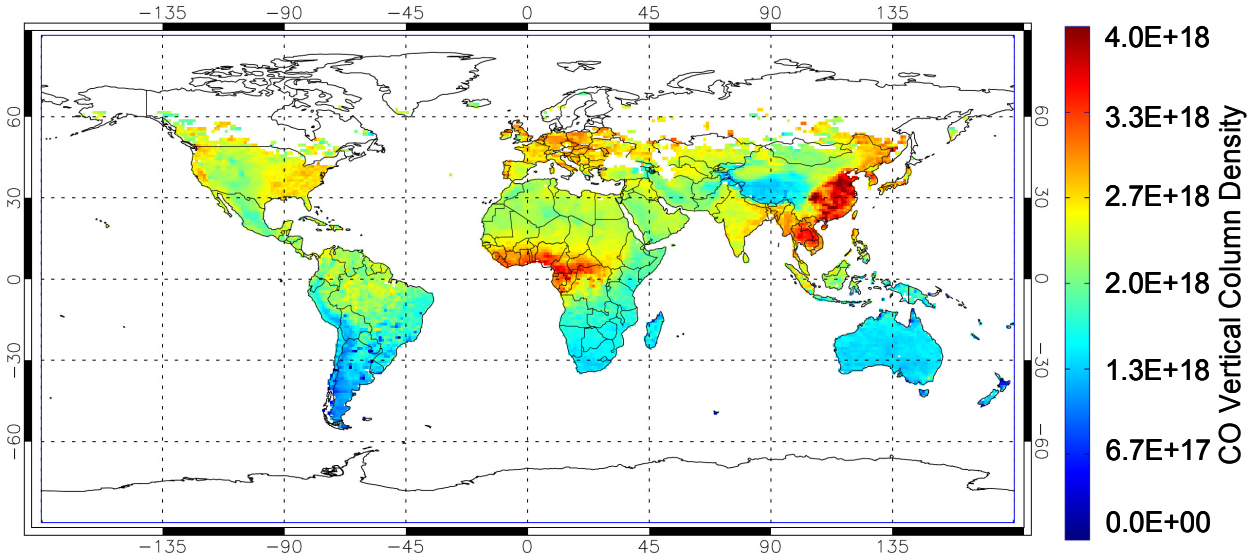

Apr. to Jun. of 2003~ 2005

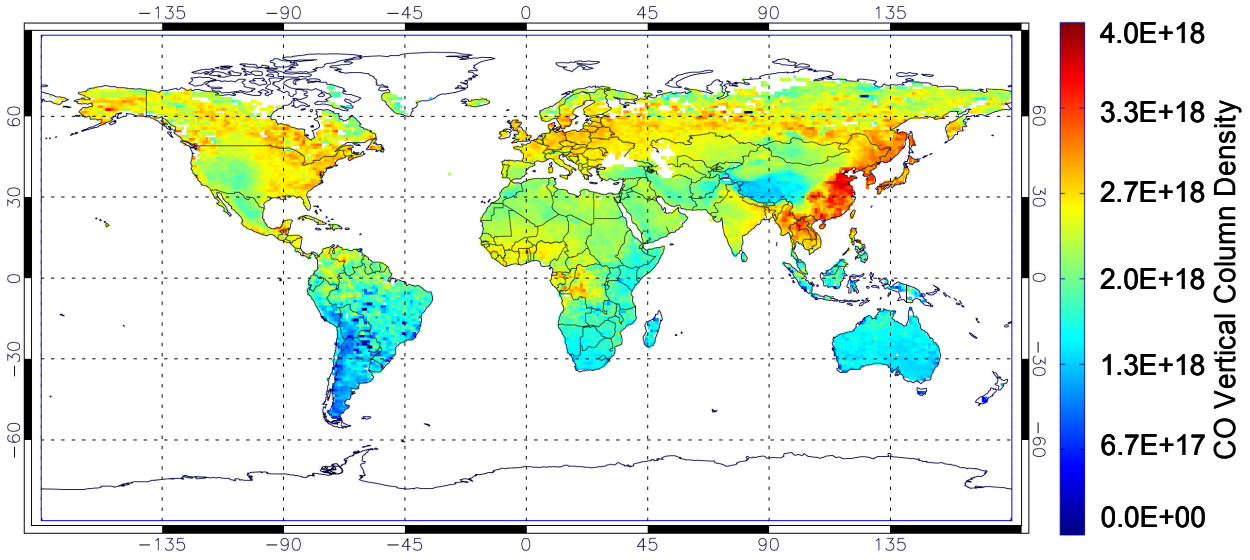

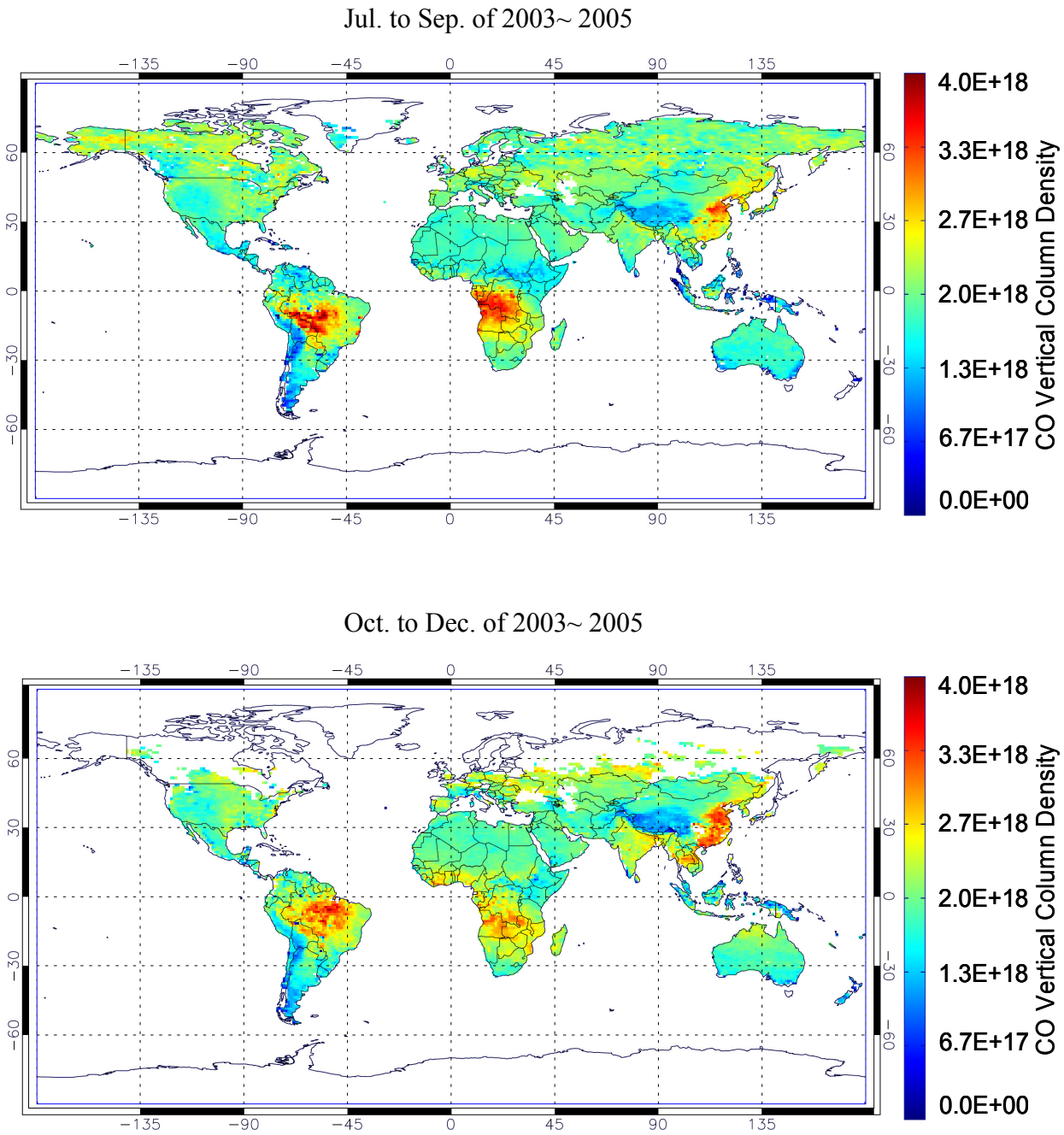

Figure 8.3: Seasonally averages of SCIAMACHY CO vertical columns from 2003 - 2006. The normalization procedure using MOPITT observations over ocean (see chapter 7) has been applied to all data, all observations with effective cloud fractions >20% are discarded, and the cloud correction, as described in the text, is applied.

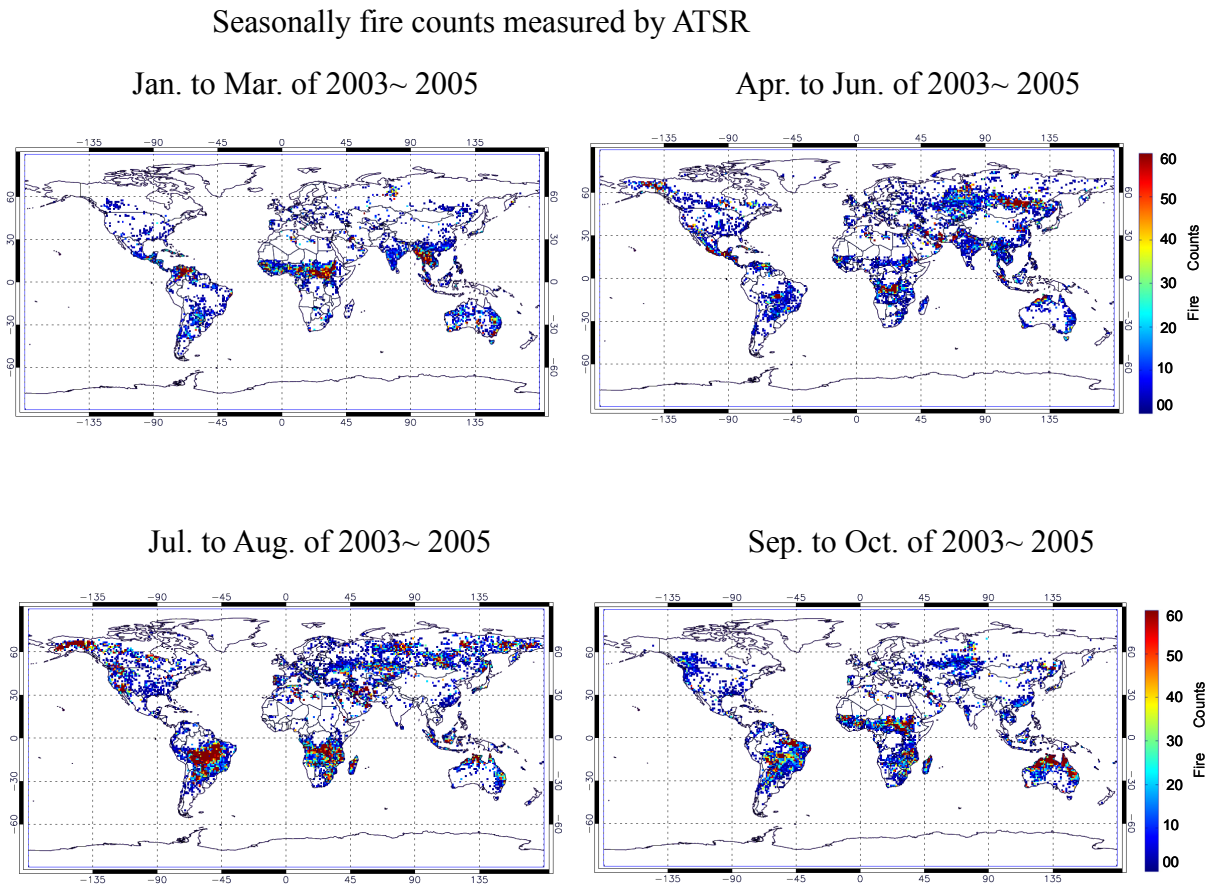

Figure 8.4: Seasonal fire distributions from 2003 to 2005. Displayed are fire counts measured by the ATSR Sensor on board the ERS-2 satellite.

Over China, where biomass burning is much less, anthropogenic emission is considered as the main source of CO. In Figure 8.5 a zoom of the multi-year average CO (Figure 8.1) over China is presented together with maps of MOPITT CO VCD, the population density and the distribution of coal mines. It is obvious that the patterns of the CO VCD compare better with the population density than with the distribution of coal mines. In particular, the highest CO VCDs coincide with the location of major Chinese cities. One interesting finding is the rather high CO VCD over the area indicated by the blue circle. Compared to other retrievals of the SCIAMACHY CO VCD (Buchwitz *et al.*, 2007) our CO analysis yields systematically higher values, probably indicating the strong importance of an appropriate correction of the influence of clouds on the SCIAMACHY CO retrieval.

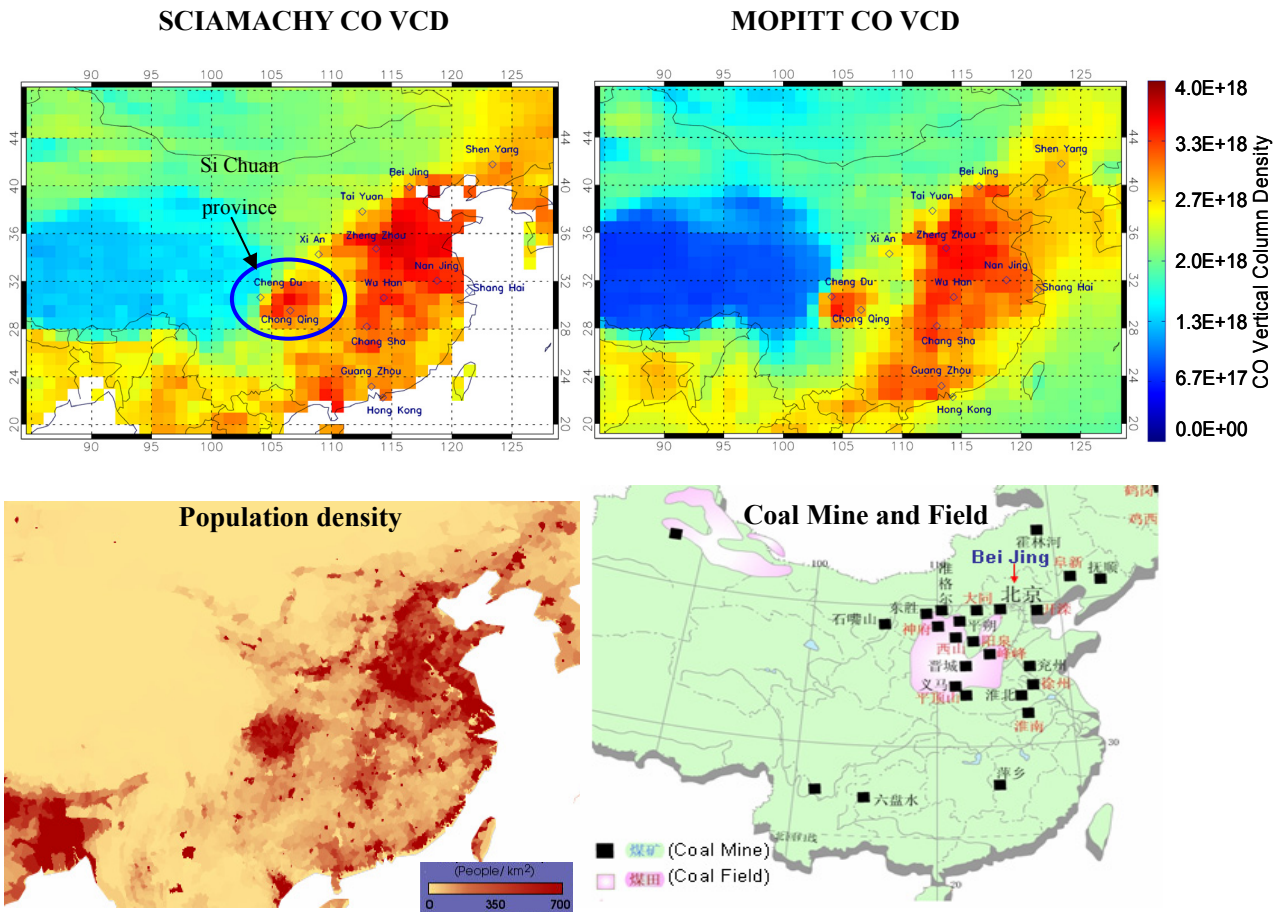

Figure 8.5: Comparison of the spatial distribution of CO VCD (average 2003 to 2005) over China derived from SCIAMACHY (top left) and MOPITT version 4 (top right) with the population density (bottom left) and the location of coal mines (bottom right). The blue circle in the map with the CO distribution indicates an area, where other SCIAMACHY algorithms (Buchwitz *et al.*, 2007) show much smaller column densities, which is probably related to the effect of clouds.

(The population density map is obtained from http://veimages.gsfc.nasa.gov/116/pop density. jpg.)

(The distribution of coal mine/field of China is obtained from http://www.eku.cc/xzy/sctx/121261.htm.)

8.2 Comparison of CO Vertical Columns from SCIAMACHY, MOPITT and Ground-based FTIR

In order to validate our CO VCD product, it is necessary to compare it with CO VCDs derived from independent observations. For that purpose, in this section SCIAMACHY CO VCDs are compared to the CO VCD from ground-based Fourier-Transform Infrared (FTIR) spectrometers and MOPITT observations. The ground-based correlative data are collected from various stations of the Network for the Detection of Atmospheric Composition Change (NDACC, http://www.ndsc/ncep.noaa.gov), which are obtained from daily solar absorption measurements under clear-sky conditions.

This thesis selects the FTIR ground based stations according to the following criteria: First, the measurements should be located over the continents. Second, the surface elevation of the FTIR measurements should be close to sea level height. Five FTIR stations, located in both the northern and southern hemisphere, are selected according to these criteria. To minimize the statistical uncertainties of the SCIAMACHY observations, the selected satellite observations include all SCIAMACHY pixels centered within 2.5 latitude and 10 longitude around the FTIR stations (Dils *et al.*, 2006). Figure 8.6 shows the comparison of the time series from SCIAMACHY CO VCDs (monthly means) and ground-based FTIR CO VCDs (daily values). In general, the time series of both data sets show reasonable agreement. However, it is also obvious that the SCIAMACHY data show a strong scatter, especially for locations with low numbers of individual SCIAMACHY observations (blue lines). This is the case for stations like Lauder, where most of the surrounding areas are ocean and thus many observations are discarded due to the very low reflectance over oceans. The best agreement is found for stations with high surface albedo like e.g., Wollongong, where in particular the seasonal variation is well captured by the SCIAMACHY observations.

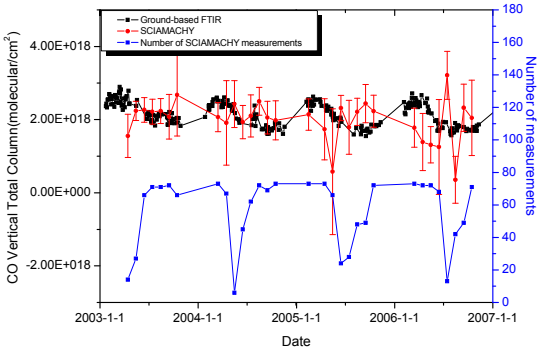

(a) Kiruna station, Sweden

(67.89N, 21.10E)

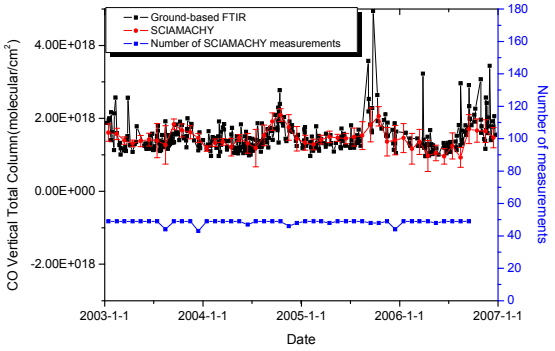

(b)Wollongong station, Australia

(34.45S, 150.88E)

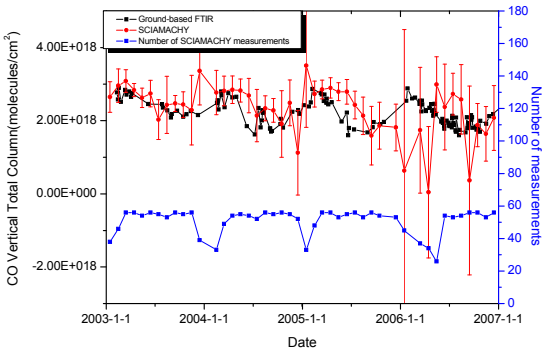

(c) Bremen station, Germany

(53.04N, 08.47E)

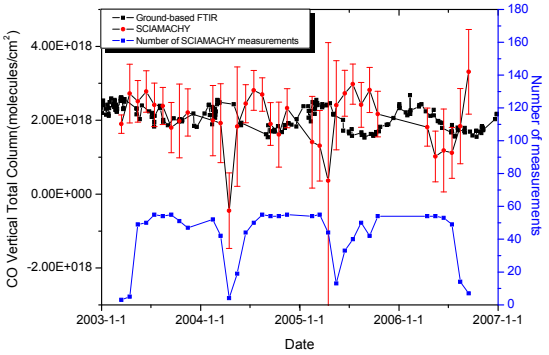

(d) Harestua station, Norway

(60.02 N, 10.8E)

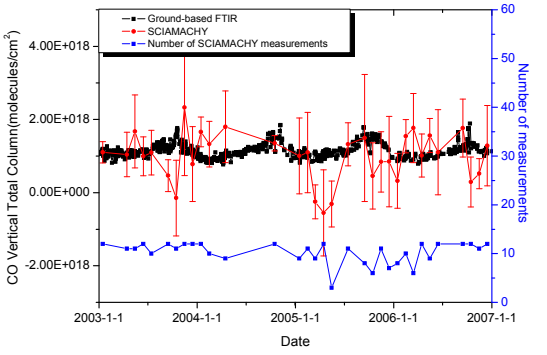

(e) Lauder station, New Zealand

(45.05S, 169.67E)

Figure 8.6: Monthly mean comparisons between SCIAMACHY and ground-based FTIR observations. The error bar of SCIAMACHY refers to the unbiased estimator of a weighted population variance.

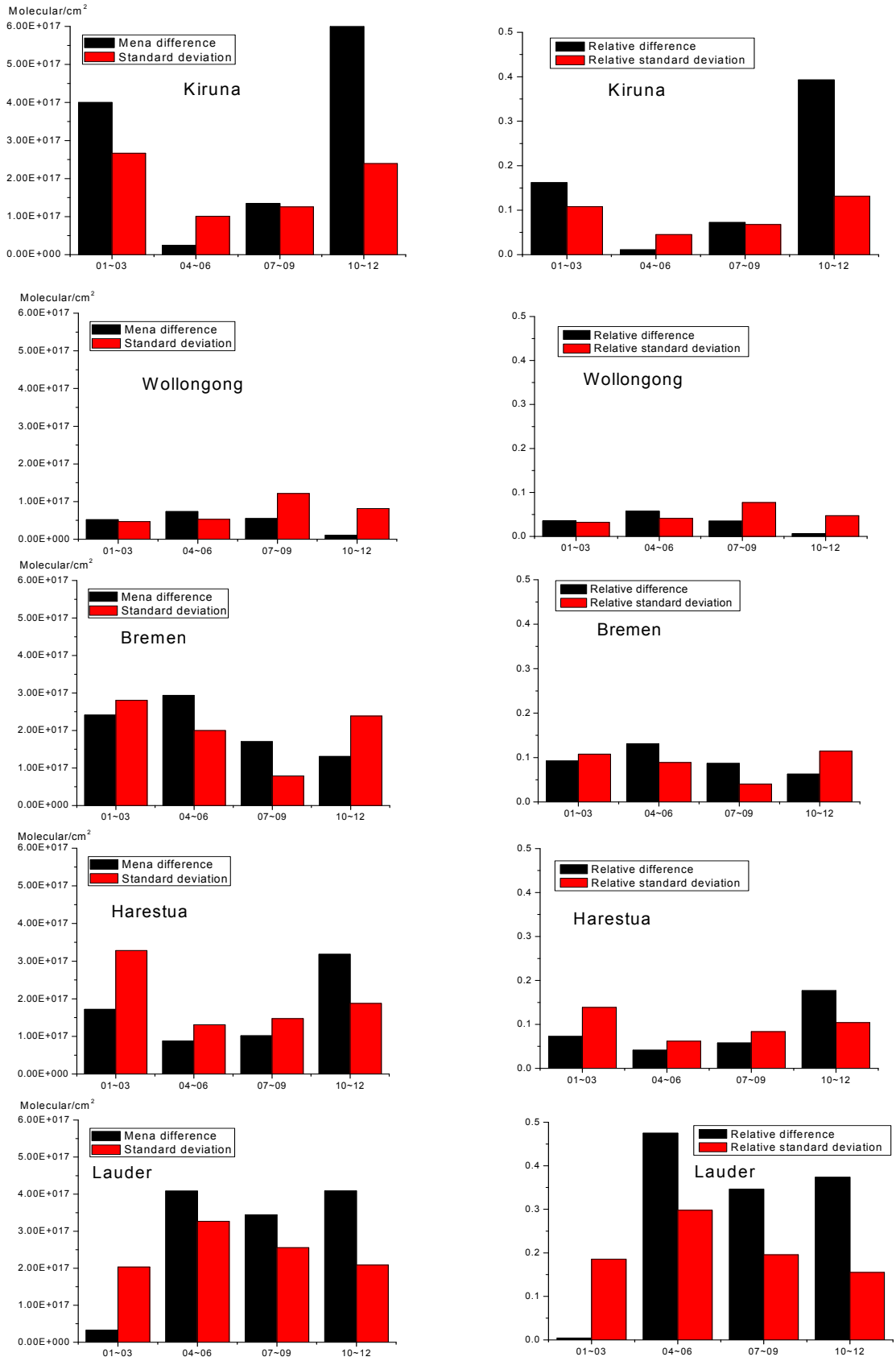

Figure 8.7: Seasonal mean difference and standard deviation of SCIAMACHY and ground-based FTIR measurements for 2003 – 2005. The left side plots are absolute differences and standard deviations; the right side plots are relative differences and standard deviations.

The differences between the two datasets can be seen more clearly in Figure 8.7, which shows the seasonal mean difference and standard deviation of both datasets. Due to the high surface albedo and SNR, the smallest mean difference and standard deviation is found in Wollongong (about 1% to 6%). Much higher relative difference is found in Lauder (about 20% to 30%) because of only few SCIAMACHY measurements. For Harestua, good agreement could be found for all seasons, which is <15%. For Kiruna, except winter, the difference between both datasets is <10%. In the winter, due to the larger solar zenith angle and the few cloud free measurements, the difference between the two datasets is much larger (about 30%). For Bremen, the relatively large differences are probably caused by the combined effects of instrument degradation, few effective measurements and low surface albedo.

Besides the rather high uncertainty of the individual SCIAMACHY observations, also the large difference in the size of the probed air masses of satellite and ground-based data might contribute to the observed differences. For CO observations the size of the SCIAMACHY pixel is 30*120km^2, and the retrieved satellite CO VCD represents an average of the CO VCD across that area (Dils *et al.*, 2006).

Unfortunately, there is no ground-based FTIR measurement in either biomass burning or heavily polluted industrial regions. Such FTIR measurements close to strong CO emission sources would have been very valuable for this study.

In this thesis the SCIAMACHY CO columns are also compared to MOPITT version 4 CO columns over the continents. Here it should be noted that such a comparison cannot be regarded as a completely independent validation, because the SCIAMACHY CO VCDs have been normalized using MOPITT observations over the oceans. But the comparison of the spatial and temporal patterns over the continents can still yield important information on the consistency of the results of both satellite sensors.

In a first step (Figure 8.8) the time series of the monthly mean CO VCDs over the areas indicated in Figure 8.1 are investigated (one example of the comparison for a region without strong CO emission sources is already presented in Figure 7.2). In the left columns of Figure 8.8 the time series using all observations within the selected areas are shown (for SCIAMACHY observations with an effective cloud fraction <20% are used). In the center columns of Figure 8.8

only collocated, coincident SCIAMACHY and MOPITT observations are used. In the right columns the respective numbers of observations are shown (notice the logarithmic scale). If only coincident observations are selected, the number of SCIAMACHY observations is strongly reduced (by a factor 10 to 100).

(1): Central Africa

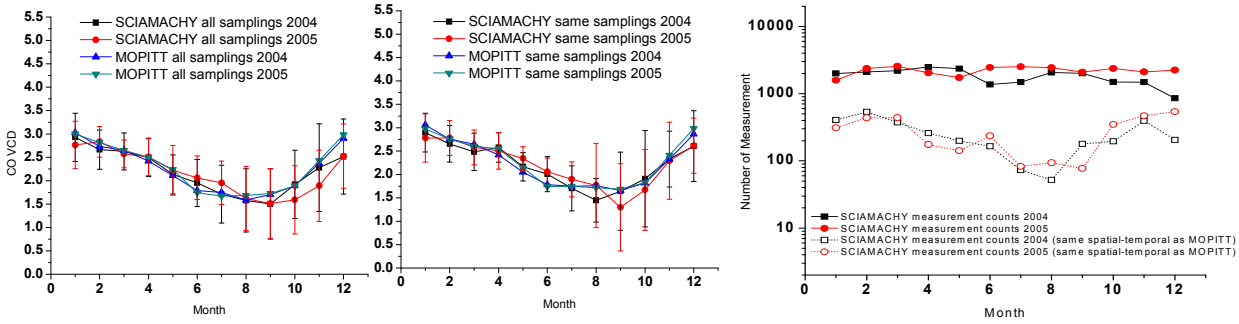

(2): Southeast Africa

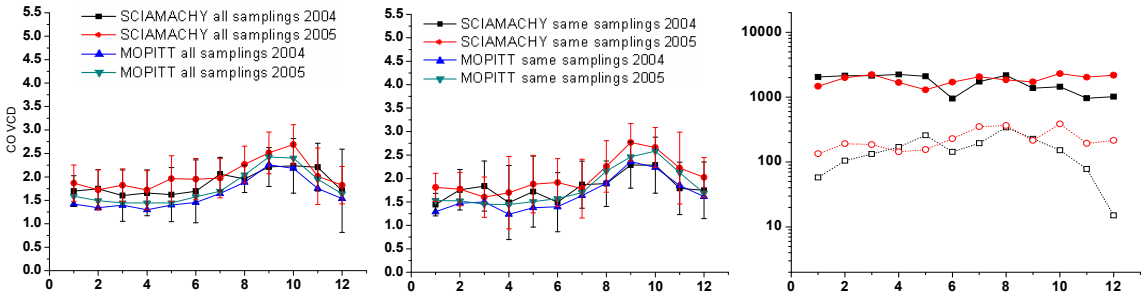

(3): Southwest Africa

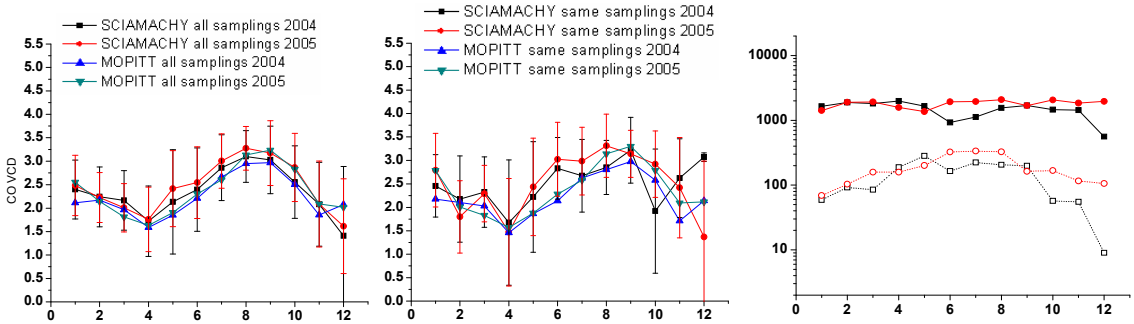

(4): Central South America

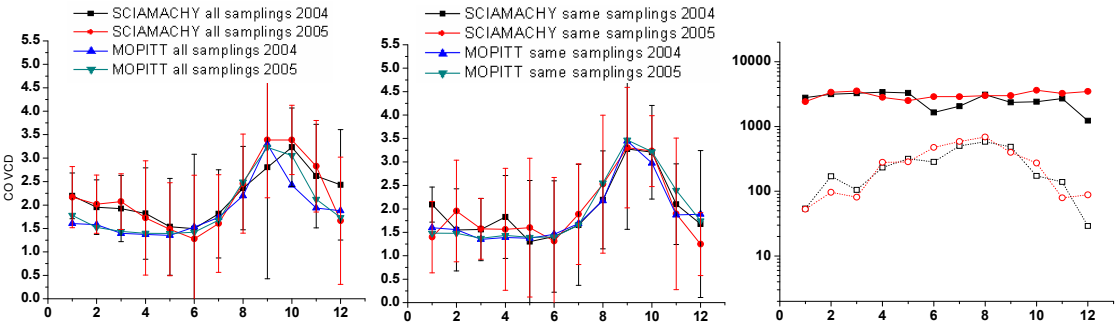

(5): Northern Australia

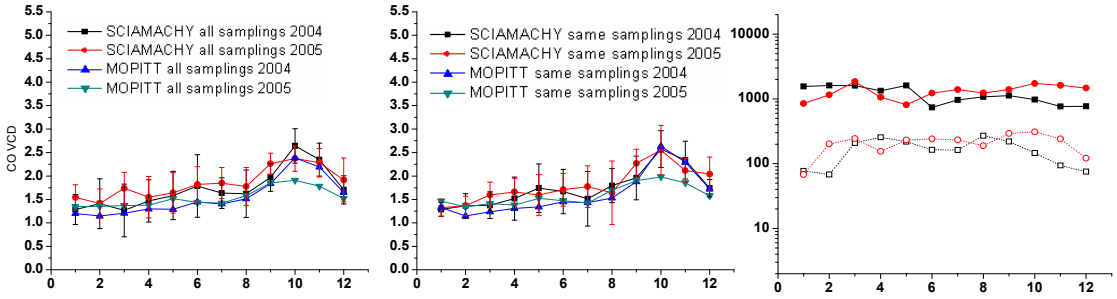

(6): Southern Asia

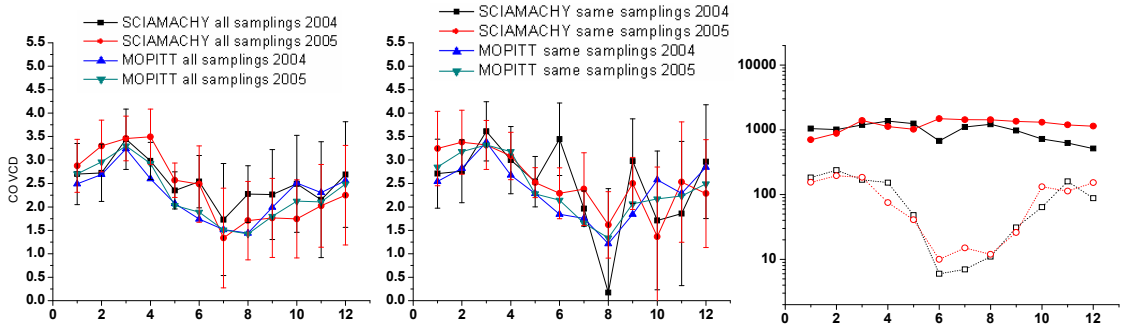

(7): Indonesia

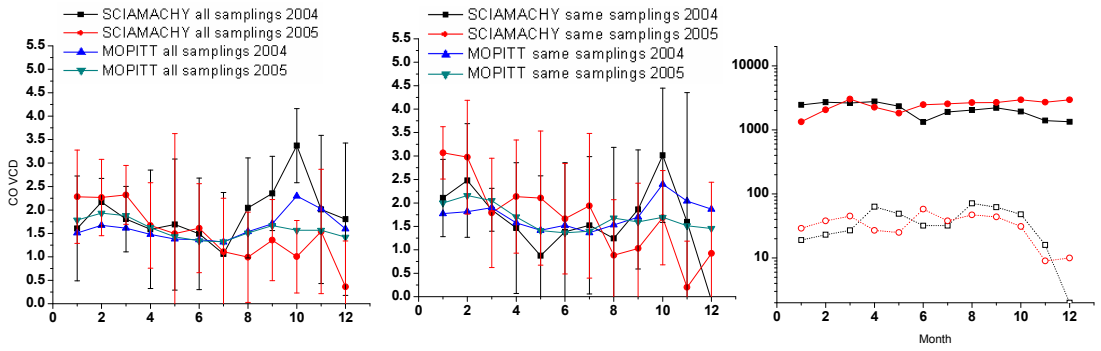

(8): East China

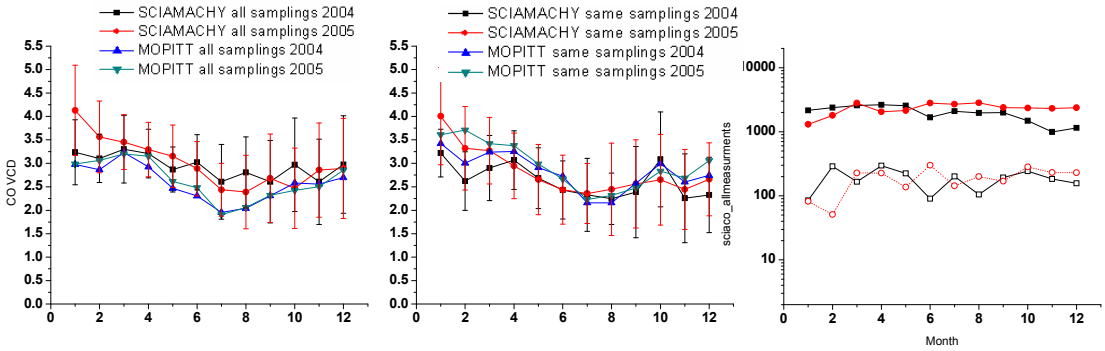

Figure 8.8: Comparison of the monthly mean CO VCDs (in units of 10^{18} molec/cm^2) derived from SCIAMACHY and MOPITT. In the left column of the figure all measurements within the selected regions (see Figure 8.1) are considered. In the middle column only collocated and coincident observations are used. The error bar of SCIAMACHY refers to the unbiased estimator of a weighted population variance. In the right column the number of selected observations are indicated (please notice the logarithmic scale).

The interpretation of the results of the comparison is not straightforward, because the true vertical CO concentration profile is not known and different assumptions on the a-priori profile are made for the two datasets. For the MOPITT CO VCDs used here, the a-priori even depends on location and season. Thus the comparison exercise can only be interpreted in a semi-quantitative way.

Over the biomass burning regions very similar seasonal cycles are found in both data sets. In most cases the SCIAMACHY CO VCDs are systematically higher than the MOPITT CO VCDs, indicating the higher sensitivity of SCIAMACHY towards the surface.

For the comparison of coincident observations of both sensors (middle columns of Figure 8.8), similar results are found, but now more direct conclusions can be drawn. The disagreement between both data sets can be seen as an indicator how well the MOPITT a-priori fits the true atmospheric CO concentration profile. Over most biomass burning regions the MOPITT a-priori CO profile appears to slightly underestimate the CO concentration in the lowest atmospheric layers. However, in contrast to most biomass burning regions, the MOPITT a-priori seems to describe the atmospheric CO profiles over East China rather well. Of course, at least part of the deviations might also be caused by other error sources. Especially for some regions (e.g., South Asia or Indonesia) and months the number of SCIAMACHY observations is relatively small and the corresponding uncertainty of the SCIAMACHY observations is high. In other parts of the world, especially over South America, also the frequent occurrence of high clouds increase the uncertainty of the SCIAMACHY (and also MOPITT) observations (see also Figure 5.5).

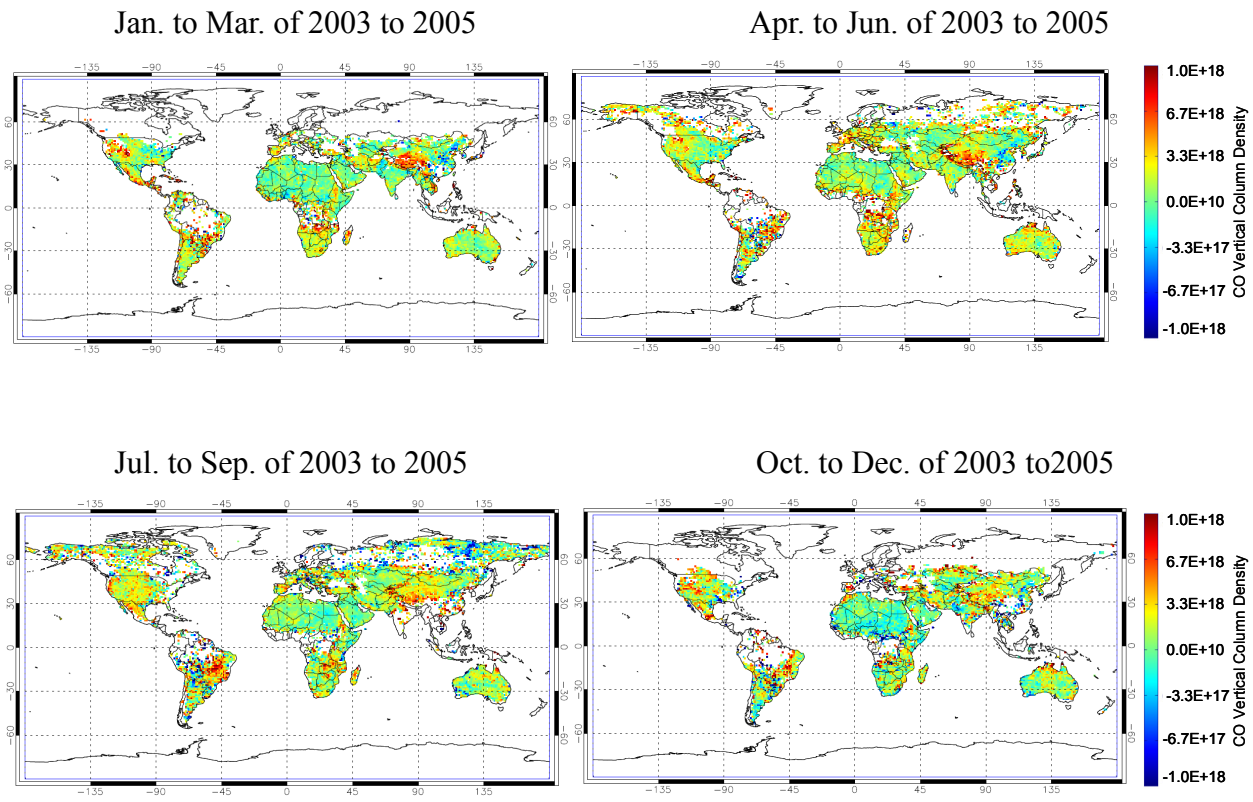

Figure 8.9: Spatial distribution of averaged seasonal differences between SCIAMACHY and MOPITT measured total columns (SCIAMACHY – MOPITT) with the same spatial-temporal samplings.

In a second exercise the global distributions of the CO VCDs derived from both satellite instruments are compared for different seasons. In Figure 8.9 the respective differences are shown using only coincident measurements. In general, again good overall agreement is found with slightly higher SCIAMACHY CO VCDs over most parts of the world. The largest differences between both sensors are found over South America and South-East Africa during the biomass burning seasons (see also Figure 8.8).

9 Comparison between Satellite Measurements and Model

This chapter compare the satellite observations of the two satellite sensors (SCIAMACHY and MOPITT) with results from the three chemistry climate models MATCH (Model of Atmospheric Transport and Chemistry, Max-Planck-Institute for Chemistry, (von Kuhlmann *et al.*, 2003)), EMAC (ECHAM5/MESSy Atmospheric Chemistry modeling system, Max-Planck-Institute for Chemistry, (Jockel *et al.*, 2006)) and GEOS-CHEM (Goddard Earth Observing System, (Bey *et al.*, 2001)). In addition, the CO emissions used in the models and measured fire counts (as a qualitative indicator for CO emissions from biomass burning) are included in this comparison. Like for the comparison between SCIAMACHY and MOPITT observations in the previous chapter, first the time series over the selected biomass burning regions (see Figure 8.1) and East China are shown. Second, global maps of the differences for different seasons are presented.

Before these comparisons are presented and discussed, some general aspects of this comparison should be briefly considered. In contrast to the comparison between MOPITT and SCIAMACHY (chapter 8), for the comparison between measurements and model results information on the vertical CO concentration profile is available from the model simulations. This information is used to correct for the height-dependent sensitivities of both sensors. Of course, the simulated CO profiles do not necessarily represent the true atmospheric profiles. Nevertheless, in general they should describe the atmospheric CO profiles better than the a-priori assumptions used in the satellite retrievals (at least for SCIAMACHY, for which a fixed a-priori profile is used). Thus from the comparison between observations and model results, more precise conclusions on the agreement between both sensors than from their direct comparison might be drawn, especially in cases for which good agreement between model simulations and observations is found.

For the comparison between measurements and model results, it should be possible to draw the following conclusions:

-If it is assumed that the model simulations represent the true atmospheric profiles (and the measurements have no errors), the exact agreement between measurements and model simulations (for the part of the atmospheric profile for which the sensitivity of the satellite

observation is greater than zero) is naturally expected.

-However, agreement between measurements and model results might also be found as a result of compensating errors of measurements and models. Thus agreement between observations and model results should be seen as an indication, but not as proof, that both measurements and model simulations are correct.

-If disagreement between measurements and model results is found, this is an unambiguous sign of errors in the measurements, in the model, or both.

It should also be noted that - for practical reasons - the altitude dependent sensitivity is considered in different ways for both satellite instruments. For the comparison of the model results and SCIAMACHY observations, the (relative) model profiles (instead of the standard profile, see Figure 5.3) are used to correct for the height dependent measurement sensitivity. According to equations 5.6 and 5.7 it is get:

$$VCD_{SCIA,\mathrm{mod}el} = \frac{VCD_{SCIA} \cdot AMF_{geo}}{AMF_{total,\mathrm{mod}el}} \qquad 9.1$$

with

$$AMF_{total,\mathrm{mod}el} = \frac{\sum_z BOX_{AMF}(z_i) \cdot c_{CO,\mathrm{mod}el}(z_i)}{\sum_z c_{CO,\mathrm{mod}el}(z_i)} \qquad 9.2$$

with $c_{CO,model}(z_i)$ the CO concentration of the model simulation at layer i.

The resulting $VCD_{SCIA,model}$ is then compared to the CO VCD obtained from the vertical integration of the CO profile from the model simulation.

For the comparison between the model results and MOPITT observations, the CO VCD from the MOPITT v4 data product is taken and compared to the CO profiles from the model simulations after applying the MOPITT averaging kernel and *a priori*.

$$VCD_{\mathrm{mod}el,MOPITT} = \sum_z x_a(z_i) + A(z_i)(x_{Model\,\mathrm{Pr}ofile}(z_i) - x_a(z_i)) \qquad 9.3$$

Here $VCD_{model,MOPITT}$ is the model CO VCD after applying the MOPITT averaging kernel $A(z_i)$

and *a priori* $x_a(z_i)$.

Despite the different formal ways of the comparison, the interpretation of the respective comparison results is identical: cases for which the satellite measurements are higher (lower) than the model results indicate an underestimation of the true CO profile by the model, e.g., caused by an underestimation of the emission sources (similar conclusions can of course also be drawn for the accuracy of the measurement). However, one important difference in the interpretation of the comparisons for the different sensors exists: the results of the comparisons allow only conclusions for the altitude range, for which the satellite instruments are sensitive. In particular, only the comparison between SCIAMACHY observations and model simulations can yield information about the CO distribution in the lowest atmospheric layers.

9.1 Comparison of Time Series

In Figure 9.1 the time series of monthly averaged CO VCDs retrieved from both satellite sensors together with the corresponding CO VCDs from the model simulations are presented for the regions shown in Figure 8.1. Note that only coincident pairs of measurements and model results are considered (but the selected cases differ for the different combinations of satellite sensors and models). The height-dependent sensitivities of SCIAMACHY and MOPITT are considered as described above.

(1): Central Africa

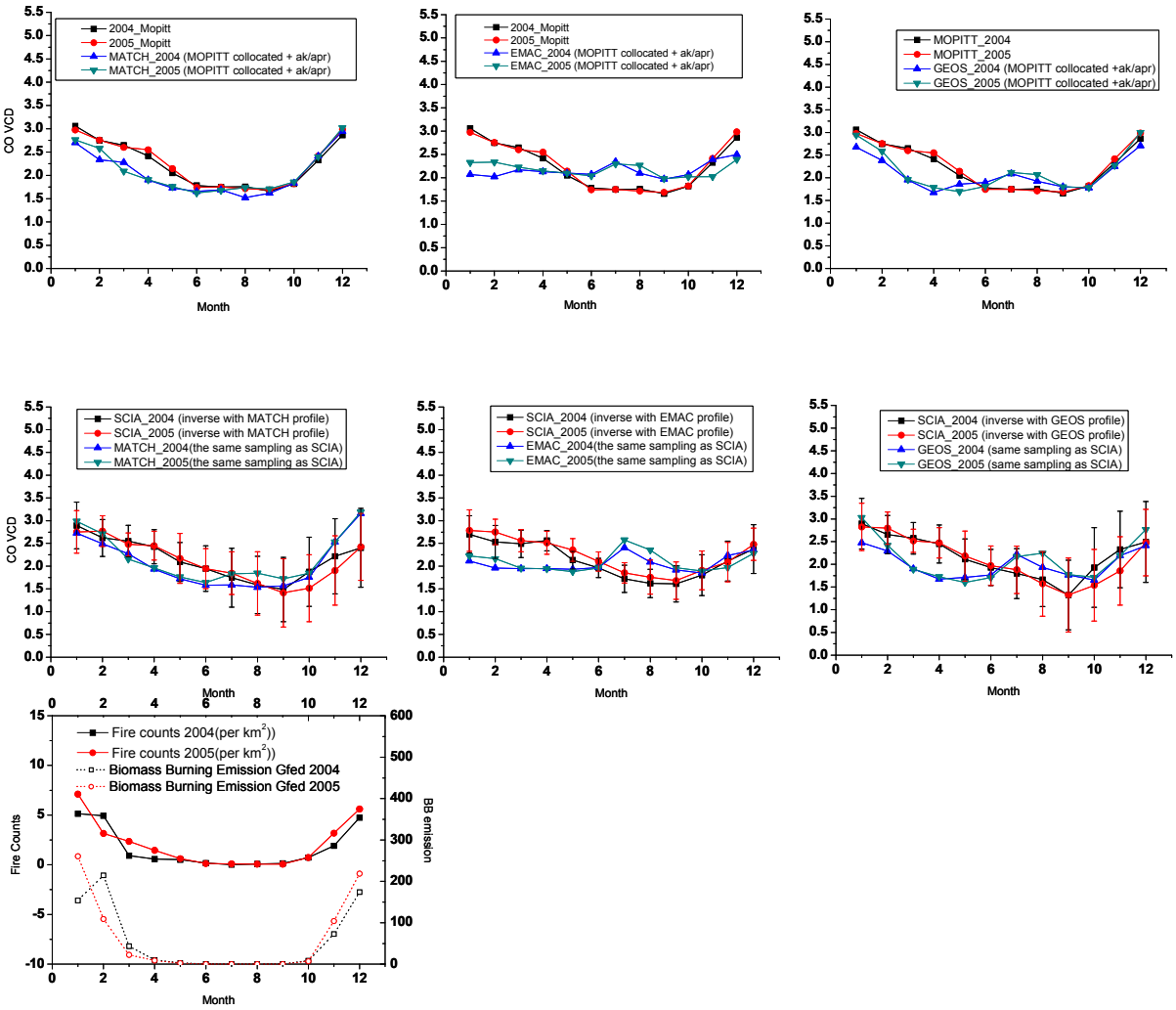

(2): Southeast Africa

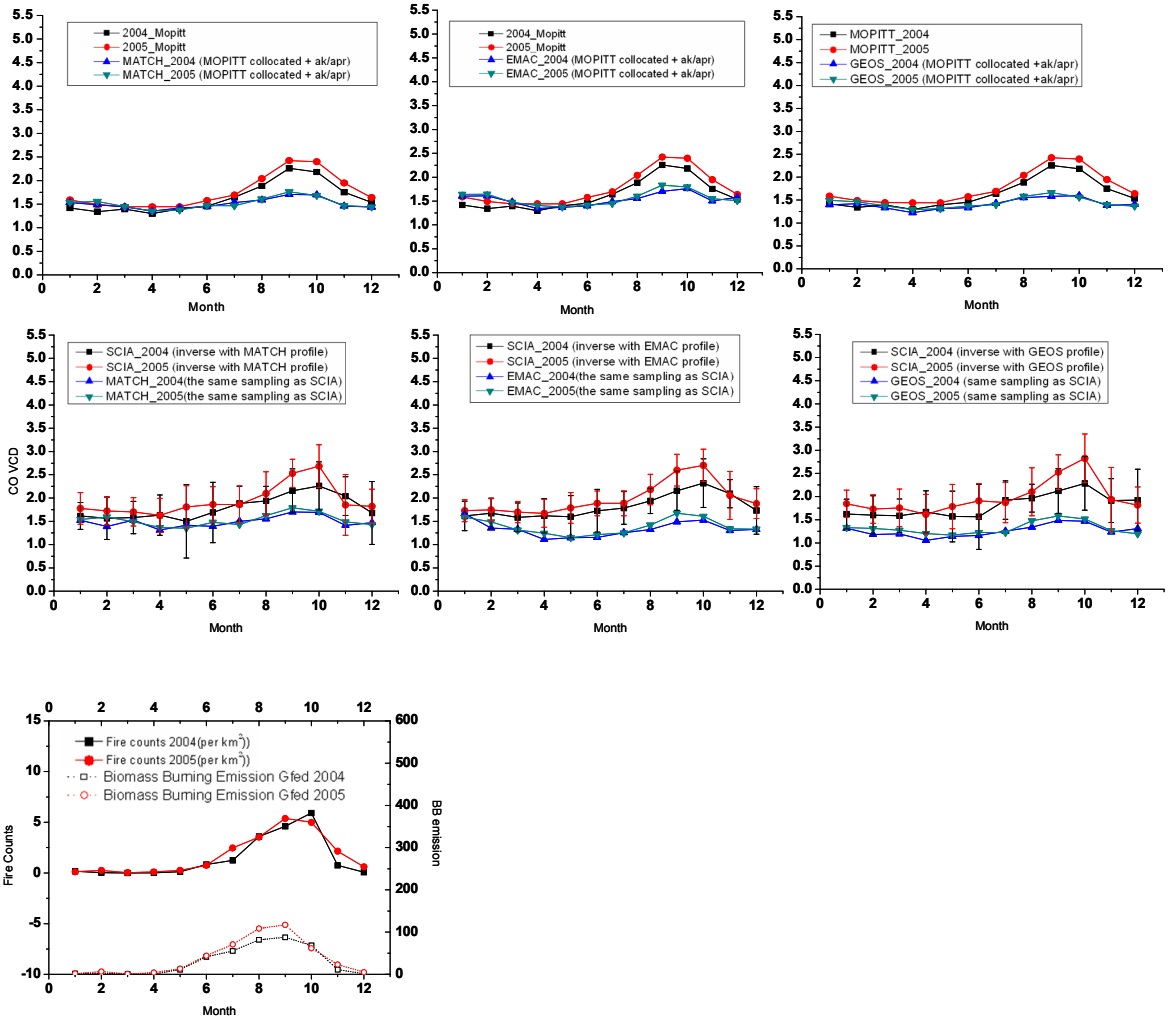

(3): Southwest Africa

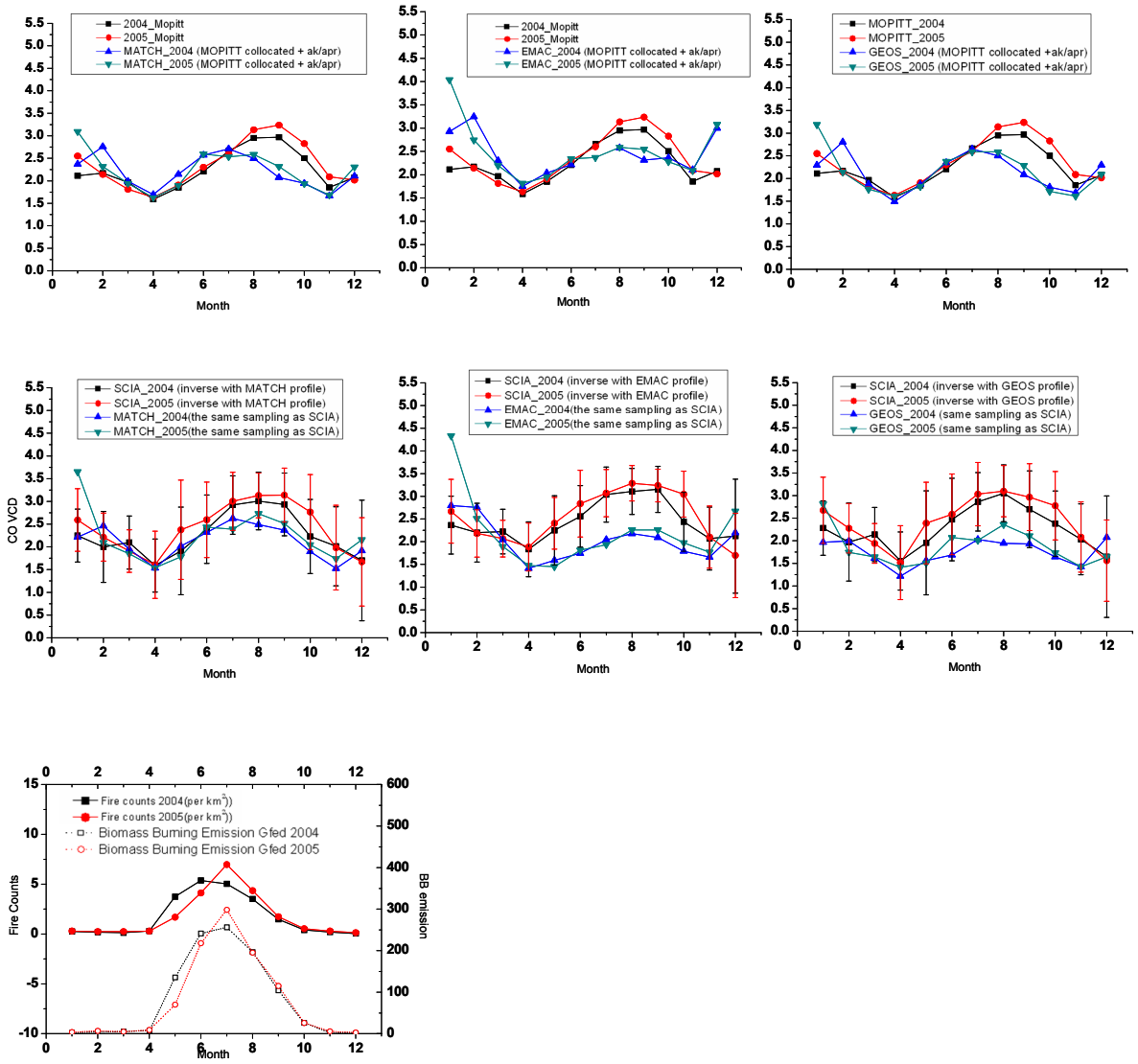

(4): South America

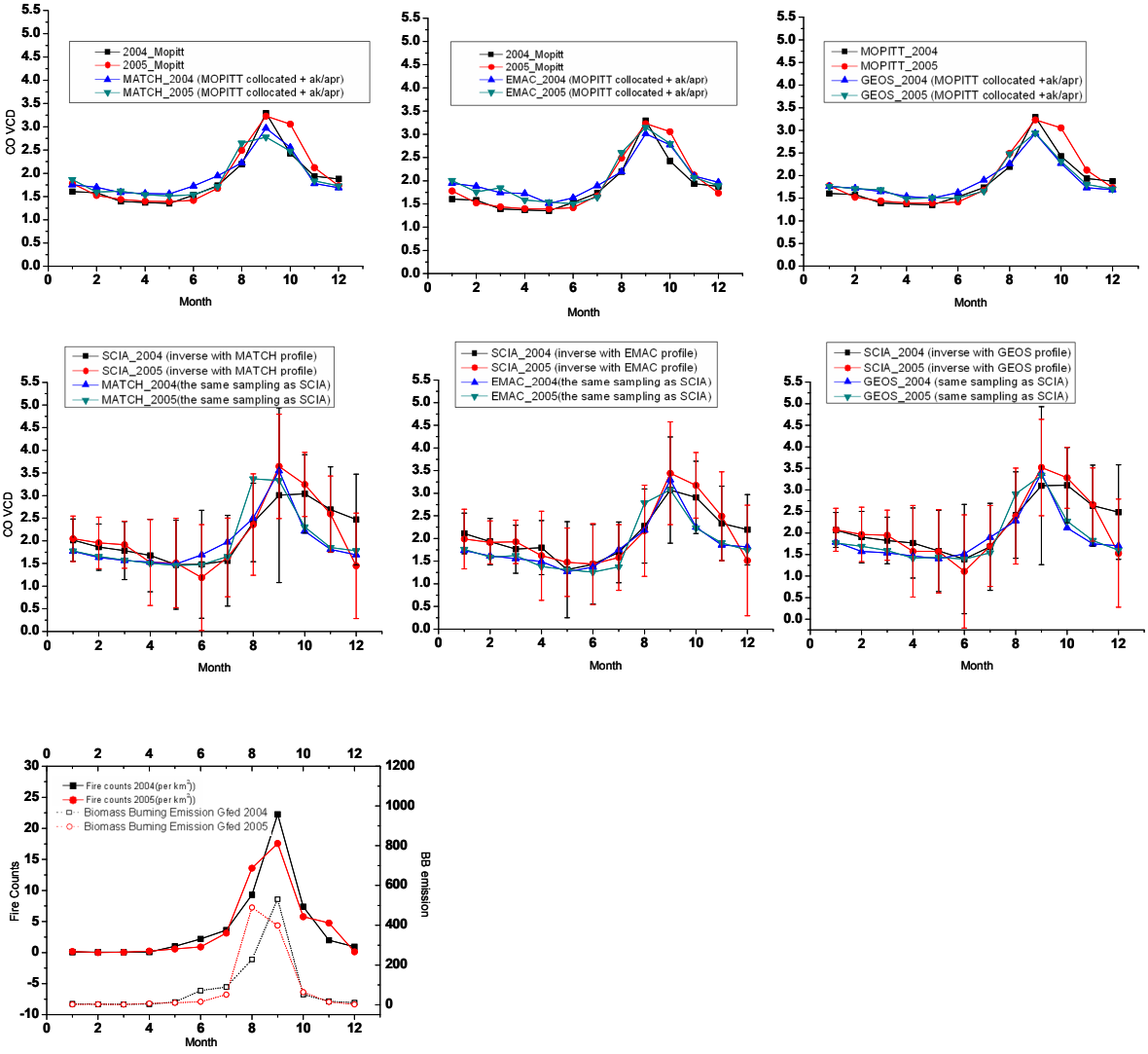

(5): Northern Australia

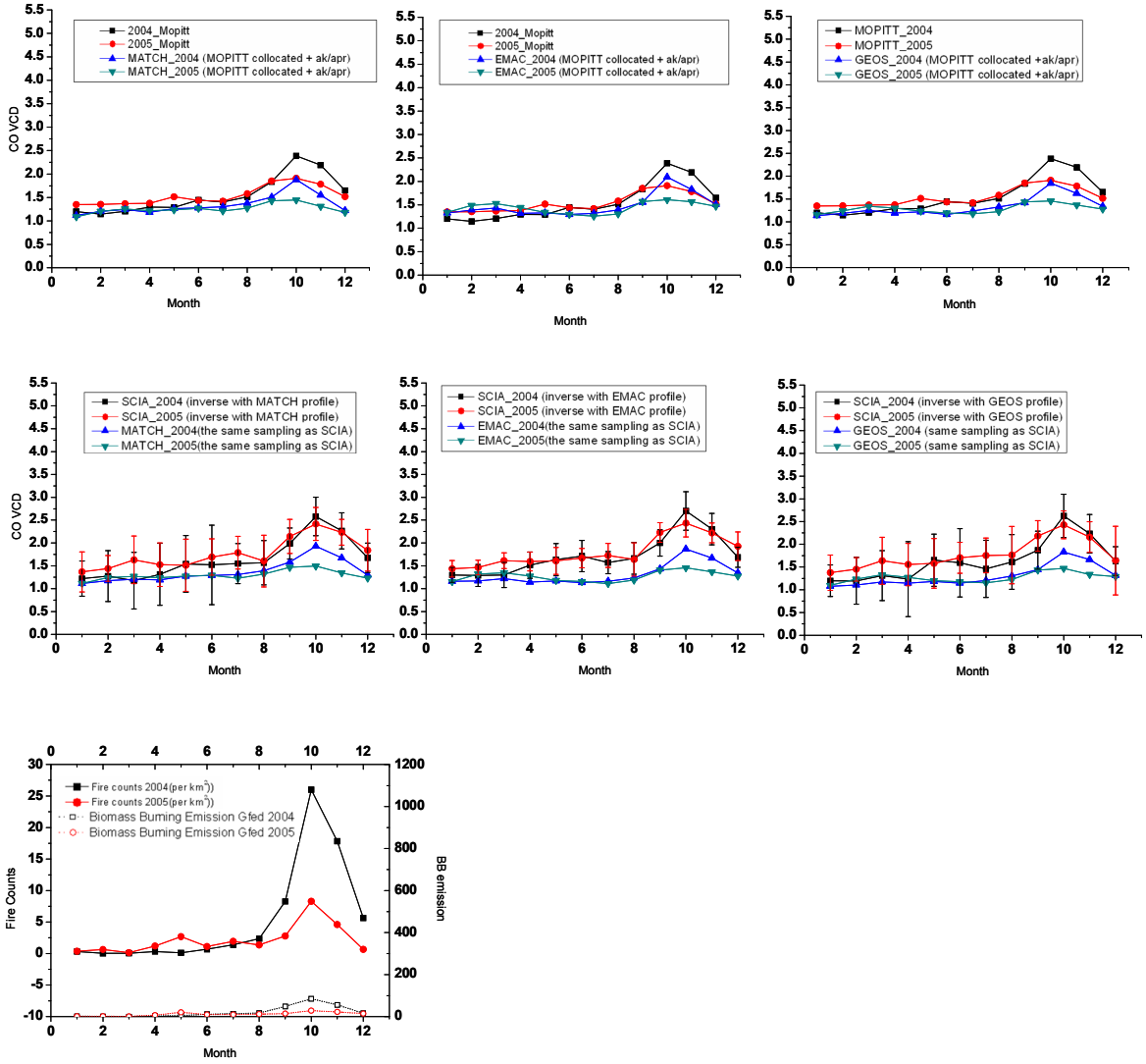

(6): Southern Asia

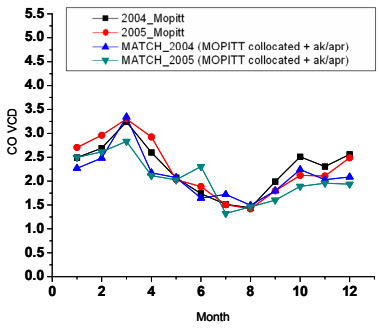

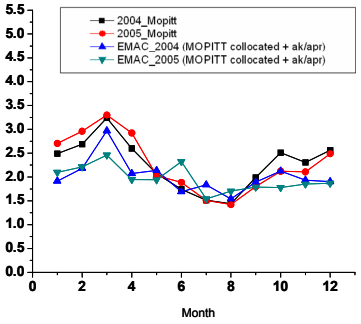

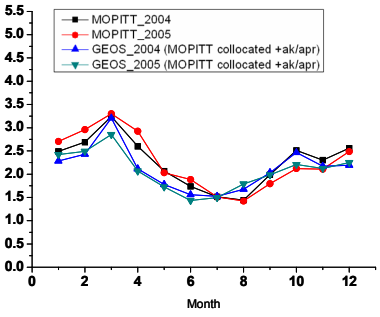

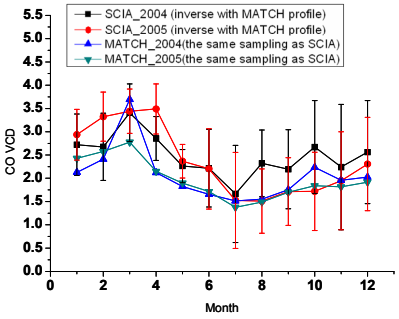

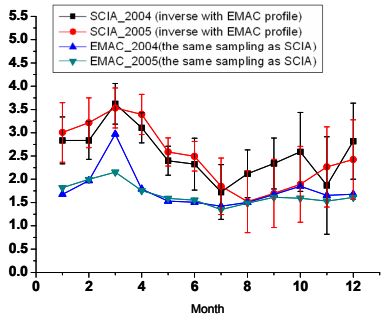

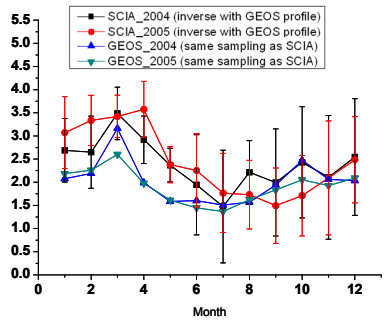

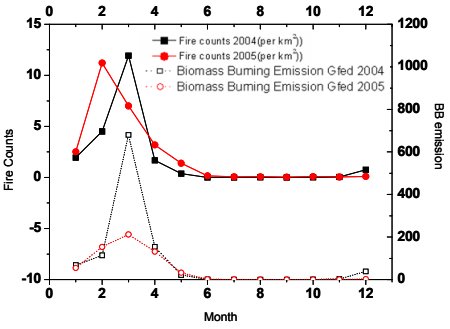

(7): Indonesia

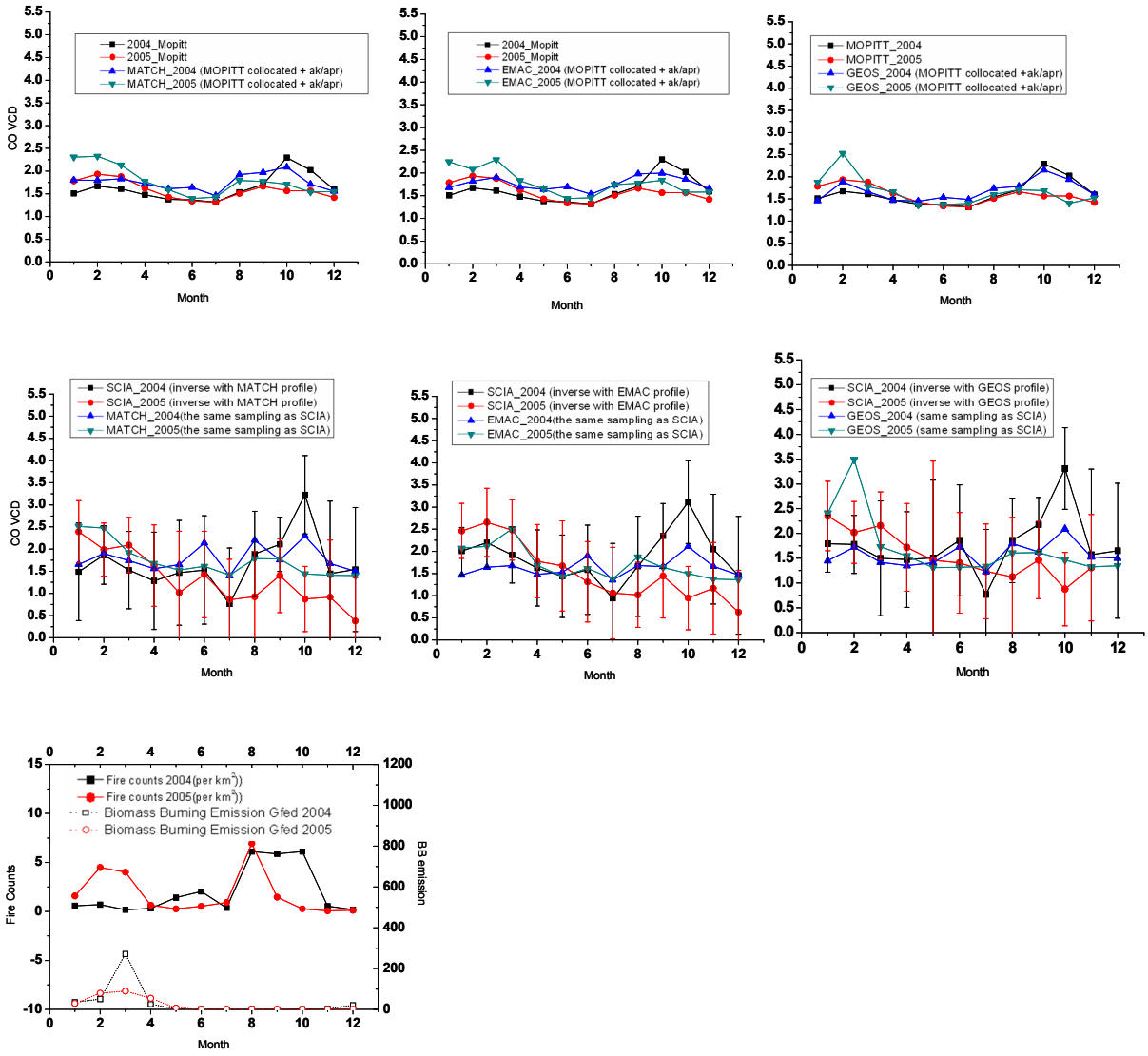
2004_Mopitt
2005_Mopitt
MATCH_2004 (MOPITT collocated + ak/apr)
MATCH_2005 (MOPITT collocated + ak/apr)
CO VCD
Month
2004_Mopitt
2005_Mopitt
EMAC_2004 (MOPITT collocated + ak/apr)
EMAC_2005 (MOPITT collocated + ak/apr)
Month
MOPITT_2004
MOPITT_2005
GEOS_2004 (MOPITT collocated +ak/apr)
GEOS_2005 (MOPITT collocated +ak/apr)
Month
SCIA_2004 (inverse with MATCH profile)
SCIA_2005 (inverse with MATCH profile)
MATCH_2004(the same sampling as SCIA)
MATCH_2005(the same sampling as SCIA)
CO VCD
Month
SCIA_2004 (inverse with EMAC profile)
SCIA_2005 (inverse with EMAC profile)
EMAC_2004(the same sampling as SCIA)
EMAC_2005(the same sampling as SCIA)
Month
SCIA_2004 (inverse with GEOS profile)
SCIA_2005 (inverse with GEOS profile)
GEOS_2004 (same sampling as SCIA)
GEOS_2005 (same sampling as SCIA)
Month
Fire counts 2004(per km²))
Fire counts 2005(per km²))
Biomass Burning Emission Gfed 2004
Biomass Burning Emission Gfed 2005
Fire Counts
BB emission
Month

(8): East China

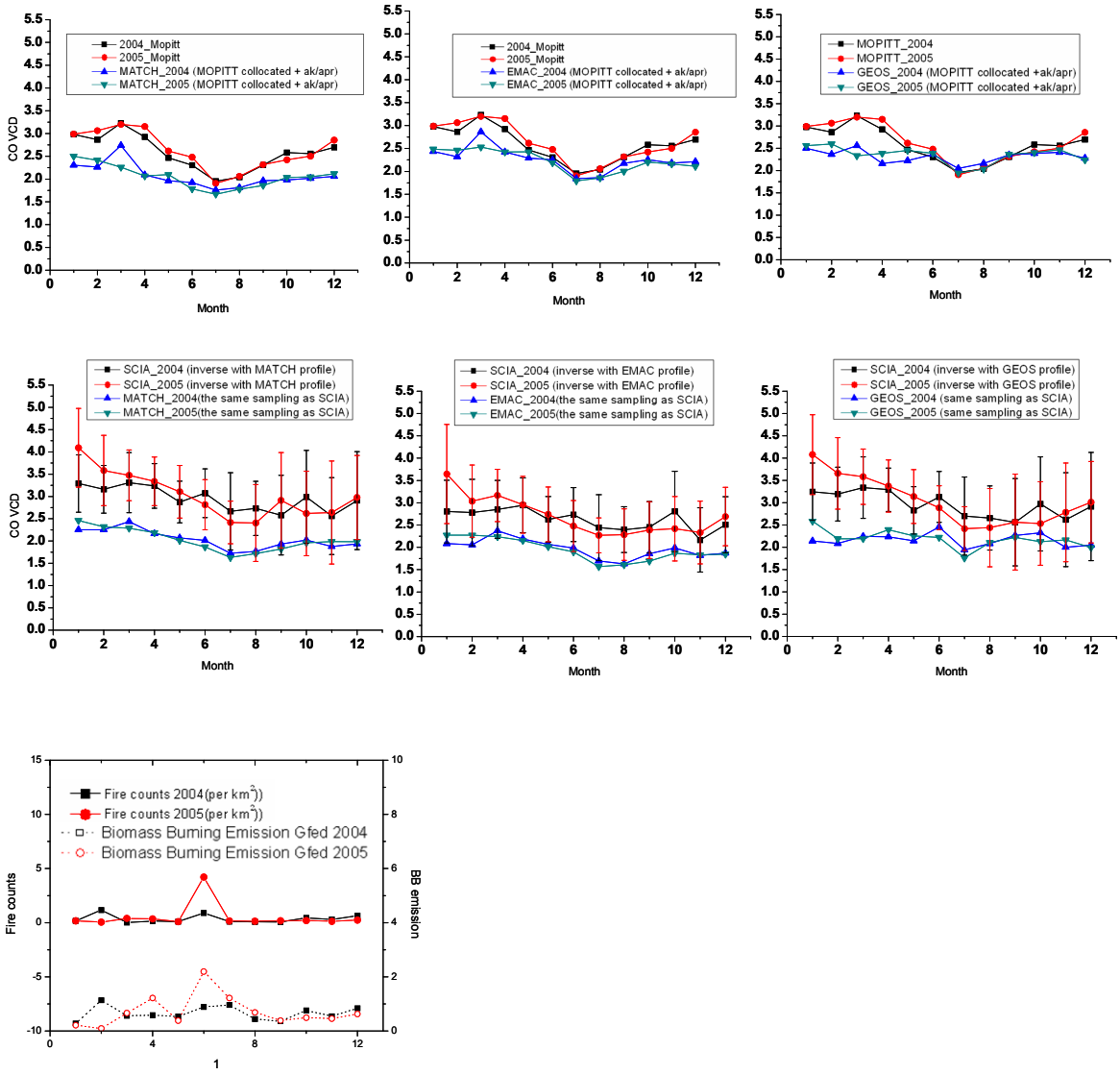

Figure 9.1: Comparison of the monthly mean CO VCDs (in units of 10^{18} molec/cm^2) between the satellite measurements (top: MOPITT; middle: SCIAMACHY) and model simulations (left: MATCH; middle: EMAC; right: GEOS-CHEM) for the regions indicated in Figure 8.1. All comparisons are done for only collocated measurements/model results; also the specific sensitivities of the satellite instrument have been considered (see text). Also shown are fire counts from ATSR (in units of 10^{-4} per km^2 per month), and the biomass burning emissions used in the models (the same for all models; in units of 10^{13} molecules/cm^2/s). The error bar of SCIAMACHY refers to the unbiased estimator of a weighted population variance.

The upper rows of the individual figures present the comparison of MOPITT with the different models; the middle rows present the respective comparison for the SCIAMACHY CO VCDs. In the bottom of the individual figures, information on measured fire counts and the CO emissions for the respective area are shown.

From the comparisons shown in Figure 9.1 several general conclusions can be drawn:

-In general, the agreement between MOPITT observations with model results is better than for SCIAMACHY.

-In most cases, the CO VCDs from SCIAMACHY observations are systematically larger than the CO VCDs from the models; this difference is especially large for Southwest Africa, Southern Asia, and East China.

-In general the seasonal variation of the intensity of biomass burning (as indicated by the fire counts) is well reproduced by the measurements and model results. However, in some cases also substantial differences are found.

-Over Central Africa the EMAC and GEOS-CHEM models show a second maximum in summer, which is not seen in the fire counts, emission inventories are also not in the satellite observations of CO. This discrepancy might indicate artifacts introduced by errors in the description of the atmospheric transport (e.g., transport of CO emitted from biomass burning south of the considered area). Especially the location of the ITCZ and its representation in the model may play a crucial role in particular when considering the separation between regions (1), (2) and (3) in Figure 8.1. Respective errors might be introduced in the models due to the limited horizontal resolution.

-For Southern Asia (region 6), transport of pollutants probably also plays an important role. Although almost no fires occur in that region after July, a second maximum is found in the observations and model results in autumn. The reason for this second maximum is probably transport of polluted air masses from biomass burning over Indonesia.

-Over Indonesia (region 7) a second maximum of the fire counts in autumn is found, which is not reflected in the CO emissions of that area.

The overall conclusion from this comparison is that for most biomass burning regions the model simulations underestimate the measured atmospheric CO VCD, implying that current emission inventories underestimate the true emissions. While this can already be concluded from

the comparison between the MOPITT observations and the model simulations, much larger differences are found for the comparison between SCIAMACHY and the model simulations. Because of the higher sensitivity of SCIAMACHY to the lowest atmospheric layers, this finding indicates that the CO concentrations are systematically underestimated by the models, especially close to the surface.

A strong underestimation of the CO VCD by the models is also found for East China. Since there most CO is emitted from anthropogenic sources, the uplifting into higher atmospheric layers might be less strong compared to most biomass burning regions. Thus a relatively large part of the emitted CO might be located close to the ground.

9.2 Comparison of Global Maps

In Figure 9.2, the spatial distribution of the differences between the seasonally averaged satellite observations (SCIAMACHY or MOPITT) and model simulations (MATCH, EMAC, or GEOS-CHEM, which are applied satellite AK/*a priori* and are collocated the same spatial-temporal samplings respectively) are shown. For SCIAMACHY only observations over land are considered, because the normalization procedure of SCIAMACHY data (see chapter 7) is performed over the oceans.

a: SCIAMACHY – EMAC (SCIAMACHY collocated +ak/apr)

Jan. to Mar. of 2004 to 2005

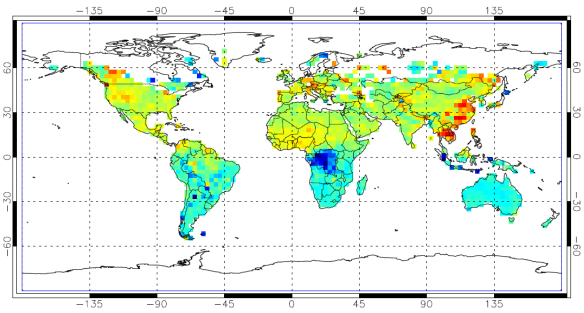

Apr. to Jun. of 2004 to 2005

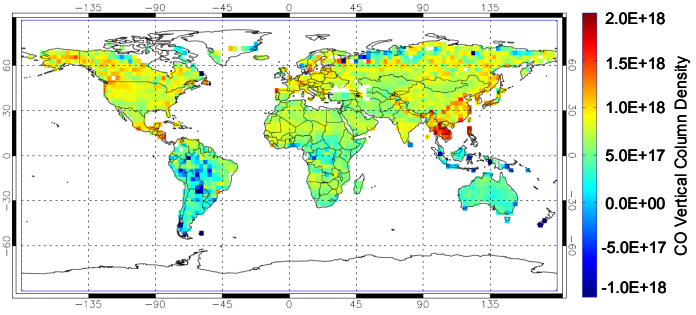

Jul. to Sep. of 2004 to 2005

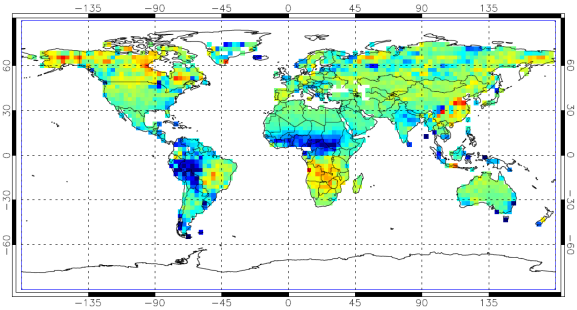

Oct. to Dec. of 2004 to 2005

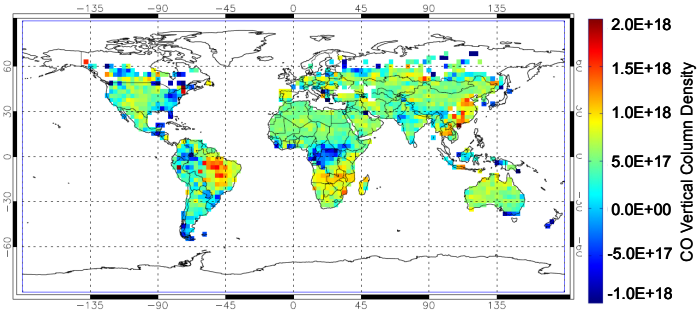

b: MOPITT – EMAC (MOPITT collocated +ak/apr)

Jan. to Mar. of 2004 to 2005

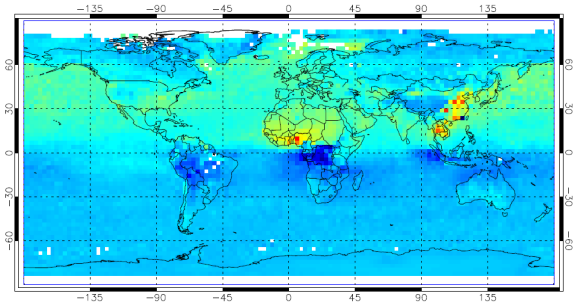

Apr. to Jun. of 2004 to 2005

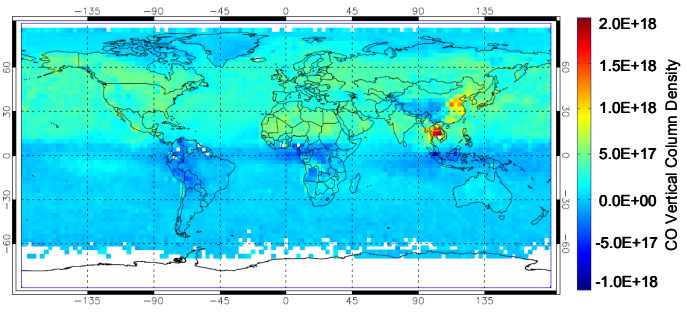

Jul. to Sep. of 2004 to 2005

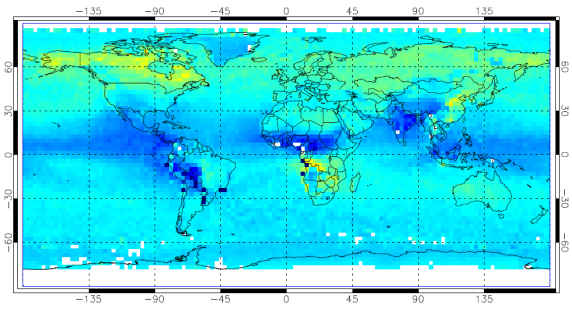

Oct. to Dec. of 2004 to 2005

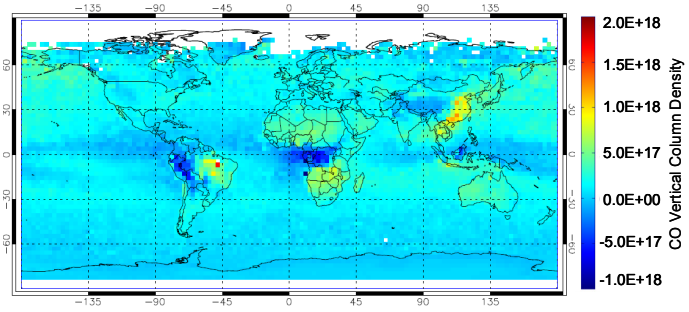

c: SCIAMACHY – MATCH (SCIAMACHY collocated +ak/apr)

Jan. to Mar. of 2004 to 2005

Apr. to Jun. of 2004 to 2005

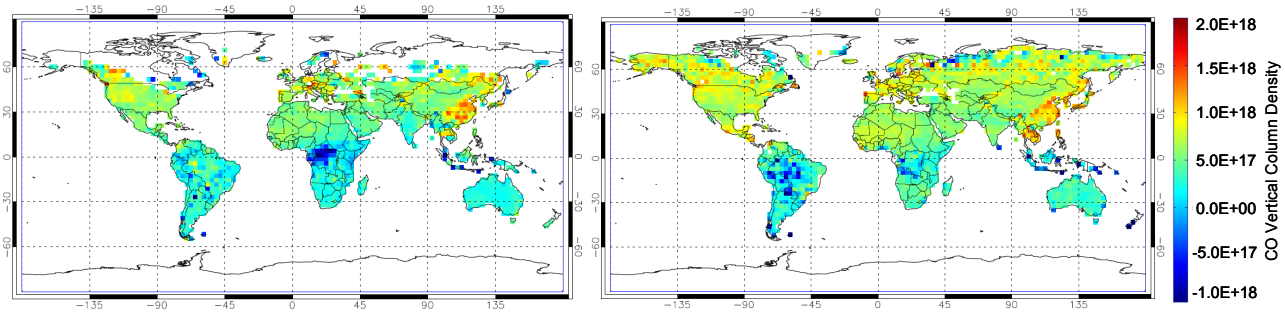

Jul. to Sep. of 2004 to 2005

Oct. to Dec. of 2004 to 2005

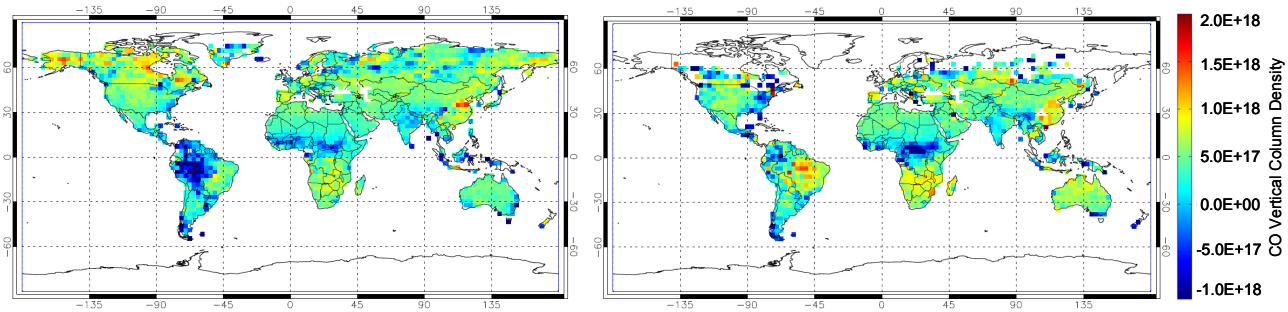

d: MOPITT –MATCH (MOPITT collocated +ak/apr)

Jan. to Mar. of 2004 to 2005

Apr. to Jun. of 2004 to 2005

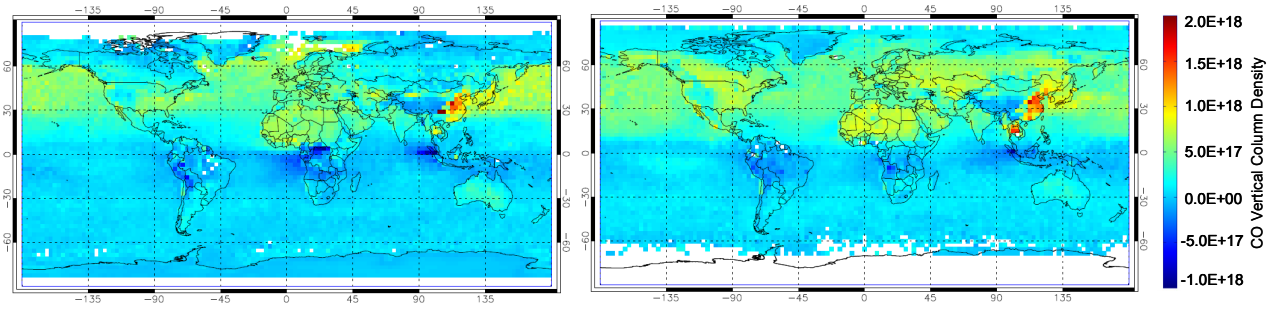

Jul. to Sep. of 2004 to 2005

Oct. to Dec. of 2004 to 2005

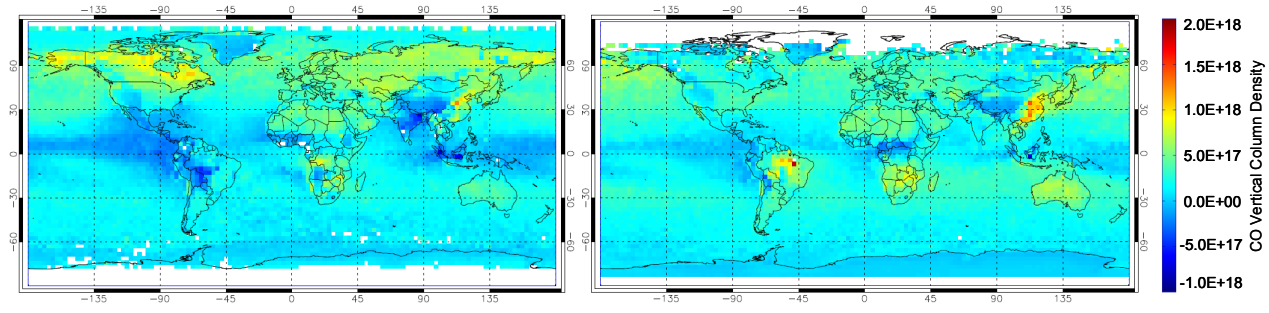

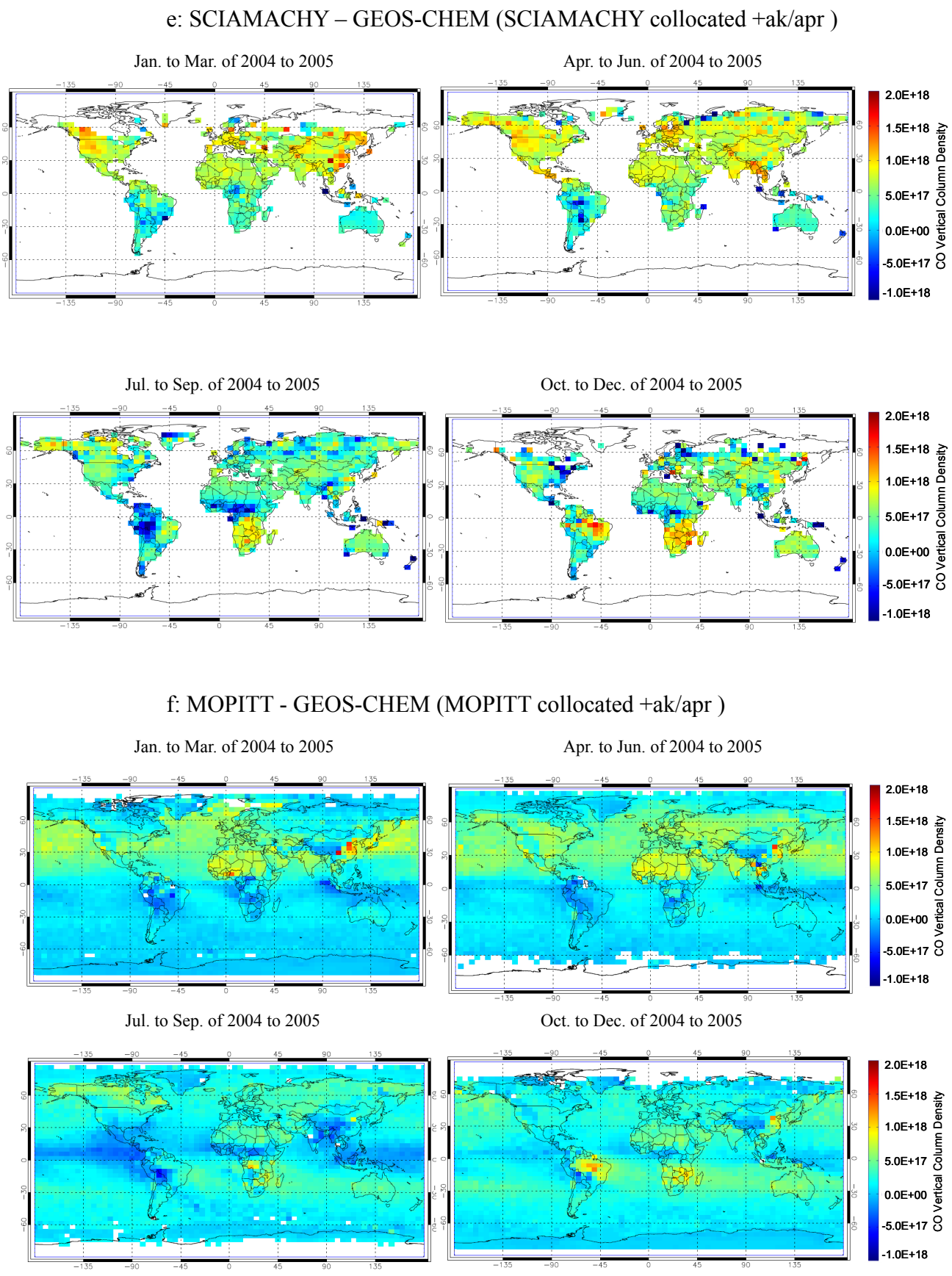

Figure 9.2: Spatial distribution of averaged seasonal differences between satellite (SCIAMACHY and MOPITT) measured CO total columns and model (MATCH, EMAC and GEOS-CHEM) simulated CO total columns, which are applied satellite AK/*a priori* and are collocated the same spatial-temporal samplings respectively.

In general the findings of this comparison are similar to those of the comparison of the time series in Figure 9.1: over regions with strong CO sources the models in general underestimate the observed CO VCD. As already seen in Figure 9.1, this underestimation is systematically larger for the comparison with SCIAMACHY. However, there are also some regions where the models systematically overestimate the observed CO VCDs; this effect is most pronounced in autumn in Africa (around the equator) and in summer in the western Amazon region. Interestingly, like for the case of underestimation by the models, the magnitude of the difference is larger for SCIAMACHY observations compared to those of the MOPITT observations. This indicates that also in the cases where models show higher CO VCDs than the measurements, the differences in the CO concentrations occur probably in the lowest layers of the atmosphere.

Another interesting finding is that in winter and spring the EMAC and MATCH models seem to systematically overestimate the CO concentrations in the southern hemisphere.

Conclusions and Outlook

The space-borne spectrometer SCIAMACHY onboard ENVISAT enables first precise measurements of atmospheric carbon monoxide from space with high sensitivity down to the surface and with global coverage over the continents. However, the spectral analysis using measurements of SCIAMACHY near infrared channel suffers from several instrumental problems. One important issue is the icing problem: water absorbed in the ENVISAT satellite frame, causes the formation of an ice layer on the detectors, strongly affecting the instrument's response function. This results in a reduction of the light throughput, and a variation of the shape of the slit function with time. Several procedures have been developed to correct the time dependent disturbances of the SCIAMACHY near IR channels. They either focus on a direct correction of the primary effects disturbing the SCIAMACHY spectra (Gloudemans *et al.*, 2005), or they apply post-corrections to the retrieved trace gas column densities (Buchwitz *et al.*, 2006b). From the comparison with collocated MOPITT data it turned out that these methods could improve the consistency of the derived CO data sets considerably; nevertheless, not all artefacts caused by the instrumental problems could be sufficiently corrected for the whole time series of SCIAMACHY CO observations.

Therefore, in this thesis a completely different strategy is developed to correct the SCIAMACHY CO observations, and a new data set of SCIAMACHY observations of the CO VCDs is produced. In contrast to other SCIAMACHY CO retrievals, a normalization procedure using coincident MOPITT observations over the oceans is applied. This normalization procedure is applied on a daily basis for different latitude ranges; thus artificial offsets in the SCIAMACHY CO data are corrected depending on season and latitude. The new SCIAMACHY CO data set can not be considered as fully independent from MOPITT observations, but is quite suitable for the investigation of the CO distribution over the continents, where all important CO emission sources are located. In this thesis SCIAMACHY observations with an effective cloud fraction <20% are used. In addition, a correction of the remaining cloud effects is applied that depends on effective cloud fraction, cloud top height and surface albedo. Here it is interesting to note that – to our knowledge – no explicit cloud

correction has so far been applied to SCIAMACHY CO observations. Even for cloud fractions <20%, omission of a proper cloud correction can lead to systematic errors up to 100%, especially over polluted regions.

In contrast to MOPITT observations, SCIAMACHY observations are also sensitive to the atmospheric layers directly above the surface. In this layer not only most CO emissions occur; this part of the atmosphere is also critical for health.

In this thesis observations from MOPITT and SCIAMACHY were compared to the results of different climate chemistry models: MATCH, EMAC, and GEOS-CHEM. For the comparison only coincident measurements/model results are selected, and the height dependent sensitivity of both satellite instruments is considered explicitly. The comparison shows that over many regions with strong emission sources (like biomass burning or anthropogenic emissions) the simulated CO VCDs are systematically smaller than the satellite observations. In particular, for most cases, the difference between SCIAMACHY and the models is larger than those between MOPITT and the models. Because of the reduced sensitivity of MOPITT towards the lowest part of the atmosphere, this thesis concludes that especially the atmospheric CO concentrations close to the surface are underestimated by the models. These findings probably indicate that the CO emission inventories used for the model simulations largely underestimate the true emissions. Besides most biomass burning regions, especially over East China the current actual CO emissions seem to be much larger than found in the emission inventories.

Interestingly, for some biomass burning regions (e.g., in the western Amazon region in summer and around the equator in Africa in autumn) the model simulations seem to overestimate the atmospheric CO concentrations.

In conclusions, our SCIAMACHY CO data set can be used to improve the existing CO emission inventories on a global scale.

Because the information content of the SCIAMACHY measurement is not high enough to discriminate the partial columns at different height layers, only the total vertical column density could be retrieved until now. However, as described in chapter 5, even for small cloud fractions most of the photons that the satellite receives are reflected from the cloud top, due to the high cloud top albedo. Thus, CO profiles can also be retrieved from SCIAMACHY using

observations for cloud covered pixels (cloud fraction > 20%) for different cloud top heights (cloud slicing). Although the CO profile can not be get from individual pixel measurement (only one cloud top height for individual pixels), monthly or longer time averaged CO profile can be derived from this strategy. Nevertheless, such profiles can be compared to averaged CO profiles from MOPITT and climate chemistry models, which will be done in the future.

References

Bergamaschi, P., Hein, R., Heimann, M., and Crutzen, P. J.: Inverse modeling of the global CO cycle 1. Inversion of CO mixing ratios, J Geophys Res-Atmos, 105, 1909-1927, 2000a.

Bergamaschi, P., Hein, R., Brenninkmeijer, C. A. M., and Crutzen, P. J.: Inverse modeling of the global CO cycle 2. Inversion of C-13/C-12 and O-18/O-16 isotope ratios, J Geophys Res-Atmos, 105, 1929-1945, 2000b.

Bey, I., Jacob, D. J., Yantosca, R. M., Logan, J. A., Field, B. D., Fiore, A. M., Li, Q. B., Liu, H. G. Y., Mickley, L. J., and Schultz, M. G.: Global modeling of tropospheric chemistry with assimilated meteorology: Model description and evaluation, J Geophys Res-Atmos, 106, 23073-23095, 2001.

Bovensmann, H., Burrows, J. P., Buchwitz, M., Frerick, J., Noel, S., Rozanov, V. V., Chance, K. V., and Goede, A. P. H.: SCIAMACHY: Mission objectives and measurement modes, J Atmos Sci, 56, 127-150, 1999.

Buchwitz, M., and Burrows, J. P.: Retrieval of CH, CO, and CO, total column amounts from SCIAMACHY near-infrared nadir spectra: Retrieval algorithm and first results, Remote Sensing of Clouds and the Atmosphere Viii, 5235, 375-388, Doi 10.1117/12.514219, 2004.

Buchwitz, M., de Beek, R., Bramstedt, K., Noel, S., Bovensmann, H., and Burrows, J. P.: Global carbon monoxide as retrieved from SCIAMACHY by WFM-DOAS, Atmos Chem Phys, 4, 1945-1960, 2004.

Buchwitz, M., de Beek, R., Noel, S., Burrows, J. P., Bovensmann, H., Bremer, H., Bergamaschi, P., Korner, S., and Heimann, M.: Carbon monoxide, methane and carbon dioxide columns retrieved from SCIAMACHY by WFM-DOAS: year 2003 initial data set, Atmos Chem Phys, 5, 3313-3329, 2005.

Buchwitz, M., de Beek, R., Noel, S., Burrows, J. P., Bovensmann, H., Schneising, O., Khlystova, I., Bruns, M., Bremer, H., Bergamaschi, P., Korner, S., and Heimann, M.: Atmospheric carbon gases retrieved from SCIAMACHY by WFM-DOAS: version 0.5 CO and CH_4 and impact of calibration improvements on CO2 retrieval, Atmos Chem Phys, 6, 2727-2751, 2006a.

Buchwitz, M., de Beek, R., Noel, S., Burrows, J. P., and Bovensmann, H.: Carbon monoxide, methane and carbon dioxide over China retrieved from SCIAMACHY/ENVISAT by WFM-DOAS, Esa Sp Publ, 611, 159-165 429, 2006b.

Buchwitz, M., Khlystova, I., Bovensmann, H., and Burrows, J. P.: Three years of global carbon monoxide from SCIAMACHY: comparison with MOPITT and first results related to the detection of enhanced CO over cities, Atmos Chem Phys, 7, 2399-2411, 2007.

Burrows, J. P., Holzle, E., Goede, A. P. H., Visser, H., and Fricke, W.: Sciamachy - Scanning imaging absorption spectrometer for atmospheric chartography, Acta Astronaut, 35, 445-451, 1995.

Crutzen, P. J., and Andreae, M. O.: Biomass burning in the tropics - impact on atmospheric chemistry and biogeochemical cycles, Science, 250, 1669-1678, 1990.

Darwent, B. DeB.: Bond dissociation energies in simple molecules, NSRDS-NBS 31, 48p., 1970.

de Laat, A. T. J., Gloudemans, A. M. S., Schrijver, H., van den Broek, M. M. P., Meirink, J. F., Aben, I., and Krol, M.: Quantitative analysis of SCIAMACHY carbon monoxide total column measurements, Geophys Res Lett, 33, -, Artn L07807, Doi 10.1029/2005gl025530, 2006.

de Laat, A. T. J., Gloudemans, A. M. S., Aben, I., Krol, M., Meirink, J. F., van der Werf, G. R., and Schrijver, H.: Scanning Imaging Absorption Spectrometer for Atmospheric Chartography carbon monoxide total columns: Statistical evaluation and comparison with chemistry transport model results (vol 112, art no D21306, 2007), J Geophys Res-Atmos, 112, -, Artn D21306, Doi 10.1029/2007jd009378, 2007.

de Laat, A. T. J., Gloudemans, A. M. S., Aben, I., and Schrijver, H.: Global evaluation of SCIAMACHY and MOPITT carbon monoxide column differences for 2004-2005, J Geophys, Res-Atmos, 115, -, Artn D06307, Doi 10.1029/2009jd012698, 2010.

Deeter, M. N., Emmons, L. K., Francis, G. L., Edwards, D. P., Gille, J. C., Warner, J. X., Khattatov, B., Ziskin, D., Lamarque, J. F., Ho, S. P., Yudin, V., Attie, J. L., Packman, D., Chen, J., Mao, D., and Drummond, J. R.: Operational carbon monoxide retrieval algorithm and selected results for the MOPITT instrument, J Geophys Res-Atmos, 108, -, Artn 4399, Doi 10.1029/2002jd003186, 2003.

Deutschmann, T.: Atmospheric radiative transfer modelling with Monte Carlo methods, Diploma Physics, University of Heidelberg, Heidelberg, Germany, 2008.

Deutschmann, T., Beirle, S., Friess, U., Grzegorski, M., Kern, C., Kritten, L., Pfeilsticker, K., Platt, U., Prados-Roman, C., Pukite, J., Wagner, T., and Werner, B.: The Monte Carlo atmospheric radiative transfer Model McArtim: Introduction and validation of Jacobians and 3D features, Atmos. Meas. Tech. Discuss., 2010.

Dils, B., De Maziere, M., Muller, J. F., Blumenstock, T., Buchwitz, M., de Beek, R., Demoulin, P., Duchatelet, P., Fast, H., Frankenberg, C., Gloudemans, A., Griffith, D., Jones, N., Kerzenmacher, T., Kramer, I., Mahieu, E., Mellqvist, J., Mittermeier, R. L., Notholt, J., Rinsland, C. P., Schrijver, H., Smale, D., Strandberg, A., Straume, A. G., Stremme, W., Strong, K., Sussmann, R., Taylor, J., van den Broek, M., Velazco, V., Wagner, T., Warneke, T., Wiacek, A., and Wood, S.: Comparisons between SCIAMACHY and ground-based FTIR data for total columns of CO, CH_4, CO2 and N2O, Atmos Chem Phys, 6, 1953-1976, 2006.

Drummond, J. R., and Mand, G. S.: The measurements of pollution in the troposphere (MOPITT) instrument: Overall performance and calibration requirements, J Atmos Ocean Tech, 13, 314-320, 1996.

Edwards, D. P., Halvorson, C. M., and Gille, J. C.: Radiative transfer modeling for the EOS Terra satellite Measurement of Pollution in the Troposphere (MOPITT) instrument, J Geophys Res-Atmos, 104, 16755-16775, 1999.

Emmons, L. K., Deeter, M. N., Gille, J. C., Edwards, D. P., Attie, J. L., Warner, J., Ziskin, D., Francis, G., Khattatov, B., Yudin, V., Lamarque, J. F., Ho, S. P., Mao, D., Chen, J. S., Drummond, J., Novelli, P., Sachse, G., Coffey, M. T., Hannigan, J. W., Gerbig, C., Kawakami, S., Kondo, Y., Takegawa, N., Schlager, H., Baehr, J., and Ziereis, H.: Validation of Measurements of Pollution in the Troposphere (MOPITT) CO retrievals with aircraft in situ profiles, J Geophys Res-Atmos, 109, -, Artn D03309, Doi 10.1029/2003jd004101, 2004.

Eskes, H. J., and Boersma, K. F.: Averaging kernels for DOAS total-column satellite retrievals, Atmos Chem Phys, 3, 1285-1291, 2003.

Frankenberg, C., Platt, U., and Wagner, T.: Iterative maximum a posteriori (IMAP)-DOAS for retrieval of strongly absorbing trace gases: Model studies for CH_4 and CO2 retrieval from near infrared spectra of SCIAMACHY onboard ENVISAT, Atmos Chem Phys, 5, 9-22, 2005a.

Frankenberg, C., Platt, U., and Wagner, T.: Retrieval of CO from SCIAMACHY onboard ENVISAT: detection of strongly polluted areas and seasonal patterns in global CO abundances, Atmos Chem Phys, 5, 1639-1644, 2005b.

Fuglestvedt, J, S., Isaksen, I. S, A., Wang, and W, C.: Estimates of indirect global warming potentials for CH 4 , CO and NO x : Two-dimensional chemical modeling, Springer, Heidelberg, ALLEMAGNE, 1996.

Gilliam, O. R., Johnson, C. M., and Gordy, W.: Microwave Spectroscopy in the Region from Two to Three Millimeters, Physical Review, 78, 140, 1950.

Gloudemans, A., Schrijver, H., Straume, A., Aben, I., Maurellis, A., Buchwitz, M., de Beek, R., Frankenberg, C., and Wagner, T.: CH4 and CO total columns from SCIAMACHY: comparisons with TM3 and MOPITT, in: Remote Sensing of Clouds and the Atmosphere VIII, vol. 5235 of Proceedings ACVE2, 3-7 May, Frascati, Italy, 2004.

Gloudemans, A. M. S., Schrijver, H., Kleipool, Q., van den Broek, M. M. P., Straume, A. G., Lichtenberg, G., van Hees, R. M., Aben, I., and Meirink, J. F.: The impact of SCIAMACHY near-infrared instrument calibration on CH_4 and CO total columns, Atmos Chem Phys, 5, 2369-2383, 2005.

Gloudemans, A. M. S., Krol, M. C., Meirink, J. F., de Laat, A. T. J., van der Werf, G. R., Schrijver, H., van den Broek, M. M. P., and Aben, I.: Evidence for long-range transport of carbon monoxide in the Southern Hemisphere from SCIAMACHY observations, Geophys Res Lett, 33, -, Artn L16807, Doi 10.1029/2006gl026804, 2006.

Gloudemans, A. M. S., Schrijver, H., Hasekamp, O. P., and Aben, I.: Error analysis for CO and CH_4 total column retrievals from SCIAMACHY 2.3 mu m spectra, Atmos Chem Phys, 8, 3999-4017, 2008.

Gloudemans, A. M. S., de Laat, A. T. J., Schrijver, H., Aben, I., Meirink, J. F., and van der Werf, G. R.: SCIAMACHY CO over land and oceans: 2003-2007 interannual variability, Atmos Chem Phys, 9, 3799-3813, 2009.

Goody, R., and Yung, Y.: Atmospheric Radiation, Oxford University Press, New York, 1989.

Gottwald, M., Bovensmann, H., Lichtenberg, G., Noël, S., von Bargen, A., Slijkhuis, S., Piters, A., Hoogeveen, R., von Savigny, C., Buchwitz, M., Kokhanovsky, A., Richter, A., Rozanov, A., Holzer-Popp, T., Bramstedt, K., Lambert, J.-C., Skupin, J., Wittrock, F., Schrijver, H., and Burrows, J. P.: SCIAMACHY, Monitoring the Changing Earth's Atmosphere, edited by: Gottwald, M., DLR, Institut für Methodik der Fernerkundung (IMF), Germany, 2006.

Grubbs, T.: Analysis of the IR spectrum of carbon monoxide: http://www2.stetson.edu/~wgrubbs/datadriven/rotationcarbonmonoxide/rotationcowtg.html, Stetson University, DeLand, 2010.

Haken, H., and Wolf, H. C.: Molekülphysik und Quantenchemie, Springer, 2006.

Hatakeyama, S., Izumi, K., Fukuyama, T., Akimoto, H., and Washida, N.: Reactions of Oh with Alpha-Pinene and Beta-Pinene in Air- Estimate of Global Co Production from the Atmospheric Oxidation of Terpenes, J Geophys Res-Atmos, 96, 947-958, 1991.

Herzberg, G.: Molecular Spectra and Molecular Structure: I SPECTRA OF DIATOMIC MOLECULES, in, edited by: SPINKS, J. W. T., F.R.S.C., Krieger Publishing Company,, 1989.

Holloway, T., Levy, H., and Kasibhatla, P.: Global distribution of carbon monoxide, J Geophys Res-Atmos, 105, 12123-12147, 2000.

Houghton, J.: The IPCC report 2001, Proceedings of the 1st Solar and Space Weather Euroconference on the Solar Cycle and Terrestrial Climate, 463, 255-259 680, 2000.

Isaksen, I. S. A., and Hov, O.: Calculations of trends in the tropospheric concentrations of O3, OH, CO, CH_4 and NOx, Tellus B, 39B, 271-283, 1987.

Jockel, P., Tost, H., Pozzer, A., Bruhl, C., Buchholz, J., Ganzeveld, L., Hoor, P., Kerkweg, A., Lawrence, M. G., Sander, R., Steil, B., Stiller, G., Tanarhte, M., Taraborrelli, D., Van Aardenne, J., and Lelieveld, J.: The atmospheric chemistry general circulation model ECHAM5/MESSy1: consistent simulation of ozone from the surface to the mesosphere, Atmos Chem Phys, 6, 5067-5104, 2006.

Justice, C. O., Vermote, E., Townshend, J. R. G., Defries, R., Roy, D. P., Hall, D. K., Salomonson, V. V., Privette, J. L., Riggs, G., Strahler, A., Lucht, W., Myneni, R. B., Knyazikhin, Y., Running, S. W., Nemani, R. R., Wan, Z. M., Huete, A. R., van Leeuwen, W., Wolfe, R. E., Giglio, L., Muller, J. P., Lewis, P., and Barnsley, M. J.: The Moderate Resolution Imaging Spectroradiometer (MODIS): Land remote sensing for global change research, Ieee T Geosci Remote, 36, 1228-1249, 1998.

Kopacz, M., Jacob, D. J., Fisher, J. A., Logan, J. A., Zhang, L., Megretskaia, I. A., Yantosca, R. M., Singh, K., Henze, D. K., Burrows, J. P., Buchwitz, M., Khlystova, I., McMillan, W. W., Gille, J. C., Edwards, D. P., Eldering, A., Thouret, V., and Nedelec, P.: Global estimates of CO sources with high resolution by adjoint inversion of multiple satellite datasets (MOPITT, AIRS, SCIAMACHY, TES), Atmos Chem Phys, 10, 855-876, 2010.

Krijger, J. M., van Weele, M., Aben, I., and Frey, R.: Technical Note: The effect of sensor resolution on the number of cloud-free observations from space, Atmos Chem Phys, 7, 2881-2891, 2007.

Kutzelnigg, W.: Einführung in die Theoretische Chemie. Wiley-VCH, 2002.

Leue, C., Wenig, M., Wagner, T., Klimm, O., Platt, U., and Jahne, B.: Quantitative analysis of NOx emissions from Global Ozone Monitoring Experiment satellite image sequences, J Geophys Res-Atmos, 106, 5493-5505, 2001.

Levine, J. S.: Global Biomass Burning - Atmospheric, Climatic, and Biospheric Implications, Global Biomass Burning, R23-R30 569, 1991.

Levine, J. S., Cofer, W. R., Cahoon, D. R., and Winstead, E. L.: Biomass Burning - a Driver for Global Change, Environ Sci Technol, 29, A120-A125, 1995.

Logan, J. A., Prather, M. J., Wofsy, S. C., and Mcelroy, M. B.: Tropospheric Chemistry - a Global Perspective, J Geophys Res-Oc Atm, 86, 7210-7254, 1981.

Maurellis, A. N., Cravens, T. E., Gladstone, G. R., Waite, J. H., and Acton, L. W.: Jovian x-ray emission from solar x-ray scattering, Geophys Res Lett, 27, 1339-1342, 2000.

Miyoshi, A., Hatakeyama, S., and Washida, N.: Om Radical-Initiated Photooxidation of Isoprene - an Estimate of Global Co Production, J Geophys Res-Atmos, 99, 18779-18787, 1994.

Pan, L. W., Gille, J. C., Edwards, D. P., Bailey, P. L., and Rodgers, C. D.: Retrieval of tropospheric carbon monoxide for the MOPITT experiment, J. Geophys. Res, 103, 32,277-232,290, 1998.

Perliski, L. M., and Solomon, S.: On the Evaluation of Air-Mass Factors for Atmospheric near-Ultraviolet and Visible Absorption-Spectroscopy, J Geophys Res-Atmos, 98, 10363-10374, 1993.

Platt, U., and Wiley, J.: Differential optical absorption spectroscopy (DOAS), Air Monitoring by Spectroscopic Techniques, 27-84, 1994.

Prather, M. J.: Time scales in atmospheric chemistry: Theory, GWPs for CH_4 and CO, and runaway growth, Geophys Res Lett, 23, 2597-2600, 1996.

Rodgers, C. D.: Retrieval of Atmospheric-Temperature and Composition from Remote Measurements of Thermal-Radiation, Rev Geophys, 14, 609-624, 1976.

Rodgers, C. D.: Inverse Methods for Atmospheric Sounding, World Scientific Publishing, New York, 2000.

Schneising, O.: Analysis and interpretation of satellite measurements in the near-infrared spectral region: Atmospheric carbon dioxide and methane, Doctor, Universität Bremen, Bremen, 2008.

Schrijver, H.: Retrieval of carbon monoxide, methane and nitrous oxide from SCIAMACHY measurements, in: ESA WPP-161 1, vol. 5235, Proc. ESAMS, European Symposium on Atmospheric Measurements from Space, pp. 285-294, Estec, Nordwijk, The Netherlands, 2004.

Shine, K. P., Derwent, R. G., Wuebbles, D. J., and Morcrette, J.-J.: Chapter 2. Radiative Forcing of Climate. In: Climate Change: , in: The IPCC Scientific Assessment, edited by: Houghton, J. T., Jenkins, G. J., and Ephraums, J. J., Cambridge University Press, Cambridge, UK, pp. 41-68., 1990.

Solomon, S., Miller, H. L., Smith, J. P., Sanders, R. W., Mount, G. H., Schmeltekopf, A. L., and Noxon, J. F.: Atmospheric No-3 .1. Measurement Technique and the Annual Cycle at 40-Degrees-N, J Geophys Res-Atmos, 94, 11041-11048, 1989.

Straume, A. G., Schrijver, H., Gloudemans, A. M. S., Houweling, S., Aben, I., Maurellis, A. N., de Laat, A. T. J., Kleipool, Q., Lichtenberg, G., van Hees, R., Meirink, J. F., and Krol, M.: The global variation of CH_4 and CO as seen by SCIAMACHY, Adv Space Res, 36, 821-827, Doi 10.1016/j.asr.2005.03.027, 2005.

Thomas, G. E., and Stamnes, K.: Radiative Transfer in the Atmosphere and Ocean, Cambridge University Press, Cambridge, 1999.

Turquety, S., Clerbaux, C., Law, K., Coheur, P. F., Cozic, A., Szopa, S., Hauglustaine, D. A., Hadji-Lazaro, J., Gloudemans, A. M. S., Schrijver, H., Boone, C. D., Bernath, P. F., and Edwards, D. P.: CO emission and export from Asia: an analysis combining complementary satellite measurements (MOPITT, SCIAMACHY and ACE-FTS) with global modeling, Atmos Chem Phys, 8, 5187-5204, 2008.

Volkamer, R., Etzkorn, T., Geyer, A., and Platt, U.: Correction of the oxygen interference with UV spectroscopic (DOAS) measurements of monocyclic aromatic hydrocarbons in the atmosphere, Atmos Environ, 32, 3731-3747, 1998.

von Kuhlmann, R., Lawrence, M. G., Crutzen, P. J., and Rasch, P. J.: A model for studies of tropospheric ozone and nonmethane hydrocarbons: Model description and ozone results, J Geophys Res-Atmos, 108, -, Artn 4294, Doi 10.1029/2002jd002893, 2003.

Wagner, T., Burrows, J. P., Deutschmann, T., Dix, B., von Friedeburg, C., Friess, U., Hendrick, F., Heue, K. P., Irie, H., Iwabuchi, H., Kanaya, Y., Keller, J., McLinden, C. A., Oetjen, H., Palazzi, E., Petritoli, A., Platt, U., Postylyakov, O., Pukite, J., Richter, A., van Roozendael, M., Rozanov, A., Rozanov, V., Sinreich, R., Sanghavi, S., and Wittrock, F.: Comparison of box-air-mass-factors and radiances for Multiple-Axis Differential Optical Absorption Spectroscopy (MAX-DOAS) geometries calculated from different UV/visible radiative transfer models, Atmos Chem Phys, 7, 1809-1833, 2007.

Wang, P., Stammes, P., van der A, R., Pinardi, G., and van Roozendael, M.: FRESCO+: an improved O-2 A-band cloud retrieval algorithm for tropospheric trace gas retrievals, Atmos Chem Phys, 8, 6565-6576, 2008.

Weinstoc, B., and Niki, H.: Carbon-Monoxide Balance in Nature, Science, 176, 290-&, 1972.

Wenig, M.: Satellite measurement of long-term tropospheric trace gas distributions and source strengths - algorithm development and data analysis, Ph.D., Institut f˙ur Umweltphysik,, University of Heidelberg., Heidelberg, 2001.

Wild, O., and Prather, M. J.: Excitation of the primary tropospheric chemical mode in a global three-dimensional model, J Geophys Res-Atmos, 105, 24647-24660, 2000.

Wofsy, S. C., Mcconnel.Jc, and Mcelroy, M. B.: Atmospheric Ch_4, Co, and Co2, J Geophys Res, 77, 4477-&, 1972.

Zimmerman, P. R., Chatfield, R. B., Fishman, J., Crutzen, P. J., and Hanst, P. L.: Estimates on Production of Co and H-2 from Oxidation of Hydrocarbon Emissions from Vegetation, Geophys Res Lett, 5, 679-682, 1978.

Acknowledgements

I would especially like to express my gratitude to Prof. Ulrich Platt and Prof. Thomas Wagner for the opportunity to conduct this PhD in Heidelberg University and Max Plank institute for chemistry and for all their help and many useful discussions throughout the past years. They are inspiring mentors and teachers who not only taught me how to do scientific work, but also how to communicate my scientific results. I am particularly grateful for all of their encouragement throughout my years in Germany. I would like to say my interest in this field of study would never fade and I really enjoy the time I live in Germany.

I would like to express my thanks to Prof. Jos Lelieveld for accepting me as a member of IMPRS and do fruitful scientific communications with German scientists. The funding received during my studies is appreciated greatly.

I acknowledge Christian Frankenberg for providing me with the (IMAP)-DOAS algorithm for SCIAMACHY CO retrieval. I am especially thankful for his continuous invaluable support and the explanation of (IMAP)-DOAS algorithm.

I would like to thank Steffen Beirle and Sven Kühl for helping me with a lot of technical problems and sharing their knowledge in many discussions. They are experts in this field.

I would like to thank to Marloes Penning de Vries, Sven Kühl and Ellen Eigemeie for proofreading my thesis. With their help, the chapter becomes clearer and some unnoticeable grammatical mistakes are corrected. I also thank Marloes Penning de Vries for practicing spoken English with me during daily conversations.

I thank all our group members for their very fruitful suggestion and cooperation. They never hesitated in helping with a problem. Their helpful comments and discussions were invaluable throughout this process.

I thank Jia Jia for being there, for her emotional support even when I was in a grouchy mood, and for helping me with daily language (German) problems.

Finally, I would like to thank my father and mother whose encouragements and supports have made all this possible.